Ultrafast carrier dynamics in III-nitride nanostructures and LED quantum efficiency

Thèse N° 9746

Wei LIU

EPFL
ÉCOLE POLYTECHNIQUE
FÉDÉRALE DE LAUSANNE

2019

"Seek Truth from Facts"

—Book of Han

Dedicate to

my parents, my wife, and my friends.

Abstract

Since the seminal report about the first Candela-class-brightness InGaN blue light-emitting diodes (LEDs) by Shuji Nakamura *et al.* in 1994, III-nitride semiconductors have been one of the most important platforms for optoelectronic devices. The achievement in III-nitride LEDs has been awarded by the physics Nobel Prize in 2014 *"for the invention of efficient blue light-emitting diodes which has enabled bright and energy-saving white light sources".* Nowadays, blue LEDs with InGaN/GaN quantum wells (QWs) as active layers achieve more than 85% internal quantum efficiency, even in the presence of a high density of dislocations (>10^8 cm^{-2}), which act as non-radiative recombination centers (NRCs). Carrier localization induced by the random alloy disorder of InGaN is widely accepted as the main reason for defect-insensitivity of the QWs, which suppresses significantly carrier diffusion towards NRCs.

Despite the success of blue LED technology, the quantum efficiency is still limited for LEDs towards high power, green-red colors, and micrometer dimensions. The interaction of carrier recombination dynamics with alloy disorder, dislocations and point defects has not yet been fully understood, which is essential for tackling these issues. To detail further, up to this point, the recombination and motion of carriers in the vicinity of NRCs at the nanometer scale has rarely been reported. In addition, though InGaN underlayers (UL) are prevalently used to improve the efficiency of LEDs, the essential merit of the UL is still unclear. Finally, the efficiency of blue LEDs drops dramatically when increasing the current density above 10 A/cm^2, which is denoted as "*efficiency droop*". Auger recombination has been experimentally proven as a predominant reason for the droop. However, it is still unclear in terms of such an efficient three-particle interaction process, which was expected to be insignificant in wide band gap semiconductors.

Through the use of nanoscopic and ultrafast spectroscopy techniques, the work of this thesis is dedicated to studying carrier recombination dynamics and its relation to the quantum efficiency of III-nitride LEDs, as summarized as follows:

(1) We directly probe exciton dynamics around an isolated single dislocation, by using time-resolved cathodoluminescence (TR-CL). The exciton diffusion length and effective area of the dislocation are deduced by modeling the CL decays across the dislocation, which reveals the intrinsic properties of dislocations as NRCs. The type of dislocation is confirmed by observing the energy shift of the exciton induced by local strain fields. Meanwhile, we demonstrate that the key role of the UL is to trap non-radiative point defects. Low-kV CL measurements provide strong evidences of annihilation of carriers by point defects at the nanometer scale and the change of diffusion length under different defect densities.

(2) We establish a comprehensive model to describe the carrier dynamics in m-plane InGaN/-GaN QWs taking into account the presence of excitons, residual doping, and phase-space filling. Based on picosecond time-resolved photoluminescence (TR-PL) and modeling, we estimate the amount of excitons in QWs at room temperature, and explain the interplay between excitonic population and electron-hole (e-h) plasma. Beyond the e-h plasma scenario, our study provides insight into the physical origins of radiative recombination in LEDs.

(3) By using high injection TR-PL at cryogenic temperatures, we demonstrate evidence that carrier localization in the InGaN/GaN QWs plays a crucial role in intensifying the Auger process, which is linked to the relaxation of momentum conservation by the alloy disorder. Furthermore, we study the impact of different densities of point defects on efficiency droop in InGaN/GaN QWs at 300 K. This study suggests an extra efficiency loss, which is likely related to a defect-assisted Auger process. We derive a linear relation between Shockley–Read–Hall (SRH) and defect-assisted Auger recombination, which implies SRH-type defects can be the scattering centers for Auger recombination.

(4) We study highly efficient single InGaN/GaN core-shell microwires, in order to evaluate their potential for micro-/nano- LEDs and mitigating the droop. We decompose radiative and non-radiative lifetimes of carriers in the sidewall m-plane QW along the wire by spatial mapping of TR-CL from 4 to 300 K, which provides nanoscopic insight on the carrier dynamics in the presence of growth induced gradient of In content. By using high injection TR-PL at low temperature, we observe significant variation of Auger recombination in the active layer, which can be attributed to a different degree of alloy disorder.

Keywords: Gallium nitride, III-nitrides, quantum wells, quantum efficiency, LEDs, time-resolved cathodoluminescence, photoluminescence, dislocation, defect, Auger recombination, excitons, electron-hole plasma, Mott-transition, core-shell QW structures.

Résumé

Depuis l'article fondateur sur les premières diodes électroluminescentes bleues (LED, pour light emitting diode) à base d'InGaN de Shuji Nakamura et al. en 1994, les semi-conducteurs nitrures d'éléments III ont été l'une des plateformes les plus fructueuses pour les dispositifs optoélectroniques. Ainsi, le prix Nobel de physique en 2014 a récompensé « l'invention de diodes électroluminescentes bleues efficaces qui ont permis la réalisation de sources lumineuses blanches et économes en énergie ». Aujourd'hui, les LEDs bleues contenant des puits quantiques InGaN/GaN atteignent des efficacités quantiques internes de plus de 85%, même en présence de densités de dislocations élevées ($>10^8$ cm^{-2}), qui agissent pourtant comme des centres de recombinaison non-radiative (NRCs, pour non-radiative recombination centers). En fait, il est largement accepté que la localisation des porteurs de charge induite par le désordre d'alliage aléatoire de l'InGaN est la principale raison de l'insensibilité aux défauts des porteurs dans les puits quantiques, et ce par la réduition de la diffusion des porteurs de charges vers les NRCs.

Malgré le succès de cette technologie, l'efficacité quantique est encore limitée en ce qui concerne les LEDs de forte puissance, les LEDs émettant dans le vert et le rouge et celles de taille micrométrique. En effet, la dynamique de recombinaison des porteurs de charge interagissant avec le désordre d'alliage, les dislocations et les défauts ponctuels n'a pas encore été entièrement élucidée, préalable essentiel pour aborder ces problèmes. Premièrement, la recombinaison et la dynamique des porteurs à l'échelle nanométrique à proximité des NRCs ont rarement été reportés. Deuxièmement, bien que les sous-couches InGaN (UL pour underlayer) soient couramment utilisées pour améliorer l'efficacité des DEDs, le mécanisme sous-jacent n'a toujours pas été clairement identifié. Troisièmement, l'efficacité des LEDs bleues diminue considérablement lorsque la densité de courant augmente au-dessus de 10 A/cm^2, ce que l'on appelle chute d'efficacité ou efficiency droop en anglais. Les recombinaisons de type Auger se sont avérées expérimentalement être un facteur prédominant dans cette chute d'efficacité. Cependant, il n'est pas encore clair pourquoi ce processus d'interaction à trois particules est si efficace dans le cas des nitrures d'éléments III. En effet, les recombinaisons Auger devraient être négligeable dans le cas des semi-conducteurs à large bande interdite. Grâce à l'utilisation de techniques de spectroscopie nanoscopique et ultra-rapide, les travaux de cette thèse se sont consacrés à l'étude de la dynamique de recombinaison des porteurs afin de quantifier l'efficacité quantique des LEDs à base de nitrure d'éléments III, comme résumé ci-dessous :

(1) Nous étudions directement la dynamique d'un exciton autour d'une dislocation isolée, en utilisant la cathodoluminescence à résolution temporelle (TR-CL pour time-resolved cathodoluminescence). La longueur de diffusion de l'exciton et la surface effective de la dislocation sont déduites en modélisant les décroissances de CL à proximité de la dislocation.

Le type de dislocation est confirmé par l'observation du déplacement d'énergie de l'énergie de bande interdite induit par les champs de déformation électrique locaux. De plus, nous démontrons que le rôle essentiel de l'UL est de piéger les défauts ponctuels non-radiatifs. La mesure de la CL à faible tension d'accélération fournit des preuves solides de la recombinaison des porteurs par des défauts ponctuels à l'échelle nanométrique ainsi que de la variation des longueurs de diffusion pour différentes densités de défauts.

(2) Nous établissons un modèle complet pour décrire la dynamique des porteurs dans les puits quantiques InGaN/GaN crûs sur GaN plan m en tenant compte de la présence d'excitons, de dopage résiduel, et du remplissage de l'espace de phase, basé sur les mesures de photoluminescence à résolution picoseconde (TR-PL). Nous estimons ainsi la quantité d'excitons dans les puits quantiques à température ambiante et expliquons l'interaction entre la population excitonique et le dopage résiduel. Au-delà de l'image classique de recombinaisons par des paires électrons-trous, notre étude fournit un éclairage différent sur les origines physiques de la recombinaison radiative dans les LEDs bleues.

(3) En utilisant la TR-PL sous forte injection à des températures cryogéniques, nous montrons ensuite que la localisation des porteurs dans les puits quantiques InGaN/GaN joue un rôle crucial dans l'intensification du processus Auger, en lien avec la relaxation de la conservation du moment cinétique par le désordre d'alliage. En outre, nous étudions plus en détail l'impact des différentes densités de défauts ponctuels sur la chute d'efficacité des puits quantiques InGaN/GaN à 300 K sous forte densité de courant. L'étude suggère une perte d'efficacité supplémentaire, qui est probablement lié au procédé Auger assisté par un défaut. Nous dérivons une relation linéaire entre les recombinaisons Shockley-Read-Hall (SRH) et les recombinaisons Auger assistées par un défaut, ce qui suggère que les défauts de type SRH peuvent être les centres de diffusion de la recombinaison Auger.

(4) Nous étudions enfin des microfils cœur-coquille InGaN/GaN très efficaces, afin d'évaluer leur potentiel pour des applications de type micro/nano-LEDs. Nous décomposons les durées de vie radiative et non radiative des porteurs dans le puits quantique plan m le long du fil par cartographie spatiale de TR-CL pour des températures allant de 4 à 300 K, ce qui fournit une vision nanoscopique de la dynamique des porteurs en présence d'un gradient de composition d'indium induit par la croissance. En utilisant la TR-PL sous forte injection à basse température, nous avons observé une variation significative de la recombinaison Auger dans la couche active, qui peut être attribuée à un degré différent de désordre d'alliage.

Mots clefs : Nitrure de Gallium, nitrure d'éléments III, puits quantiques, efficacité quantique, LEDs, cathodoluminescence à résolution temporelle, photoluminescence à résolution picoseconde, dislocation, défaut, recombinaison Auger, exciton, plasma électrons-trous, transition de Mott, hétérostructures cœur-coquille.

Contents

Contents

Introduction

The objective of this thesis is to unveil the physics related to the limitations for achieving ultimate efficiency in III-nitride LEDs using nanoscopic ultrafast spectroscopy techniques and to provide relevant solutions. The thesis is constructed as following:

Chapter 1 introduces the structure and optical properties and III-nitride semiconductors. The specific properties and theoretical background of InGaN/GaN QWs are further clarified. In the end, a section delivers an overview of III-nitride LEDs and the main issues related to their quantum efficiency.

Chapter 2 introduces the nanoscopic and ultrafast spectroscopy techniques used in this thesis, which include picosecond time-resolved photoluminescence, low-kV cathodoluminescence, and time-resolved cathodoluminescence with nanometer and picosecond resolutions.

Chapter 3 addresses the impact of dislocations on the efficiency of LEDs. To this end, TR-CL is employed to characterize exciton recombination dynamics at the nanometer scale around a single dislocation in bulk GaN. To identify the type of dislocation, modeling of the distribution of local strain fields is used to reproduce the observed nanoscale energy shifts of exciton emission. By recording variations of the exciton lifetime and CL intensity across an isolated dislocation, we gain access to the exciton diffusion length and the effective area of the dislocation by a recombination-diffusion model [1]. Collaborating with our epitaxy team, we clarify the historical confusion surrounding the merit of UL for efficiency improvement in III-nitride LEDs. Picosecond TR-PL and low-kV CL experiments are performed to understand the impact of such an UL on the density of point defects in InGaN active layers.

Chapter 4 provides a comprehensive picture about the origin of radiative recombination, compared to the standard e-h pair scenario. Hence, we study the interplay between excitons and e-h plasma in m-plane InGaN/GaN QWs, by using TR-PL. To decompose the radiative recombination channel into an excitonic and an e-h plasma contribution, a model is developed to extract their radiative lifetimes and density ratio based on Fermi's golden rule and first-order corrected Saha's equation [2].

Chapter 5 investigates the influence of carrier scattering on indirect Auger processes in InGaN/GaN QWs. Here, we monitor the differences in the PL decay from QWs with different degrees of carrier localization, and develop a model to accurately predict Auger recombination coefficients [3]. Moreover, based on our understanding of the role of the InGaN and InAlN ULs on the point defect density [4], we study the impact of point defects on Auger recombination in InGaN/GaN QWs in the droop regime.

Chapter 6 studies the optical properties of single InGaN/GaN core-shell microwires provided by an industrial partner, to evaluate their potential for highly efficient micro-/nano- devices. Here, we probe the temperature dependent carrier dynamics along the wire by TR-CL, to characterize the radiative and non-radiative lifetimes of carriers in m-plane active layers. By analyzing the optical properties in the spectral, spatial and temporal domains, this work provides nanoscopic insight into the carrier dynamics influenced by alloy fluctuations and point defects [5]. High injection TR-PL is employed as well to study the impact of the intrinsic homogeneity of the microwires on Auger recombination.

Chapter 7 summarizes major the results of this thesis and gives the prospective based on this study.

1 III-nitride semiconductors

This chapter first provides an overview of the basic properties of III-nitride materials and the main features of III-nitride QWs, which gives the basis for the studies detailed in the following chapters. A general introduction on LEDs is then given, which delivers the current status and issues regarding the efficiency of GaN-based LEDs. Finally, the overall objectives and outlines of this thesis are summarized.

1.1 Structural and optical properties

III-nitride semiconductors are typically bound in two forms: either the metastable cubic zinc-blende phase, or the thermodynamically stable hexagonal wurtzite one. Note that all III-nitride devices are based on the wurtzite structure, we will focus on the fundamental properties originating from this crystalline phase. Figure 1.1 illustrates schematically an ideal wurtzite structure, which features C_{6v}-symmetry and is characterized by the a and c lattice parameters, with ratio of $c/a = \sqrt{8/3}$. Each atom is tetrahedrally surrounded by four other counterpart atoms, with the orientation governed by the sp^3-hybridization of orbitals. The cations and N-atoms are arranged in two hexagonal close-pack lattices shifted relative to one another by $u \cdot c$ along the [0001] direction, where u=3/8 is the internal displacement parameter. The specific lattice parameters of the binary III-nitride compounds at room temperature are shown in Table 1.1. Slight deviations from the ideal c/a ratio and u are observed for III-nitrides compounds, mainly due to the strong ionicity of the bonds. The lattice constants of ternary alloys In$_x$Ga$_{1-x}$N and Al$_x$Ga$_{1-x}$N are given by the Vegard's law, i.e. a linear interpolation of the lattice parameters of their respective binary constituents.

Table 1.1 – Lattice parameters of the wurtzite GaN, InN, AlN binary compounds at room temperature.

lattice parameter	GaN	InN	AlN	ideal
c	5.186	5.704	4.981	-
a	3.189	3.538	3.112	-
u	0.379	0.377	0.387	0.375
c/a	1.626	1.612	1.601	1.633

The lack of inversion symmetry in the wurtzite structure introduces the displacement of the

(a)

[0001] *c*-plane

○ metal atoms

● N-atoms

c

u·c

a

[1̄210] *a*-plane

[101̄0] *m*-plane

(b)
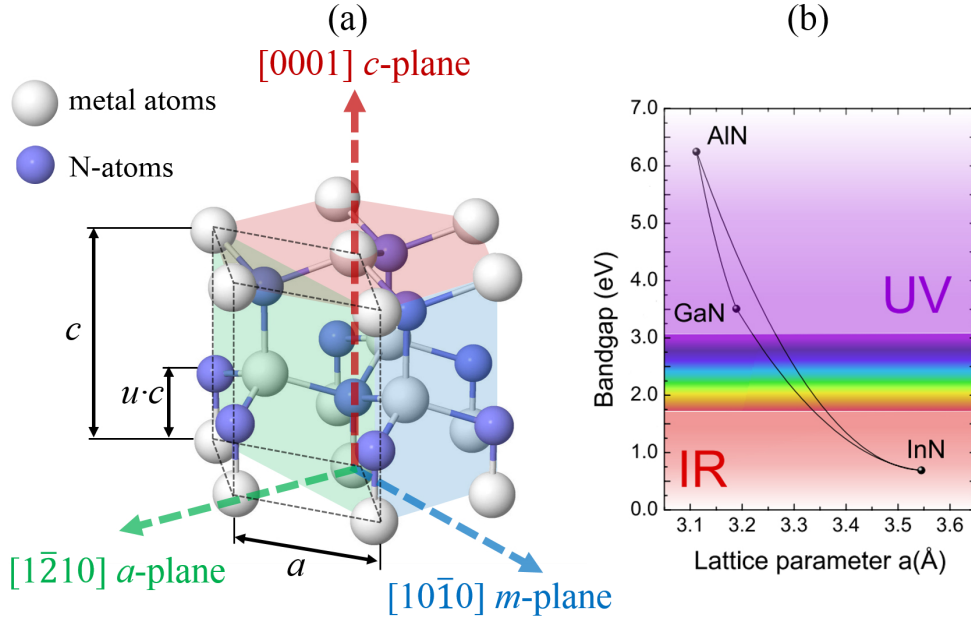
Figure 1.1 – (a) Hexagonal wurtzite primitive cell of III-nitride materials. *a* and *c* are the lattice constants in one of the unit cells (dashed frame) and the most-common surface planes are shaded by different colors; (b) Bandgap of wurtzite III-nitride compounds versus in-plane lattice constant *a* at room temperature.

negative and positive charge barycenters, introducing a permanent dipole moment, which results in a spontaneous polarization P^{sp} along the [0001̄] direction. Moreover, when the crystal lattice is subjected to deformation, any change in the crystal anisotropy also induces a large piezoelectric polarization P^{pz} along the *c*-axis. As shown in figure 1.1, the *c*-plane (0001), also referred to as polar orientation, is the predominant growth orientation for commercial III-nitride devices, thanks to its mature growth. Nonetheless, the polarization induced quantum-confined Stark effect (QCSE) (see section 1.2.1) limits the radiative rate of active layers. In the meantime, non-polar planes, i.e., the (1̄210) *a*-planes and the (101̄0) *m*-planes, raise interest for their advantages related to non-polar properties. Additionally, semi-polar orientation, for example the (202̄1)-plane, reveals potential for the realization of LEDs and laser diodes in the green spectral range, thanks to higher indium incorporation.

The wurtzite structure determines the electronic energy-momentum ($E − k$) dispersion of III-nitride materials. For example in figure 1.2(a), the calculated band profile of GaN within the first Brillouin-zone presents its direct band gap at the Γ-point, which indicates efficient light-matter interaction. For small momenta around the Γ-point, the corresponding $E − k$ dispersion of electrons can be expressed in the parabolic approximation:

$$E_c(\mathrm{k}) = E_c(0) + \frac{\hbar^2 k_\perp^2}{2m_\perp^*} + \frac{\hbar^2 k_\parallel^2}{2m_\parallel^*},$$

(1.1)

where $\hbar$ is the reduced Planck-constant. Due to the uniaxial symmetry, the wave vector is decomposed into two components: $k_\parallel$ along the *c*-axis and the in-plane $k_\perp$ term perpendicular
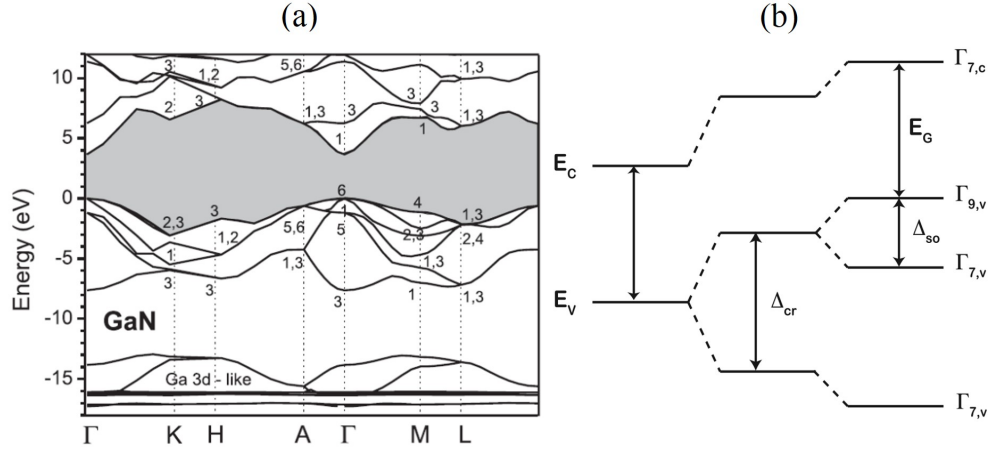
Figure 1.2 – (a) Calculated band structures of GaN in the first Brillouin-zone; (b) Degeneracy lifting of GaN valence band edge by crystal field splitting (Δ_{cr}) and the spin-orbit interaction (Δ_{so}) (adapted from [6]).

to the c-axis. The same is true for the effective mass of the electron $m_\parallel$ and $m_\perp$. The valence bands (VBs) can be described in a similar manner: their concave dispersion can be interpreted either by an electron with negative effective mass or by a positively charged quasi-particle with positive mass-the hole.

The lowest conduction band (CB) features s-orbital symmetry and is only spin-degenerated. Unlike the s-like CB, the three uppermost VB in III-nitrides possess p-orbital symmetry. The anisotropies of the wurtzite structure results in the lifting of VB degeneracy, as shown in figure 1.2. In detail, the energy splitting (given by the crystal-field energy Δ_{cr}) is closely related to the c/a-ratio. While in the case of GaN, Δ_{cr} is positive and on the order of 10-20 meV [7], it is negative for AlN. As the spin-orbit interaction is further taken into account, the higher-energy valence subband of GaN is split with an amplitude Δ_{so} of approximately 8 meV. The VBs exhibit Γ_9, Γ_{7+}, and Γ_{7-} symmetry in order of decreasing energy [8]. They are often called the heavy-hole (hh), light-hole (lh) and split-off (so) bands, but also commonly denoted as the A, B, and C valence bands, respectively.

As shown in figure 1.1(b), the band gaps of III-nitride materials go from the infrared, through the visible to the deep UV region. At 10 K, the band gap energy E_g of unstrained GaN is estimated to be 3.504 eV [9], and for AlN it is 6.089 eV [10]. For InN, after a long-standing controversy, its E_g value has been concluded to be around 0.7 eV [11]. The band gap of ternary alloys ($A_xB_{1-x}N$) can be described by the interpolation method:

$$E_g(A_xB_{1-x}N) = xE_g(AN) + (1-x)E_g(BN) - bx(1-x), \tag{1.2}$$

where b is the bowing factor to account for lattice distortion. When changing the temperature (T), the lattice dilatation leads to a reduction of E_g, which can be described by a semi-empirical equation called Varshni's law [12]:

$$E_g(T) = E_g(0) - \frac{\alpha T^2}{\beta + T}, \tag{1.3}$$

where α and β are material dependent parameters.

Apart from the free e-h picture, the Coulomb interaction between them can lead to the formation of a hydrogen-like quasi-particle called an exciton. The Hamiltonian for a single exciton in bulk material can be described as:

$$H_X = -\frac{\hbar^2}{2m_e^*}\nabla_{r_e}^2 - \frac{\hbar^2}{2m_h^*}\nabla_{r_h}^2 - \frac{e^2}{4\pi\varepsilon_0\varepsilon_r|r_e - r_h|} + E_g, \tag{1.4}$$

where $m_{e/h}^*$ denotes the effective mass of electron/hole, $r_{e/h}$ is the coordinate of the electron/hole, and ε_0 and ε_r are the vacuum and relative permittivity, respectively. Since the Coulomb term only influences the relative motion of electron-hole pairs, the equation can be simplified into center-of-mass and relative coordinates. The discrete exciton eigen-energies are thus expressed as:

$$E_X = E_g + \frac{\hbar^2 k^2}{2M^*} - \frac{E_B}{N^2}, \tag{1.5}$$

where $M^* = m_e^* + m_h^*$ is the exciton translation mass, k is the sum of electron and hole wave-vectors, N is the principle quantum number. E_B denotes the exciton binding energy:

$$E_B = \frac{\mu^* e^4}{2(4\pi\varepsilon_0\varepsilon_r\hbar)^2} = \frac{\mu^*}{m_0}\frac{1}{\varepsilon_r^2}\cdot 13.6 \text{ eV}, \tag{1.6}$$

where, $\mu^* = \frac{m_e^*\cdot m_h^*}{m_e^* + m_h^*}$ is the exciton reduced mass.

Analogous to the hydrogen atom, the effective Bohr radius of the exciton can be derived from:

$$a_B = \frac{4\pi\varepsilon_0\varepsilon_r\hbar^2}{\mu^* e^2}. \tag{1.7}$$

In bulk GaN, the experimentally measured E_B is as large as 26 meV, giving an estimated $a_B \approx 3$ nm, which suggests that excitons are robust even at room temperature. Comparatively, at low temperature, due to the presence of impurities, excitons usually bind to these impurities to form complexes, such as neutral donor excitons (D°X) and acceptor bound excitons (A°X).

1.2 III-nitride quantum wells

1.2.1 Quantum-confined Stark effect

The active region in III-nitride LEDs and laser diodes is usually made of QWs. The confinement energy and envelope wave function of carriers can be described by the Schrödinger equation:

$$\left[-\frac{\hbar^2}{2m_z^*(z)}\cdot\frac{\partial^2}{\partial z^2} + V_{QW}(z)\right]\Psi(z) = E\Psi(z), \tag{1.8}$$

where V_{QW} is the confinement-potential along the growth direction z. In the polar and semi-polar orientation, V_{QW} is modified by a built-in electric field F_{QW} due to the presence of polarization charges at the interfaces. This electric field induces a shift of transition energy

compared to the rectangular QW case and a separation of e-h envelope wave functions.

In general, F_{QW} in the QW can be calculated from the combination of Gauss's law and the electrical neutrality condition. This leads to an expression for the built-in electric field along the $[000\bar{1}]$ direction in a single QW (SQW):

$$F_{SQW} = \frac{P_B^{sp} - P_W^{sp}}{\varepsilon_W} + \frac{P_B^{pz} - P_W^{pz}}{\varepsilon_W}, \tag{1.9}$$

where the subscripts W and B stand for QW and barrier, respectively, and ε_W is the dielectric constant of the QW. The polarization can be derived from the work of V. Fiorentini et al. via *ab initio* calculations, detailed in Ref. [13].

In the case of multi-quantum well (MQW) samples, due to a partial redistribution of the electric field in the barriers, the electric field in each well is decreased compared to the case of a SQW. This is known as the geometrical effect and is given by the following equation which depends on the sample geometry [14, 15]:

$$F_{MQW} = F_{SQW} \frac{\varepsilon_W l_B}{\varepsilon_W l_B + \varepsilon_B l_W}, \tag{1.10}$$

where ε_B is the barrier dielectric constant, and l_W (l_B) is the well (barrier) thickness.

When carriers are present in the QW, they can screen the internal electric field. The reduction of the QCSE as a function of carrier density can be estimated through the solution of two coupled equations: the Schrödinger and the Poisson equation. Numerically, these two equations are solved self-consistently as detailed in Ref. [16]. The one-dimensional Poisson-equation is expressed as:

$$\frac{\partial^2}{\partial z^2} \Phi(z) = -\frac{\rho(z)}{\varepsilon_0 \varepsilon_r}, \tag{1.11}$$

where $\Phi(z)$ is the electric potential and $\rho(z)$ is the differential QW charge carrier density:

$$\rho(z) = -e \cdot n_{QW} \cdot \left[|\Psi_e(z)|^2 - |\Psi_h(z)|^2 \right], \tag{1.12}$$

where e is the electron charge and n_{QW} is the density of e-h pairs in the QW.

1.2.2 Excitonic effect and Mott transition

When the QW width is of the order or smaller than the bulk exciton Bohr radius, the strong confinement enhances the 2D exciton binding energy. In the extreme case of an infinitely thin and deep QW, the relation between the exciton binding energy in the QW and its value in a bulk structure is expressed as [17]:

$$E_B^{2D} = E_B^{3D} / (N - 1/2)^2, \tag{1.13}$$

which reveals that the ground state exciton binding energy E_B^{2D} is four times larger than the bulk one E_B^{3D}.

In a more practical scenario, the binding energy can be described by the Leavitt & Little approximation [18]:

$$E_{\text{B}}^{\text{2D}} = E_{\text{B}}^{\text{3D}} \int_{-\infty}^{+\infty} \left| \Psi_{\text{e},q_{\text{e}}} \right|^2 \left| \Psi_{\text{h},q_{\text{h}}} \right|^2 w \left[(z_{\text{e}} - z_{\text{h}}) / a_{\text{B}}^{\text{3D}} \right] \text{d}z_{\text{e}} \text{d}z_{\text{h}}, \tag{1.14}$$

where w is a non-analytical integral-function that can be approximated by a polynomial one. Meanwhile, the oscillator strength of 2D excitons is also enhanced by the confinement, which can be described as [17]:

$$\frac{f_{\text{X}}}{S} = \frac{4 \left| \mathbf{p}_{\text{cv}} \right|^2 p_{\text{QW}}^2}{m_0 E_{\text{X}}} \cdot \frac{1}{\pi a_{\text{B}}^2}, \tag{1.15}$$

where $\left| \mathbf{p}_{\text{cv}} \right|^2$ denotes the transition matrix-element, p_{QW} is the overlap of the e-h envelope wave function in the QW, and S is the unit surface area.

An exciton is categorized as a boson with a symmetric wavefunction and integer spin. In comparison, free electrons and holes are fermions with an anti-symmetric wavefunction and half-integer spin. The transition from a dilute exciton gas following Bose-Einstein statistics to an uncorrelated and conductive e-h plasma due to fermionic interactions at high carrier densities is usually referred to as the Mott-transition (MT) [19]. The symmetry properties of the wavefunction has profound implications for the statistics of particles, which leads to significant differences in the low-temperature behavior of systems of bosons and fermions. The MT is thus an important phenomenon for cavity-polariton condensation, polariton lasing, etc. Furthermore, from the practical point of view, the carrier density for MT coincides with the operation conditions of high power LEDs and lasers. A comprehensive understanding of the MT is important for optimizing devices.

The commutation rule for excitons in 2D-systems with exciton carrier density n_{X} has been evaluated to [20, 21]:

$$\left[\hat{d}_{\mathbf{k}_\perp}, \hat{d}_{\mathbf{k}'_\perp}^\dagger \right] = \delta_{\mathbf{k}_\perp, \mathbf{k}'_\perp} - O \left(n_{\text{X}} a_{\text{B}}^2 \right), \tag{1.16}$$

where δ is the Kronecker delta, $\hat{d}_{\mathbf{k}_\perp}^\dagger$ is the exciton creation operator with in-plane wave-vector $\mathbf{k}_\perp$, O is the finite error, which progressively increases as n_{X} raises. When the inter-particle distance becomes equal to the Bohr radius a_B, it gives an upper limit for the critical density $n_{\text{crit}}^0 = 1/\pi a_{\text{B}}^2$, called the hard-sphere criterion. The MT was initially claimed to be an abrupt first-order phase transition [19, 22], being featured as a discontinuous phase change; however, this statement was critically debatable. The latest theoretical studies suggest that the transition changes from discontinuous to continuous as the exciton binding energy increases [23]. In addition, recent evidence from experiment and theoretical calculations also indicates a rather anomalous Coulomb correlated e-h liquid phase next to the MT, which still sustains excitonic excitations despite being a degenerate Fermi liquid [23, 24]. The results obtained on GaN and ZnO epitaxial layers indeed confirmed a MT of continuous type [25, 26, 27]. In particular, Binet and co-workers investigated the optically-induced MT in bulk GaN layers deposited on sapphire [25]. They observed a smooth MT occurring around $2 \times 10^{18} \text{cm}^{-3}$ at low temperature and claimed a distinct rise of n_{crit} with temperature, which they ascribed to an increasing
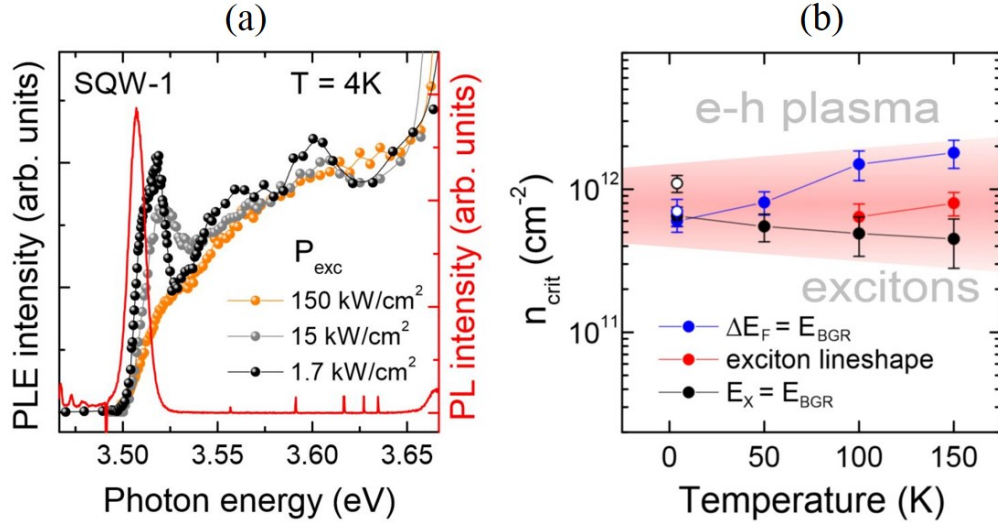
Debye-Hückel screening length.

Figure 1.3 – (a) Photoluminescence excitation spectra of a GaN/ $Al_{0.09}Ga_{0.91}N$ SQW as a function of excitation power density; (b) Dependence of n_{crit} on lattice temperature as deduced from various criteria: $\Delta E_F = E_{BGR}$, $E_X = E_{BGR}$, and exciton absorption lineshape (adapted from Ref. [16]).

To deliver an intuitive perspective into the MT, figure 1.3(a) shows power-dependent photoluminescence excitation (PLE) spectra recorded on a c-plane 3.2 nm-thick GaN/ $Al_{0.09}Ga_{0.91}N$ SQW at 4K, corresponding to a previous study performed in our group [16]. The low-injection spectrum exhibits a typical sharp exciton absorption peak. As excitation power P_{exc} increases by about one order of magnitude, the exciton absorption amplitude reduces apparently together with broadening of the linewidth. When increasing P_{exc} by another factor of ten, excitonic absorption features vanish completely, which evidences the crossover MT. Interestingly, the absorption edge appears at the former exciton position, confirming the picture of a band gap renormalization (BGR) induced MT. Apart from the exciton-lineshape criterion, figure 1.3(b) summarizes the temperature dependence of n_{crit} based on different MT-criteria. One criterion is that Coulomb screening and phase-space filling diminish the exciton binding energy E_B and eventually the exciton energy E_X coincides with the renormalized band gap E_{BGR}, which means that the exciton binding energy tends to zero. An additional criterion is according to the transparency limit $\Delta E_F = E_{BGR}$, i.e., when the quasi-Fermi level separation exceeds the band edge.

1.2.3 Carrier localization in quantum wells

Carrier localization induced by InGaN random alloy disorder is widely considered as one of the main reasons for highly efficient blue LEDs, which is supposed to decrease carrier diffusion towards NRCs [28]. From the physics point of view, alloy disorder creates Anderson-like localization resulting from the wavefunction interference of carriers experiencing potential fluctuations. The nanometer scale localization has profound impacts on the carrier recombination. In recent reports, the novel localization landscape (LL) theory enabled calculating the localization properties of carriers in the InGaN system including alloy disorder. The spatial

location of the eigenstates of carriers in a fluctuating potential $V(r)$ can be predicted by an effective confining potential $W(r) \equiv 1/u(r)$, via solving the following equation [29]:

$$\hat{H}u = -\frac{\hbar^2}{2m}\Delta u + Vu = 1, \tag{1.17}$$

where $\hat{H}$ is the Hamiltonian of eigenstates, and m is the effective mass of carriers. To construct the InGaN alloy, In atoms can be distributed in a 2D grid with a spacing corresponding to the average distance between cation atoms ($a = 2.83$ Å), and governed by a binomial distribution with an average circular area (radius ≈ 0.6 nm) [30, 31, 32]. This average area accounts for smoothing the rapidly oscillating distribution of atoms, while preserving the effects of disorder on the electronics properties. The fluctuations of the valence (conduction) band potential $V(r)$ can be simulated by the about 0.3(0.7) of band gap variation of InGaN calculated by the interpolation method [30, 33, 34]. In addition, the constructed $\hat{H}$ can also be used for calculating the ground state using the Schrödinger equation. For example, figure 1.4 illustrates the simulated 2D potential fluctuation of hole in the m-plane with an In composition of 11%. It suggests spatial carrier localization on the order of 3 nm dimension, defined by the individual potential minima.
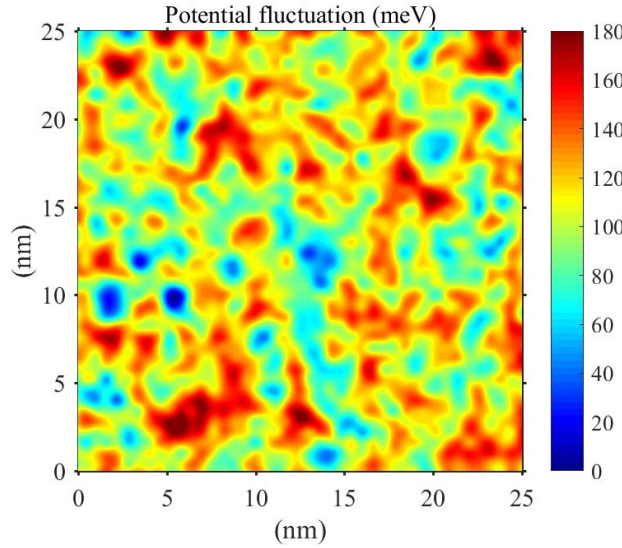
Figure 1.4 – Simulated potential landscape of an m-plane hole in the A valence band, with 11% In content, ~0.6 nm diameter of average area, 0.58 m_0 effective mass [3].

1.3 On the efficiency of III-nitride LEDs

Over the last 15 years, the luminous efficacy of white LEDs has improved from ~25 lm/W to over 160 lm/W, which is higher than any conventional light sources. The achievement is mainly attributed to the realization of highly efficient blue LEDs based on InGaN/GaN QWs. The internal quantum efficiency (IQE) of LEDs is known as the fraction of e-h pairs in the active layers which recombine as photons. Blue LEDs grown on sapphire (0001) substrates currently achieve more than 85% maximum IQE [35], even with a high threading dislocation

density (TDD) of $\sim 10^8$ cm^{-2}, which act as NRCs. The defect-insensitivity of InGaN/GaN QWs was ascribed to the intrinsic properties of the InGaN alloy: carriers are strongly localized due to large potential fluctuations induced by random alloy disorder hindering their diffusion towards NRCs. Apart from that, the continuous optimization of the phosphor (matched to the human eye response) and package (optical scattering/absorption) efficiencies also greatly improved the ultimate luminous efficacy of white LEDs. The high efficacy together with an extended lifetime (>25,000 h) gives LED products a lower life cost of ownership compared to the conventional light sources. The contribution to energy saving by the LED technology has been already measurable and profound. By 2035, it could potentially save 500 TWh of primary energy per year, as predicted by the U.S. Department of Energy (DOE) [36]. Beyond that, LEDs pave the way for novel applications, which are not possible or economical by using previous lighting solutions.

1.3.1 Efficiency droop

However, based on the forecast of the DOE, the current LED technology has not yet reached its potentially ultimate efficacies, which are ~260 lm/W for the predominant phosphor-conversion (PC) architecture and ~330 lm/W for the color-mixed (CM) one at 35 A/cm^2 input current density, as shown in figure 1.5. Note that the current density around 35 A/cm^2
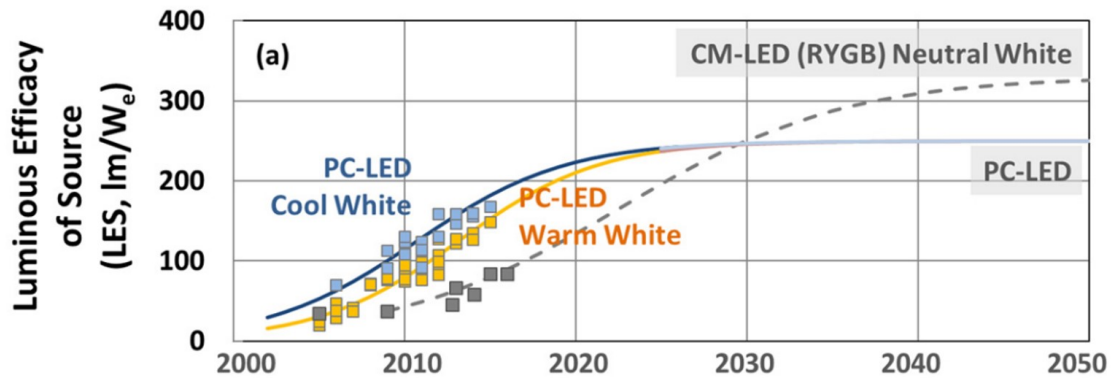
Figure 1.5 – (a) Luminous efficacies of commercial LED packages measured at 25 °C and 35 A/cm^2 input current density: blue = cool white (5700 K) data (squares) and logistic fit (line); orange = warm white (3000 K) data (squares) and logistic fit (line); approximate long-term-future potential efficacies of the PC-LED and RYGB (4-color: red, yellow, green, blue) CM-LED architecture is shown as the solid and dashed gray curves, respectively (adapted from Ref. [36]).

is a typical operation condition, which is high enough to enable relatively low cost, but low enough to avoid the most severe effects of efficiency droop as discussed below. The efficiency of blue LEDs has been improved immensely, but only at relatively low current densities. Even in state-of-the-art commercial LEDs, efficiency decreases dramatically at the higher current density, which are desirable for low cost for higher market penetration (figure 1.6). In the literature, this issue is referred to as *efficiency droop*. Generally, from about 10 A/cm^2 to 35 A/cm^2, the droop results in ~10% external quantum efficiency (EQE) loss, and from 35 A/cm^2 to 100 A/cm^2 causes another 15% penalty. It is worth noting that, as limiting thermal load is considered, improvement of efficiency droop by even a few percent contributes nonlinearly to the maximum achievable light output. For instance, assuming 10 W of heat dissipation

capacity, the improvement in wall plug efficiency (WPE) from 80% to 90% enhances the maximum light output from 40 to 90 W, before thermal degradation occurs. Consequently, the last few percentage improvement towards ultimate efficiency is essential in terms of cost and performance of high power LEDs.
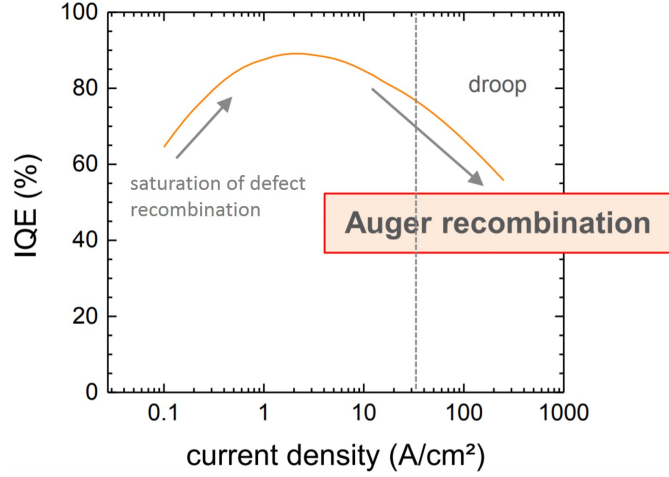

Figure 1.6 – IQE as a function of current density in high brightness commercial InGaN/GaN LEDs, which approach ~ 90% IQE at low current density, and are subject to ~40% internal losses at high current density (adapted from DOE solid stated lighting workshop [37]).

At the early stage, carrier overshoot and carrier leakage were proposed to account for the droop. However, the similar results observed from EL and PL droop indicate that the droop mechanism is due to an internal process within the active QWs, as carrier escape is negligible under photoexcitation of unbiased LED structures [38, 39, 40]. Moreover, in contrast to the strong temperature dependent slope of the current-efficiency dependence under low current, the slope is not affected by temperature in the droop regime [38], which suggests that the speculated inefficient carrier confinement or carrier density activated defect recombination [41] are unlikely origins of droop. It is worth mentioning that the study of Auger recombination relies on a precise determination of carrier density, radiative, and SRH recombination coefficients. In the conventional method based on electroluminescence (EL) on full LED structures and the oversimplified *ABC* model, the mutual effects resulting from structural complexities and over-fitting may conceal the major impacts [42].

Alternatively, as proven by the direct observation of linear correlations between the hot electron emission current and the *droop current*, Auger recombination is now widely accepted as one of the dominant and intrinsic mechanisms underlying the droop [43]. In the Auger process, the energy released through an e-h recombination event, is transferred via Coulomb scattering to a third particle that is excited to a higher-energy state. Theoretical calculations predict that direct Auger recombination obeying energy and momentum conservation is weak in III-nitrides, with a coefficient on the order of 10^{-34} cm^{6}s^{-1}, which cannot account for experimental measurements. In contrast, the calculated indirect Auger processes, mediated by electron-phonon, alloy scattering, and defects are much stronger and the derived coefficients are of a magnitude that has been shown to be sufficient to account for the droop of III-nitride LEDs [44, 45, 46]. Recent experimental studies further evidence that indirect Auger processes

can be particularly strong in InGaN/GaN QWs because of the scattering induced by alloy disorder and point defects [3, 47].

To circumvent the efficiency droop caused by Auger recombination, the general approach is increasing the rate of radiative recombination. Specifically, it includes: (1) composition and geometry engineering in the active region; (2) using alternative recombination mechanisms such as stimulated emission; and (3) decreasing carrier densities either via band-structure and transport engineering, or via alternative geometries such as stacked active regions connected through tunnel junctions. The prerequisite of these approaches is to understand and control the complex material epitaxy and device processing to maintain the high performance that has been achieved by painstaking optimization in current LED structures.

1.3.2 Issue of non-radiative centers in LEDs

On the other hand, instead of using the PC-LED architecture (in which the Stokes loss is unavoidable due to phosphor down conversion) another opportunity is move to CM architecture. While the performance of InGaN-based blue and violet LEDs has advanced rapidly
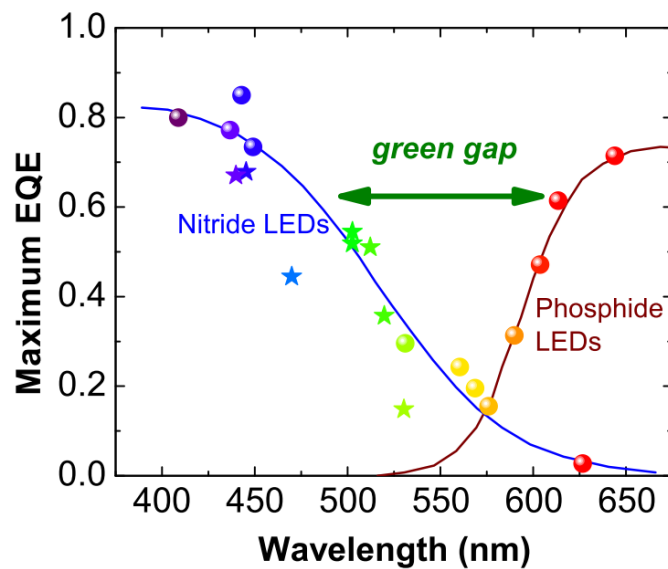
Figure 1.7 – Maximum EQE as a function of wavelength in different commercial III-nitride and phosphide LEDs (spheres). The lines are guides to the eye. The stars denotes the EQE of the green III-nitride single-quantum-well LEDs (adapted from Ref. [48]).

over the past couple of decades, increasing the indium composition to provide emission in the green spectral region results in a rapid reduction in quantum efficiency. CM-LEDs require individual units with ideal wavelengths at approximately 540 nm in green and 575 nm in amber, which are right in the so-called "green gap" region: the quantum efficiency reduces as the green emission wavelengths are approached, both from the short wavelength and the long wavelength sides, as illustrated in figure 1.7.

The inferior efficiency of InGaN-based green LEDs is related to the high indium content, which creates a high density of point defects and extended defects due to larger strains. There is

also increasing evidence that defect-assisted Auger recombination may limit the performance of green LEDs [47]. Apart from the high indium content induced NRCs, recent theoretical work indicates that strong carrier localization causes laterally uncorrelated electron and hole distributions, which reduces the radiative recombination of e-h pairs [48]. Though the QCSE increased by the high indium content will limit the IQE, the QCSE induced by the use of a wide QW geometry is beneficial for reaching green emission, which allows for lower indium content. However, to ensure an optimum use of this strategy, the precondition is the suppression of the non-radiative recombination rate by NRCs, so as to compensate the reduced radiative recombination rate by QCSE. In this respect, we recently elucidated the role played by the InGaN and InAlN UL on trapping non-radiative point defects, which can be essential for improving the IQE of active layer for green-red colors [49].

UV LEDs reveal numerous potential applications, such as water purification [50], document authentication, medical diagnostics and phototherapy [51]. Though still lower than blue InGaN LEDs at moderate current, the IQE of AlGaN-based UV LEDs emitting at 200-320 nm has been improved considerably through extended-defect engineering [52, 53, 54]. Figure 1.8
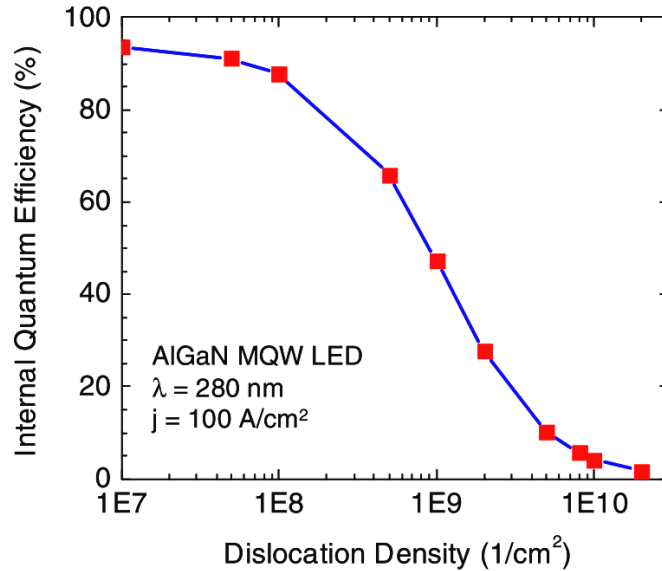
Figure 1.8 – Simulated IQE versus threading dislocation density for 280 nm UV LEDs (adapted from Ref. [54]).

indicates that as long as TDD in the active layer is less than 10^8 cm^{-2}, more than 80% IQE can be achieved. However, the strong absorption and in-plane polarization of optical transition limit the light extraction efficiency [52, 53]. In addition, the IQE of near UV near 340 nm is still limited, due to the weak carrier localization related to low Al content.

In parallel, as a disruptive technique, nano/micro- wires are a promising alternative to solve the remaining issues preventing the achievement of ultimate efficiency in III-nitride LEDs [55]. The benefits of nano/micro- wires technology are manifold: compared to the growth of planar layers, it is possible to grow nanowires on low cost substrates (e.g. silicon) without inducing dislocations, thanks to their high surface to volume ratio [56, 57]. In addition, it has been shown that strain relaxation by a free surface reduces the internal electric field in heterostruc-

tures embedded in nanowires [58], and improves the indium incorporation, which can be an option to solve the green gap issue [59]. Thanks to their non-polar heterostructures and their high aspect ratio, InGaN/GaN core-shell nanowires have been shown to be a promising structure to develop high efficiency LEDs. Indeed, these wires benefit from heterostructures without any internal electric field which increases the radiative recombination rate. Moreover, core-shell geometry could also increase the active region area for the same footprint area. This last property is of particular interest, because by reducing the current density for the same light output power one could drastically decrease the impact of the *droop*, regardless of its cause.

Since planar III-nitride LEDs have already achieved high efficiency and dominated the market of solid state lighting, the opportunity for LEDs based on nano/micro- wires are mainly targeting the micro-display market, because of their competitive advantage compared to etched planar LEDs in terms of surface defects. As shown in figure 1.9(a), when the LED dimension is decreased to less than 100 μm, the A coefficient starts to increase drastically, which is related to the non-radiative SRH-like recombination resulted from the LED perimeter. As a comparison, the wire-LED technology does not suffer from drop of efficiency with pixel size downscaling. Figure 1.9(b) clearly shows that the pixel size (the number of wires) has no impact on the efficiency of the wire-LED chip. Therefore, the wire-LED technology reveals noticeable advantage in developing highly efficient micro-LEDs, as the size is scaled down, as shown in figure 1.9(c) .
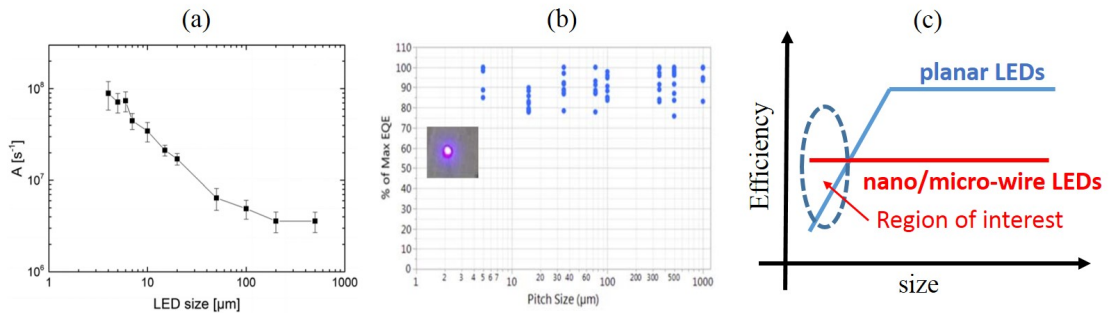
Figure 1.9 – (a) Extracted *A* coefficient versus LED size, adapted from Ref. [60]. (b) Evolution of the efficiency with regard to the pixel size of the wire-LED technology, inset, a blue nanowire emission device [adapted from Ref. [61]]. (c) schematic of the advantage of LEDs based on nano/micro- wires in terms of pixel size.

However, some uncertainties remain and should be answered to transform this potential into success. For instance, if the high surface to volume ratio provides a great advantage, it is important to investigate the effect of surface states and surface recombination on the efficiency of optoelectronic devices [62]. In addition, the inherent inhomogeneity of ternary nano-objects (such as InGaN nanowires) and the wire to wire variation and its consequence on working devices should be investigated in detail to conclude about the pertinence of the use of nanowires for optoelectronic devices.

2 Experimental setups

This chapter describes the main experimental techniques used in this thesis. The first section describes our picosecond TR-PL system, which is employed to study carrier recombination dynamics in III-nitride QWs, over a wide range of carrier densities and with a temporal resolution of few picoseconds. Second and third sections explain our original designed scanning electron microscope (SEM-) based continuous-wave (CW)/time-resolved CL setup, which provides simultaneously ultrahigh spatial and temporal resolutions, and allows us to directly observe carrier dynamics around nanostructures related to the quantum efficiency, including dislocations, V-pits, and step edges.

2.1 Time-resolved micro-photoluminescence

Picosecond photoluminescence spectroscopy is a prevalent tool to study charge carrier dynamics in semiconductors. As reported in ref. [63], the characteristic lifetimes involved in the relaxation and the recombination dynamics of carriers in semiconductors happens on the order of picoseconds. On the other hand, depending on the quality and the geometry of semiconductors, the recombination dynamics of carriers can take place at different time scales, from a few picosecond to the nanosecond and even the microsecond. Therefore, it requires ultrafast excitation and detection techniques to be able to capture this dynamics within the appropriate time scale. In our experiment, a frequency-tripled Ti:sapphire laser is used as excitation source, producing pulses with 2 ps duration and 280 nm wavelength. The transient luminescence is recorded by a streak camera with tunable time windows.

2.1.1 Excitation scheme of the pulse laser

The source combines a CW pump laser, a mode-locked Ti:sapphire oscillator, a pulse picker, and a frequency up-conversion unit, as presented in figure 2.1 and detailed below:

(1) The excitation source starts with a frequency-doubled Nd:YVO$_4$ CW laser. The water-cooled Nd:YVO$_4$ crystal is pumped by two laser diode bars (each binding 20 laser diodes) with 820 nm wavelength, which matches the absorption spectrum of Nd^{3+} ion. The design of diode bars is for optimizing the mode matching and reducing the lasing threshold. The active medium four-level Nd^{3+} ions emit at 1064 nm via their most probable transition: $^4F_{3/2}$-$^4F_{11/2}$. The

emission is further converted to 532 nm through second harmonic generation (SHG), using noncritically phase-matched and temperature-tuned lithium triborate (LBO) crystal, which gives 10 W of output power at maximum.

(2) The CW output is guided into a Ti:sapphire (Al_2O_3) oscillator. The Ti^{3+} ions are typically pumped in the green spectral region and cover a broad gain bandwidth between 670 and 1100 nm, which is imperative for ultrashort pulse generation and wide wavelength tunability. Depending on the details of the amplifying medium and the mirrors, the optimized gain of our oscillator is around 780-900 nm and maximized at 850 nm. For proper operation under high power pumping, the Ti:sapphire crystal requires a constant flow of cooling water and dry nitrogen purge. The cavity length is $L = 1.83$ m, which results in an ~12 ns round trip time for the pulses and ~80 MHz repetition rate. Even though theoretically the cavity allows longitudinal mode number in the order of $\sim 10^6$, the actual mode number is ~3000, which is limited by the presence of birefringent filter for wavelength tuning, acousto-optic modulator (AOM), and any other dispersions. Active mode-locking is realized by the AOM driven by a radio frequency (RF) generator that matches precisely the laser repetition rate. The global phase-locking gives rise to the concentration of all the electromagnetic energy within the cavity into a single pulse with ~2 ps duration and ~ 1.5 W output. The pulsed width is short enough to probe the carrier recombination dynamics occurring in the III-nitride semiconductors. A Gires-Tournois interferometer (GTI) is placed at the end of cavity to compensate the group velocity dispersion of the beam. In addition, even shorter pulses in the femtosecond region can be realized by self-mode-locking cavity using the Kerr effect.

(3) In order to adapt to the characteristic decay time of carrier, the pulse train passes subsequently through a pulse picker for tuning the temporal interval. In general, by using an electro-optical modulator with KD*P crystal, the beam is rotated by 90 degrees of polarization, when applying a bias along one of the crystal axes. The voltage is triggered by an electrical synchronous countdown signal, which is locked in time with the optical input stimulus. Sequentially, the rotated pulses pass through a beam-splitting polarizer.

(4) In order to reach the visible to UV wavelength range, the pulse is sent into a frequency up-conversion unit, which involves two steps of sequential harmonic generation. Firstly, a fraction of the fundamental is converted to the second harmonic in the 400-480 nm range with a maximum at 425 nm, in the beta barium borate (BBO) nonlinear crystal (doubler). The unconverted fundamental and the second harmonic are then coupled into the next BBO crystal (tripler) for sum-frequency mixing, which produces the third harmonic covering the 270-330 nm wavelength window with an optimum at 280 nm and ~5 mW of output power. Experimentally, the accurate phase matching, temporal and spatial overlaps, and proper focusing of the fundamental and second harmonic are crucial for optimizing the third harmonic generation. Additionally, a cylindrical lens is placed in the output path to collimate the elongated beam shape to a Gaussian one.

The output beam with a diameter of $\phi = 1 - 2$ mm is reflected towards the sample by a 80/20 beam splitter. To achieve high injection (in the degenerate regime with carrier densities >10^{12}cm^{-2}), an objective lens OL1 with a focal length $f_1 \approx 10$ mm and a numerical aperture N.A. ≈ 0.4 is used for focusing the beam below 7 μm diameter, estimated via $f = 2.44\lambda/\phi$. On the other hand, low injection condition is based on an achromatic lens with 120 mm focal
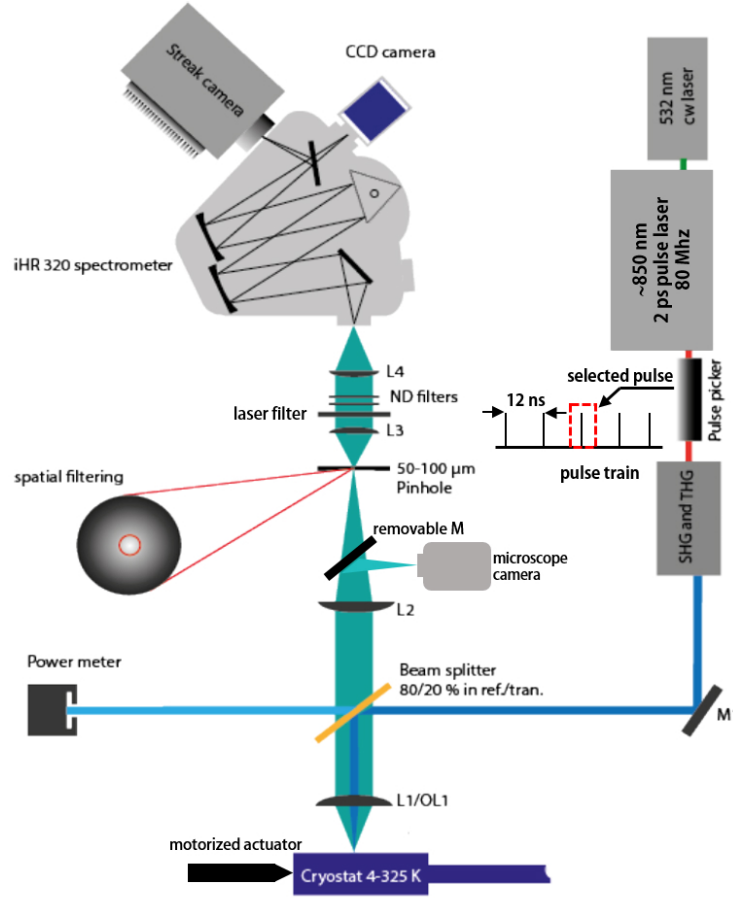
Figure 2.1 – Schematics of the TR-PL setup performed in illumination-collection mode. The excitation source is a pulse frequency-tripled Ti:sapphire laser with 280 nm wavelength, 2 ps pulse width, 80 MHz frequency. A pulse picker before the Ti:sapphire laser allows tuning the repetition from 80 MHz to 80 Hz. The PL signal is collected by two sets of projection microscopes, and subsequently sent into a monochromator with two exit ports connected to a time-integrated CCD camera and a synchronized streak camera. A pinhole placed in the collection path allows spatial filtering of the uniform part of the excitation spot, as shown in the inset of the figure.

length, which gives a larger focal spot of the beam with ∼ 80 μm diameter.

2.1.2   Collection scheme of the luminescence

When operating in the illumination-collection mode, the laser pulses and the PL signal are focused and collected by the same objective lens L1/OL1. The collection path combines two sets of projection microscopes. The L1/LO1 and lens L2 with f_2 = 300 mm operate as a projection microscope, which images the luminescence spot on the focal plane of L2 and magnifies it by f_2/f_1 times. In the high injection configuration, a spatial filter (pinhole) with a diameter of 50 μm is placed in the focal plane of L2. The spatial filter selects only the luminescence from the center region of excitation with highest and uniform carrier density. Figures 2.2 (a) and 2.2 (b) show the zero order PL signal (red spot) recorded by the CCD camera

with and without pinhole, respectively. Figure 2.2(c) further presents the corresponding time-integrated and normalized PL spectra. By implementing a pinhole, the absolute slope of the high energy tail in QW spectra reduces, which manifests Fermi filling effect. The second set of lenses combines L3 and L4 that refocuses the PL signal on the entrance slit of a monochromator with 32 cm focal length.

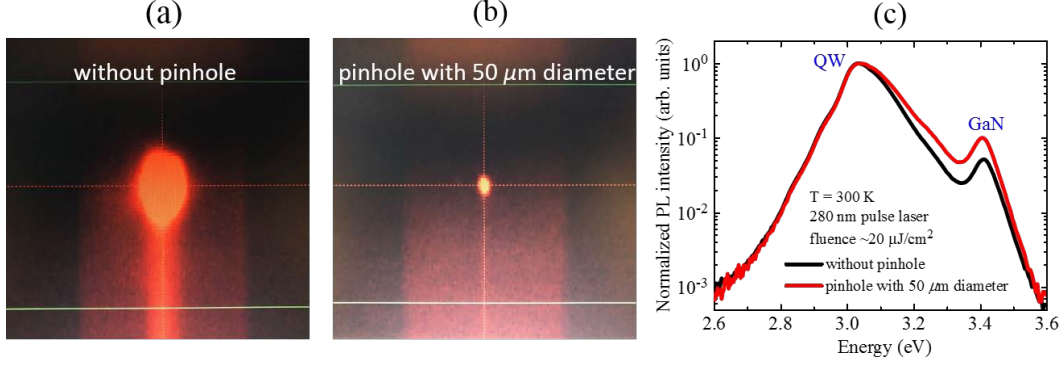| (a)	(b)	(c)
without pinhole	pinhole with 50 μm diameter	

Figure 2.2 – (a) and (b) show the zero order PL signal (red spot) recorded by the CCD camera with and without pinhole, respectively. (c) Corresponding time-integrated and normalized PL spectra with and without pinhole. By implementing a 50 μm diameter pinhole, the absolute slope in the high energy tail of QW spectra reduces, which suggests that a higher carrier density is observed due to Fermi filling effect.

Two sets of 1 inch wide gratings are used in this thesis with 150, 300, and 1200 grooves/mm blazed at wavelength of 500 nm, and 300, 600, and 1200 grooves/mm gratings blazed at 350 nm. The intrinsic spectral resolution of these gratings is defined by $\Gamma = \frac{E_c}{N_g g l}$, where E_c is the center energy of the luminescence, N_g is the diffraction order, g is the groove density, l is the width of the grating. Thus the intrinsic resolution of the gratings with 150, 300, 600, and 1200 grooves/mm is about 0.8, 0.4, 0.2, and 0.1 meV, respectively. The practical resolution is, however, one order of magnitude less, mainly limited by the size of the entrance slit of the spectrometer. It is worth to mention that the energy shift between two close spectra does not only depend on the gratings, but also relies on the position accuracy in the CCD camera. The spectral accuracy can be described by $\Gamma_p = \Gamma \frac{1.8}{SNR} \frac{1}{\sqrt{N_\Gamma}}$, where Γ is the practical grating resolution, SNR is the signal to noise ratio and N_Γ is the number of pixels within Γ. For instance, a 600 grooves/mm grating, with $\Gamma = 2$ meV, $N_\Gamma = 3, SNR \approx 50$ gives $\Gamma_p = 0.04$ meV, which allows to resolve small energy variations in III-nitride nanosctructures.

A Streak camera is implemented at one of the two exits of the monochromter, which enables capturing ultrafast light phenomena and measuring PL intensity as a function of time and wavelength. Figure 2.3 explains the general principle of the streak camera. The incident light is first focused on a horizontal slit, and then arrives at the photocathode, which converts light into a number of photoelectrons proportional to the intensity of the light. The electrons are accelerated by a pair of accelerating electrodes and travel through a pair of sweep electrodes, which is synchronized to the electrical trigger of the pulse picker. During the high-speed sweep, the electrons are deflected vertically at different angles, depending on their arrived times. The deflected electrons are multiplied by a micro-channel plate (MCP), and then
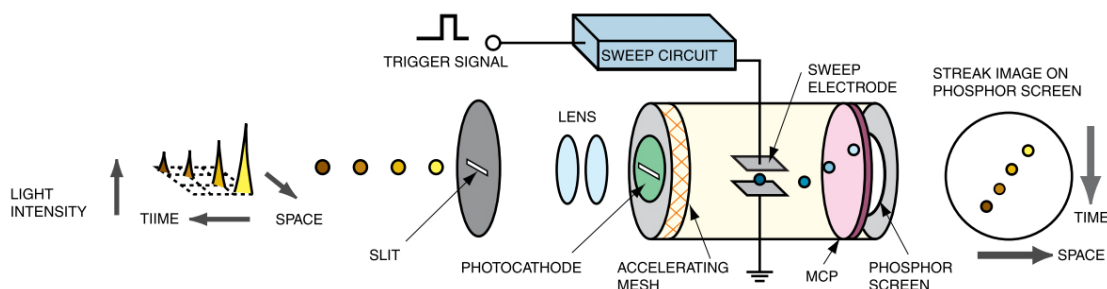
Figure 2.3 – Schematics of the operation principle of a streak camera. In general, the incoming photons at different time delays are converted into the photoelectrons by a photocathode. Afterwards, a sweep voltage deflects vertically the electrons to different positions on a phosphor screen. The time delay of the photons is therefore correlated with the difference in vertical position of the illumination on the screen. The lateral difference of the illumination stands for any other dimensional resolutions, which is the wavelength of the photons in this case. The intensity of incoming light corresponds to the brightness appearing on the screen [64].

bombard a phosphor screen. The brightness of the phosphor pixels is proportional to the intensity of the respective incident optical pulses. The horizontal direction of the phosphor image corresponds to the spectral dispersion of the incident light. We can thus access to the luminescence intensity mapping with temporal and spectral resolution from the phosphor screen. It is worth to point out that the temporal resolution of our setup is about 10-20 ps. Further improvement can be achieved by suppressing the delays induced by grating and trigger, imperfection of focusing, and trigger jitter.

In addition, a continuous-flow liquid-helium cryostat allows to vary the sample temperature between 4 and 300 K. A motorized micro-actuator enables moving the cryostat horizontally. A microscope camera is used for imaging microstructures.

2.2   Low-kV continuous wave cathodoluminescence

SEM is a powerful technique to obtain nanoscopic insight into semiconductors, which enables multidimensional analyses based on the information from secondary electrons (SE), backscattered electrons, Auger electrons, X-rays, and cathodoluminescence (CL). In particular, SE and CL signals are employed in this thesis to investigate the structural and optical properties at the nanometer scale in III-nitride materials.

The SE signal is widely used for characterizing the surface morphology, which originates from the ejected electrons of the sample atoms by inelastic interactions with the primary electron beam. SEs carry relatively low energy typically less than 50 eV, which can thus only escape from the near-surface regions within several nanometer depth [65]. The shallow volume of emitting SE also contributes to a small spatial extension and a high spatial resolution on the order of a few nanometers. Moreover, when the electron beam is injected near the edges of nanostructures, more SEs will escape from the sample, which enhances the SE emission. This is the so-called "edge effect". On the other hand, the impinging electrons generate e-h pairs by inelastic scattering. The cathodo-created carriers recombine during their diffusion and relaxation, which eventually produce the CL signal giving access to nanometer-resolved

optical properties.

The spatial resolution of CL mainly depends on the interaction volume and carrier diffusion. The interaction volume is related to the impinging electron trajectories in the specimens, which can be estimated via Monte-Carlo simulation [66]. Figure 2.4(a) reveals that, when the acceleration voltage elevates between 1 kV and 6 kV, all the lateral distributions of cathodo-created carriers highly concentrate around the center of the excitation spot and reduce drastically when moving away from the center. However, the lateral expansion increases from ~12
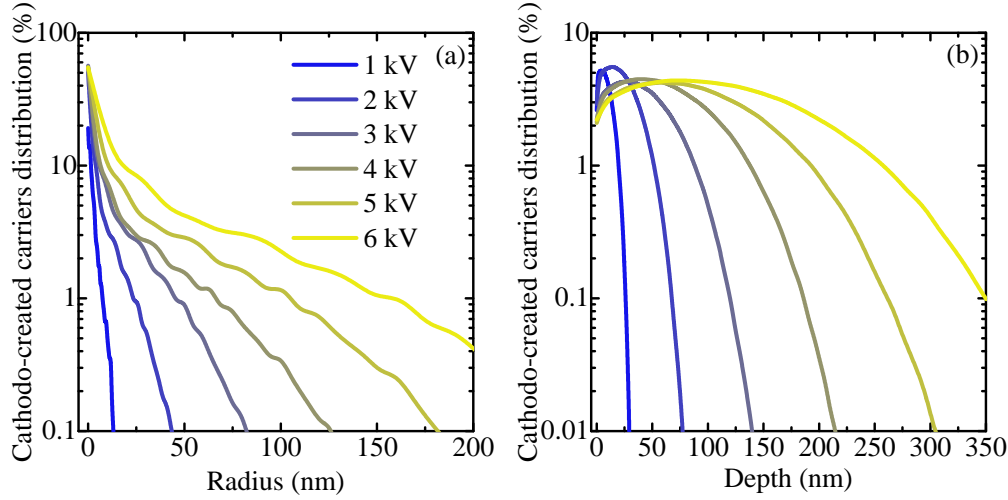

Figure 2.4 – (a) Monte-Carlo simulation of the cathodo-created carrier distribution by radius in bulk GaN by varying the acceleration voltage from 1 kV to 6 kV; (b) Corresponding carrier distribution by depth.

nm to ~200 nm, due to the increase of beam energy. Meanwhile, the carrier distribution by depth also extends from the near-surface region (~25 nm) to the inner part of the sample (~300 nm), as presented in figure 2.4(b). High spatial resolution and SNR of the CL signal can be achieved under low-kV excitation, by well-designing the sample layout with active layers beneath the surface, where having the maximum of vertical carrier distribution. Furthermore, the short carrier diffusion length also contributes to a better spatial resolution of CL, which is in the range of a few tens to hundreds of nanometers for III-nitride materials [67]. Therefore, low temperature, alloy disordered system, and a short carrier lifetime are favorable for achieving ultrahigh spatial resolution. Additionally, it is possible to estimate the density of e-h pairs generated in a semiconductor by an electron beam. It is usually admitted that the number of electron-hole pairs generated by a single incident electron corresponds to the beam energy divided by three times the sample band gap [68]. Consequently, the carrier density is on the order of $10^{10} - 10^{11}$ cm^{-2} in III-nitride materials.

Figure 2.5 shows a schematic of the SEM-CL system used in this thesis. The CW electrons emit from a Schottky field-emission electron gun (FEG) through thermal activation and tunneling effect, and are accelerated in the range of 1-6 kV.
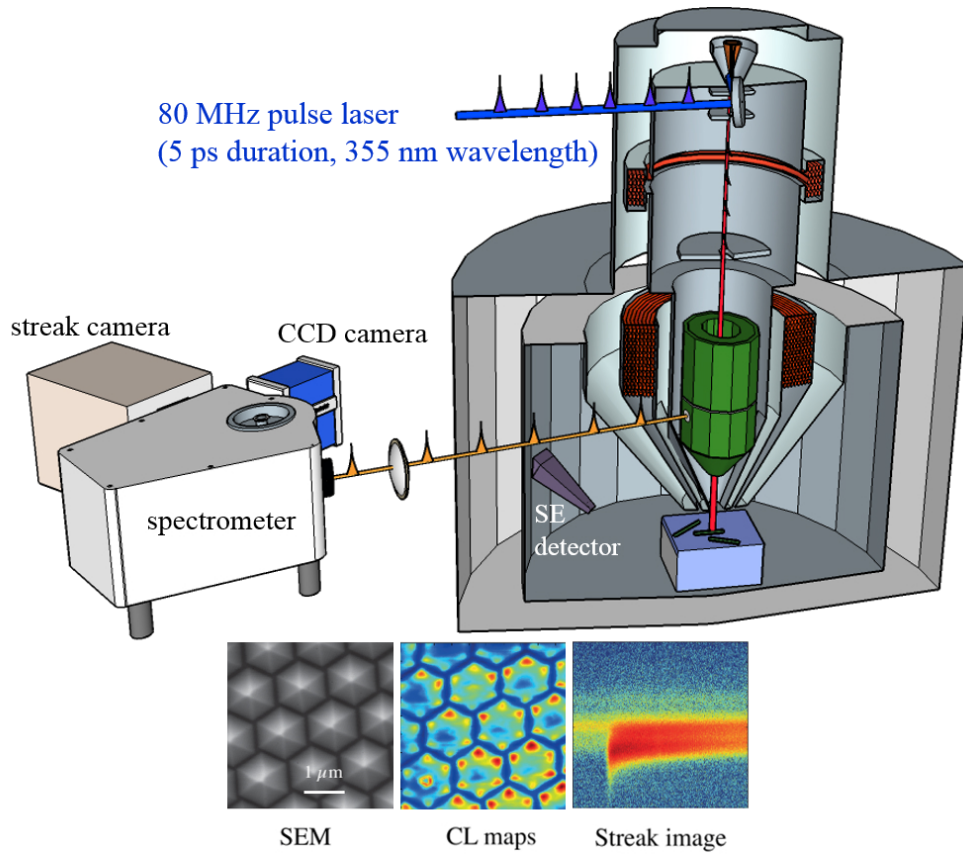
Figure 2.5 – Schematics of our SEM-CL/TR-CL setup. When operating in CW mode, a CW electron beam is emitted from a Schottky FEG by thermally activated tunneling effect. The electrons are subsequently accelerated along the column of the microscope. The CL is collected by using integrated optics and dispersed in a monochromator followed by a CCD camera. Meanwhile, SE images are recorded by an Everhart-Thornley detector. For comparison, in pulse mode, a pulse laser (5 ps duration, 355 nm wavelength) is focused on the tip of the gun to create electron pulses. Transient CL is detected by a streak camera. For example, the bottom three mappings are the SE image of GaN pyramids, the corresponding time-integrated CL intensity, and the streak image. Courtesy to Dr. Mehran Shahmohammadi.

Subsequently, the electron beam passes through the condenser lens and objective lens, and is focused on the surface of a sample, to a size about 1-10 nm diameter. Mappings of SE are acquired by an Everhart-Thornley detector installed on the sidewall of the sample chamber. The CL signal is simultaneously collected by a Cassegrain objective placed above the sample, and afterwards sent to a monochrometer and recorded by a time-integrated CCD camera. The sample stage is coupled with a nano-metric piezoelectric positioning system, and allows temperature tuning (4-300 K) by using a open-cycle helium cooling. The sample stage is designed for suppressing vibrations and drifts, and obtain a slow drift of ~100 nm/hour.

From the experimental point of view, to achieve high spatial resolution, high convergence of the first condenser lens is favorable for the subsequent focusing of the objective lenses, and the use of a small pinhole (25 μm diameter) between the two magnetic lenses is important for suppressing the energy dispersion of electrons. In addition, well-overlap of the focal points of

Cassegrain objective and electron beam is important to gain high SNR of CL.

2.3   Time-resolved cathodoluminescence

With the concept of combining the temporal resolution of TR-PL and the spatial resolution of an SEM, our lab, in collaboration with Attolight company, developed a unique TR-CL technique, which enables watching directly the ultrafast carrier dynamics at the nanometer scale [69, 70, 71]. The first realization of TR-CL with a ns time resolution has been reported in ref. [72]. Electron pulses were generated by the beam blanking technique, where the electron beam was deflected by a transverse oscillating electric field. Recently, a new beam blanking technique has been proposed to create ultrashort 100 fs electron pulses based on integrating a photoconductive switch with an electrostatic deflector [73]. Alternatively, our group took advantage of the photoelectric effect to generate ultrashort electron pulses. As demonstrated by ref. [74], a pulsed electron beam with ~10 ps duration can be obtained by exciting a 50 nm thick gold photocathode with the third harmonic of a mode-locked Ti:sapphire laser.

Our current TR-CL setup (Attolight Allalin Chronos 4027 system) is composed of three major units: a pulse electron generation unit, an SEM unit, and a transient CL detection unit. The extraction efficiency of photoelectrons was further improved by a combination of Schottky FEG and a pulse laser (355 nm wavelength, 5 ps duration, ~80 MHz frequency). As shown in figure 2.6, several kV extraction voltage is applied to the tip emitter of the gun, which reduces the potential barrier between metal and vacuum. Instead of thermally triggering electron tunneling, the laser pulse excite the electron from near-Fermi energy E_f to the high energy state, enhancing their tunneling probability. A small heating current in the range of the μA heats slightly the gun, for two reasons: (1) introducing flow of liquid metal to the tip from the reservoir for reducing the workfunction; (2) slightly elevate the electron population near the Fermi level, but without causing CW tunneling current. Ultimately, ~5 ps long electron pulses are generated, with a low mean beam current ~10 pA, which corresponds to 1-10 electrons per pulse. The compact SEM chamber is designed specifically to avoid any temporal broadening
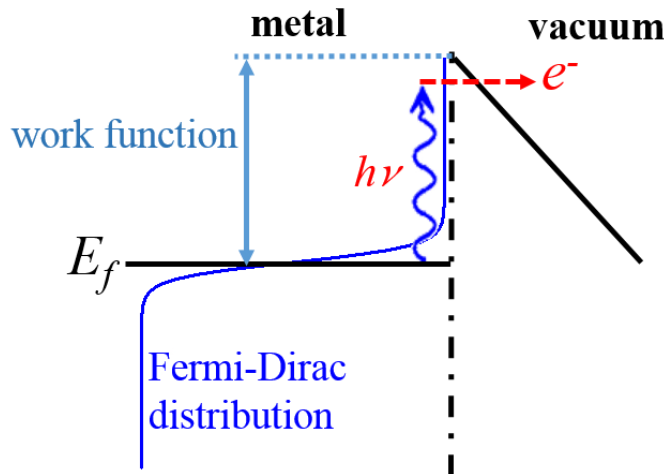

Figure 2.6 – Photoelectron emission process in a bias field emission excited by a laser pulse.

of the electron pulse during the traveling. As for the CW-mode, the pulsed electron beam is controlled by the magnetic lenses. The acceleration voltage in time-resolved mode is usually set to 6 kV, combined with a 100 μm pinhole for the balance in the spatial resolution and SNR of CL. When performing a SE mapping, the signal is only acquired during a few ps of pulse width, while noise is accumulated during the interval of each pulse, which consequently reduces the SNR and the resolution of SE imaging. Similarly to the collection of the TR-PL setup, the transient CL is sent to a monochromator, which is equipped on one of the exit ports with a streak camera synchronized with the laser, with temporal resolution better than 20 ps. This temporal resolution is determined by fitting a CL decay curve (see figure 2.7) using the following equation:

$$TRCL(t) = \frac{1}{2}\left(1 + \mathrm{erf}\left(\frac{t}{\sigma\sqrt{2}}\right)\right) \times \left(A_1 e^{-t/\tau_1} + A_2 e^{-t}/\tau_2\right), \tag{2.1}$$

where erf is the Gauss error function. We fit the TR-CL signal integrated over the QW emission of a core-shell nanowire at T=4 K. By this fitting, we can estimate an upper bound of the temporal resolution of our system. We extract a standard deviation of 8 ps (i.e a full width at half maximum (FWHM) = 19 ps). As a consequence, the temporal resolution is around 20 ps.
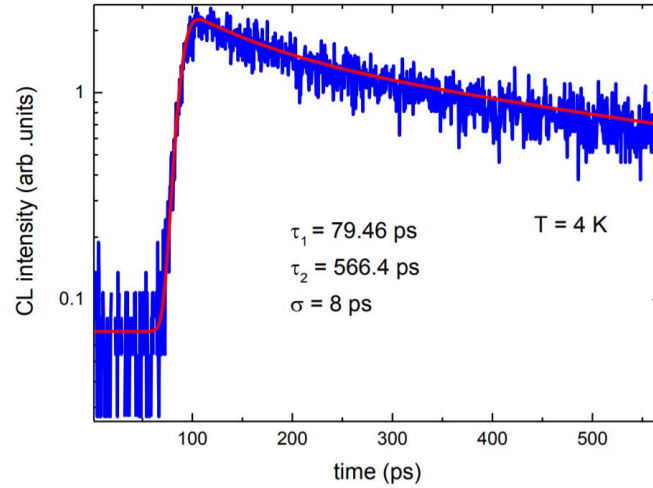

Figure 2.7 – TR-CL decay trace integrated over the QW emission of a core-shell nanowire at $T = 4$ K (blue) and its corresponding fit (red)

3 Nanoscopic insight into nonradiative recombination centers

3.1 Introduction

Dislocations are regarded as one of the NRCs that limits the quantum efficiency of III-V optoelectronic devices. However, despite a huge density of dislocation compared to other III-V materials, the adverse effect of dislocations is drastically reduced in III-nitride LEDs and a satisfactory efficiency can still be maintained. This unique behavior partly explains the success of III-nitride LEDs. However, up to now, there are no clear experimental indications on the carrier dynamics close to a dislocation, which requires sophisticated techniques to probe the motion and the recombination of carriers occurring in the nanometer and picosecond regimes. In this chapter, by using our original picosecond TR-CL setup with high spatial and temporal resolutions, we observe directly the motion of excitons in the vicinity of a dislocation in GaN and quantify the exciton dynamics around a single dislocation.

Besides dislocations, point defects such as impurities or vacancies are another common source of NRCs in III-nitride materials. In particular, deep level defects are detrimental to the efficiency of blue LEDs. Armstrong *et al.* pointed out that the density of NRCs in InGaN/GaN QWs decreases if a thick InGaN layer is deposited before the growth of the active region [75]. In fact, such an InGaN UL or InGaN/GaN superlattice (SL) is commonly used in high efficiency commercial blue LEDs. Its role is to trap surface defects (SDs) and avoid their further incorporation into the InGaN/GaN active region [76, 75, 77]. However, the use of InGaN UL leads to absorption in the UV regime, which is a shortcoming for UV LEDs. To exploit another potential UL that remains transparent in the UV range, we studied the defect trapping mechanism in InAlN UL/SL by TR-PL, and the nanoscopic optical properties in the active layer with different defect densities controlled by the InAlN UL/SL via low-kV CL.

3.2 Exciton dynamics at a single dislocation

3.2.1 Motivation

Blue InGaN/GaN LEDs on sapphire (0001) substrates are currently one of the most efficient lighting sources for energy saving, achieving above 85% IQE at low current density [35]. Indium fluctuations in the InGaN alloy have been proposed to be the main reason for such a high

efficiency [78, 79]. The high efficiency can be achieved even with high TDD $\sim 10^8$ cm^{-2} in the active layers, whose non-radiative character is evidenced by CL [80]. However, the efficiency severely drops in GaN-based LEDs with a lower indium composition, which corresponds to emission in the violet to near ultra-violet (UV) regions [81]. Violet LEDs on free-standing GaN substrates ($\sim 10^6$ cm^{-2} TDD) provide superior color rendering index (CRI) for white lighting [82] and are a promising approach to overcome the efficiency droop [42, 83]. As the dislocation density is above 10^9 cm^{-2}, it becomes a critical issue that limits the quantum efficiency of UV LEDs, which has weak carrier localization [84]. Therefore, to fully realize the potential of GaN-based LEDs emitting from violet to near UV wavelengths, it is essential to understand the carrier dynamics around dislocations.

CL is a powerful technique and is widely used to study the optical properties of GaN at the nanoscale [85, 86, 87, 88]. Since 1997, it has been confirmed, through a comparison between atomic force microscopy (AFM) and CL images, that dislocations act as NRCs [80]. The non-radiative dislocations have been further identified as pure edge or mixed (edge and screw) type using a comparison between plan-view transmission electron microscopy (TEM) and CL images. An effective radius R_{eff} of the dislocation has been proposed to explain the CL efficiency around the dislocations [89]. However, the information about carrier lifetime around the dislocations, which requires simultaneous picosecond temporal and nanoscale spatial resolutions, remains difficult to access. Furthermore, the influence of R_{eff} and the excitation volume on the CL intensity on a dislocation are still elusive.

Here, thanks to our picosecond TR-CL setup with ultra-high spatial ans temporal resolutions as detailed in Chapter 2, we investigated the exciton dynamics at $T = 10$ K on a single dislocation in bulk GaN grown by metal-organic chemical vapor deposition (MOCVD) [70]. We obtained the distributions of emission peak energies, effective lifetimes, and CL intensities around such a dislocation. By fitting the experimental data with a simple diffusion model, we were able to define the type of dislocation and extract R_{eff} and the diffusion length of excitons. These results give imperative information about the carrier dynamics around a dislocation and confirm the relevance of such a technique to elucidate the influence of dislocations on GaN-based LEDs.

3.2.2 Sample structure and general optical properties

The structure of the sample is the following: a 2 μm thick GaN layer is grown on a free-standing GaN (0001) substrate with non-uniform dislocation density (ranging from 1×10^6 cm^{-2} to 1×10^7 cm^{-2}), followed by a capping layer of 10 nm Al$_{0.05}$Ga$_{0.95}$N used as a protecting layer to reduce the influence of surface recombination. In figure 3.1(a), temperature dependent PL demonstrates that donor bound excitons D°X$_A$ (3.473eV at 15 K) dominates the spectrum in the 15–50 K range, whereas free exciton FX$_A$ gradually thermally activates and only becomes predominant above 70 K [90].

The strong luminescence from D°X$_A$ most probably comes from the high n-type doping ($\geq 2.5 \times 10^{18}$ cm^{-3}) inherited from the GaN substrate. Figure 3.1(b) shows the CL intensity mapping of the (0001) surface of the sample in continuous excitation mode at $T = 10$ K, and the linear grayscale indicates the CL intensity. The mean electron current is around 5 nA and the acceleration voltage is 6 kV. Such an acceleration voltage has been chosen as

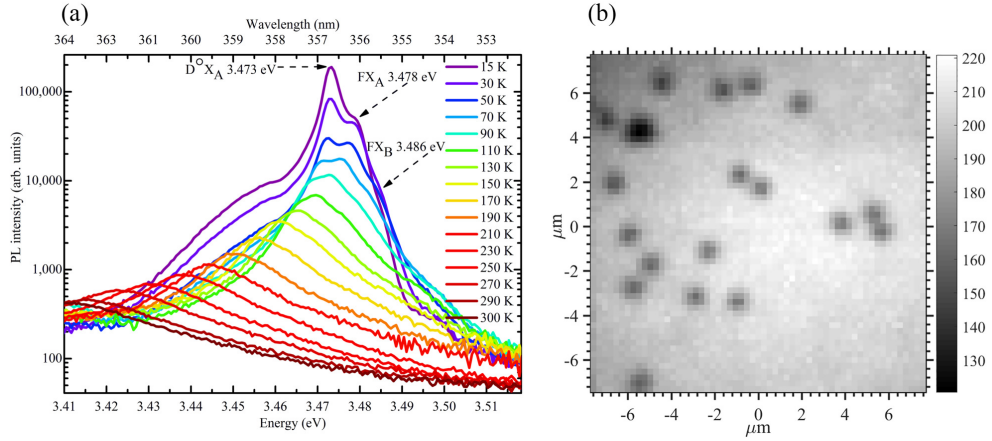Figure 3.1 – (a) Temperature dependent PL from T=15 K to 300 K using a 280 nm pulsed laser at a low fluence ($\sim$1nJ/cm^2), where D$^\circ$X$_A$ indicates the donor bound A exciton, and FX$_A$ and FX$_B$ are the free excitons at A and B valence bands, respectively. (b) CL intensity mapping under continuous excitation mode at T=10 K, where the dark spots indicate the locations of dislocations with an areal density $\sim 8 \times 10^6$cm^{-2}, and the greyscale indicates the CL intensity (arb. units) in linear scale.

a trade-off between the CL interaction volume and the yield of CL signal when working in pulsed excitation mode. The dark spots with lower CL intensity suggest the locations of dislocations acting as NRCs [80]. The average density of dislocations within this area (~ 240 μm^2) is $\sim 8 \times 10^6$cm^{-2}, which is within the order of magnitude of the dislocation density in the GaN substrate. It has been reported that the distribution of dislocations in this type of GaN substrate is non-uniform [91]. In our sample, the density of dislocations revealed by the CL can be as large as $\sim 4 \times 10^7$cm^{-2} in some small regions (~ 25 μm^2), whereas we did not observe any dislocations in some other parts of the sample.

3.2.3 Signature of strain field around a dislocation

To further understand the recombination dynamics of carriers on a single dislocation [92], we perform measurements in pulsed excitation mode at 10 K. Low temperature allows us to reduce the spectral linewidth due to the suppression of phonon scattering. It is a prerequisite to precisely observe whether or not the dislocation induces a local energy gradient and to probe whether or not this gradient could affect the carrier dynamics. Figure 3.2(a) presents the integrated CL intensity mapping around a dislocation at T = 10 K. The blue spot in the center with ~200 nm diameter shows the signature of a non-radiative dislocation. The CL intensity on the dislocation is ~50% lower than that of its surroundings. Figure 3.2(b) presents the corresponding mapping of the emission peak energy in the same area. The average energy all over the area is ~3.473 eV, which is consistent with the D$^\circ$X$_A$ emission [90]. More importantly, there is a dipole-like energy shift on the order of ~1.3 meV difference around the dislocation, as illustrated by the blue and red circles. Such a dipole behavior has been observed at several dislocations under different excitation conditions in our sample. Figure 3.2(c) presents the average spectra within each circle indicated in figure 3.2(b). The blue spectrum, which corresponds to the emission from the blue circle, presents a clear blue shift compared to the red spectrum from the red circle. This dipole-like energy shift clearly indicates
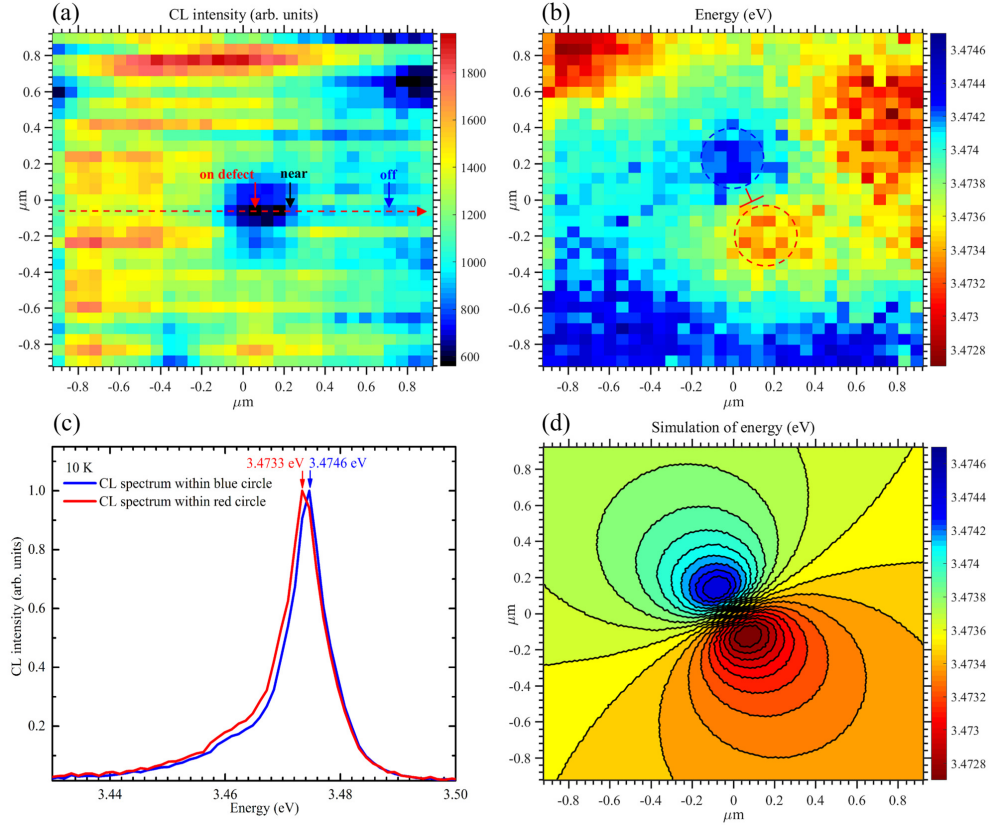
Figure 3.2 – (a) CL intensity mapping at T=10 K obtained under the pulsed excitation mode of the microscope, the color bar indicates the CL intensity (arb. units) in linear scale. (b) Peak energy mapping of the emission in the same area corresponding to (a). The color bar indicates the peak energy (eV) in linear scale; the blue and red dashed circles indicate the dipole-like energy shift, in the middle of which appears a mark at the position of the dislocation. (c) Normalized CL spectra integrated over the corresponding circles (blue/red) as shown in (b). (d) Results of the simulation of the emission energy shift corresponding to (b), with the fitting parameter FWHM of interaction volume =220 ± 30 nm.

the presence of an edge or mixed type of dislocation, which induces local strain fields [93, 94].

In figure 3.2(d), a continuum elastic model reproduces the dipole-like energy shift with the ~1.3 meV difference and ~400 nm separation between the two poles, which are consistent with the experimental results. In detail, the edge component of a dislocation has a Burgers vector $b = \frac{1}{3}\langle11\bar{2}0\rangle$. The dipole-like energy shift ΔE_g is given by:

$$\Delta E_g = (a_1 + b_1)\,\varepsilon_{zz} + (a_2 + b_2)\left(\varepsilon_{xx} + \varepsilon_{yy}\right), \tag{3.1}$$

$$\varepsilon_{xx} = \frac{b}{4\pi}y\frac{(3c_{11} + c_{12})\,x^2 + (c_{11} - c_{12})\,y^2}{c_{11}\left(x^2 + y^2\right)^2}, \tag{3.2}$$

$$\varepsilon_{yy} = \frac{b}{4\pi} y \frac{-(c_{11} + 3c_{12}) x^2 + (c_{11} - c_{12}) y^2}{c_{11} (x^2 + y^2)^2}, \tag{3.3}$$

where $a_{i=1,2}$ and $b_{i=1,2}$ are hydrostatic deformation potentials, $c_{ij} = 11, 12$ are the elastic constants of GaN, x and y indicate the location based on the Cartesian coordinate ($x \| \langle 11\bar{2}0 \rangle$, $y \| \langle 1\bar{1}00 \rangle$, $z \| \langle 0001 \rangle$), and $\varepsilon_i = xx, yy, zz$ are strain tensors, in which $\varepsilon_{zz} = 0$, considering the Burgers vector is parallel to the xy plane. All the above values are taken from Ref. [94]. Considering the interaction volume and the diffusion of injected carriers, ΔE_g is convoluted with a two-dimensional (2D) (xy plane) Gaussian distribution with a FWHM≈ 220 nm, which is consistent with the simulated interaction volume and determines both the energy shift and the separation distance of the dipole. Therefore, our simulation reveals that the optical properties around this particular dislocation are dominated by the edge component, with $\langle \bar{1}100 \rangle$ orientation, as the red mark of dislocation in figure 3.2(b) shows. In Ref. [94], the distance between the two poles was found to be $\sim 5\ \mu$m, which is one order of magnitude more than what we observe here (~ 400 nm). The reason behind this discrepancy is the following: the strain fields around a dislocation present a divergence exactly at the center of the dislocation. As a result, the distance between the observed maximum and minimum in energy only comes from the limited spatial resolution. Thanks to the much higher spatial resolution offered by CL compared to micro-PL, the two peaks appear closer in our experiments, which confirms the relevance of our approach.

The above analysis is useful to determine the type of dislocation and its influence on the local bandgap; however, we do not observe any significant impact of this dipole on the carrier diffusion. Indeed, the CL intensity around the dislocation in figure 3.2(a) does not exhibit any favored direction. This could be explained by the small energy shifts induced by the dislocation (± 0.7 meV), which is less than the thermal energy at T=10 K and as such does not play a significant role on the exciton dynamics.

3.2.4 Time-resolved cathodoluminescence at single dislocation

TR-CL is then employed to probe the exciton recombination dynamics around the dislocation. The effective lifetime τ_{eff} is measured along the red dashed arrow plotted in figure 3.2(a). Figure 3.3(a) shows a streak image recorded all along the red dashed arrow in figure 3.2(a) and demonstrates that the decay time is not energy dependent in our sample. Figure 3.3(b) presents the decay curves probed at different distances from the dislocation, as denoted by the solid arrows (on, near, and off the dislocation) in figure 3.2(a), and reveals two main features when moving closer to the dislocation: (1) The CL intensity $I_{CL}(t = 0)$ at early delay time is lower and (2) the effective lifetime τ_{eff} is shorter. In Figs. 3.3 (c) and 3.3 (d), more details are given by the one-dimensional (1D) mappings of $I_{CL}(t = 0)$ and τ_{eff}, extracted from a mono-exponential fit. $I_{CL}(t = 0)$ drops by 40% at the dislocation compared to the surroundings, and τ_{eff} reduces from 125 ps to 90 ps.

To explain both the spatially dependent effective lifetime τ_{eff} and the CL intensity at early delay time $I_{CL}(t = 0)$, we propose a model based on a 2D (xy plane) diffusion equation which considers a region around the dislocation, defined by an effective radius R_{eff}, where the
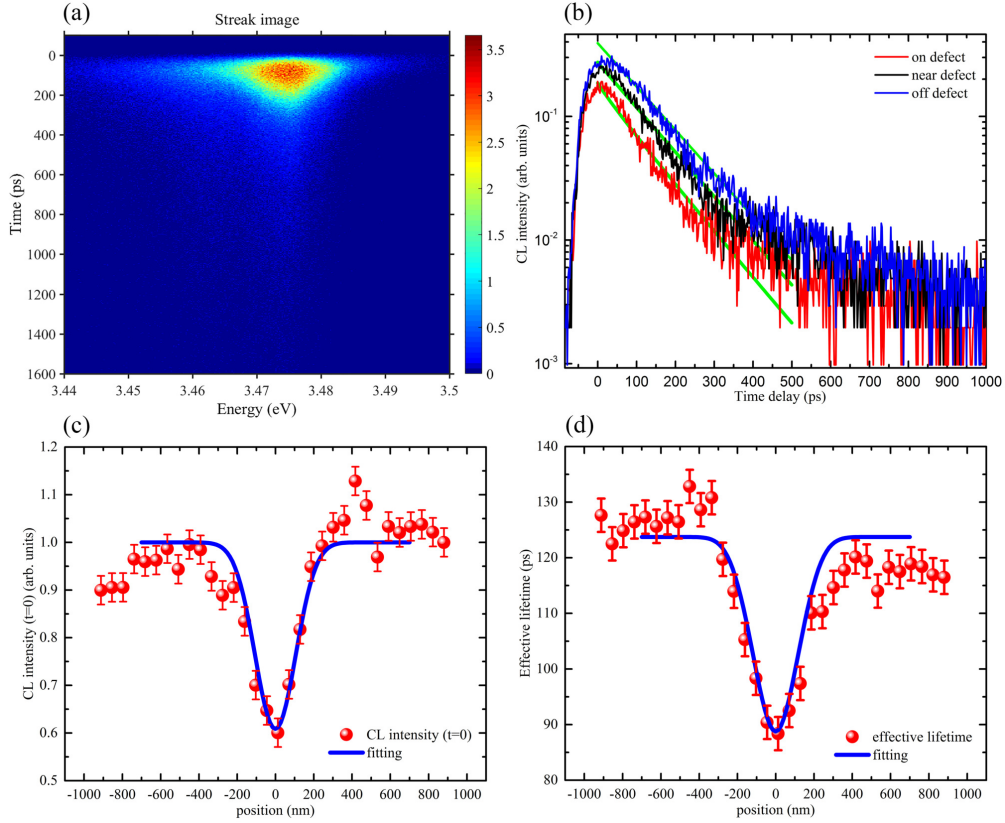
Figure 3.3 – (a) Integrated streak image of the 1D mapping along the line illustrated by the red dashed arrow in Fig. 3.2(a). The color bar indicates the CL intensity (arb. units) in linear scale. (b) Decay curves measured at different distances from the dislocation, as indicated by the solid arrow lines in Fig. 3.2(a) (on, near, and off the dislocation), and the fitting curves (green lines) corresponding to each decay curve. (c-d) 1D mappings of normalized $I_{CL}(r_0, t = 0)$ and $\tau_{eff}(r_0)$, and the best fits (blue lines) with the following parameters: diffusion coefficient $D = 4.5 \pm 0.2$ nm^2/ps, effective lifetime far from the dislocation $\tau_{eff,\infty} = 125 \pm 3$ ps, effective radius of the dislocation $R_{eff} \approx 95$ nm, FWHM of interaction volume = 220 ± 4 nm.

recombination is treated as entirely non-radiative and instantaneous [95]. This assumption is based on the fact that, when the electron beam is located at the dislocation, a drop of intensity appears at early delays, which indicates that the non-radiative processes at the dislocation are faster than our temporal resolution (~20 ps). For simplicity, we set the dislocation at the origin of the simulation area. When an exciton is outside the R_{eff} of the dislocation, it can diffuse and recombine either radiatively or non-radiatively, and the density as a function of location and time can be described as below:

$$\frac{d}{dt}n(r - r_0, t) = D\nabla^2 n(r - r_0, t) - \frac{n(r - r_0, t)}{\tau_{eff,\infty}}, \quad \text{if } r > R_{eff}, \tag{3.4}$$

where $n(r - r_0, t)$ is the exciton density at location r and at time t diffusing from r_0 (the position of the electron beam), D is the diffusion coefficient, and $\tau_{eff,\infty}$ is an effective lifetime far from the dislocation. On the other hand, when the excitons diffuse into the effective area

of dislocation, which is regarded as a *dead zone* [85], the exciton density is forced to vanish

$$n(r - r_0, t) = 0, \quad \text{if } r < R_{eff}. \tag{3.5}$$

The initial exciton density distribution is supposed to follow a Gaussian distribution $\mathcal{N}\left(r_0, \sigma^2\right)$, namely, $n(r - r_0, t = 0) = n_0 \mathcal{N}\left(r_0, \sigma^2\right)$, where n_0 is the initial exciton density and σ is its standard deviation. Since the FWHM has been estimated to be ~220 nm as mentioned before, the remaining fitting parameters to derive $n(r - r_0, t)$ are: R_{eff}, D, and $\tau_{eff,\infty}$, where $\tau_{eff,\infty}$ corresponds to the effective lifetime far from the dislocation: we set $\tau_{eff,\infty} = 125$ ps as observed experimentally. As a result, the CL intensity of excitons can be described as $I_{CL}(r - r_0, t) \propto n(r - r_0, t)/\tau_r$, and $\tau_{eff}(r_0)$ can be modeled by fitting $n(r - r_0, t)$, supposing a constant radiative lifetime τ_r. Here, it is important to notice that the two remaining parameters D and R_{eff} are independent and can be tuned almost independently during the fitting procedure. Indeed, the ratio between the effective radius R_{eff} and the FWHM of the interaction volume mostly defines the drop observed in the CL intensity at early delays $I_{CL}(t = 0)$, since we consider that the dislocation instantaneously acts on the carrier inside the effective dislocation area. On the other hand, the diffusion coefficient D mainly governs the dynamical behavior and hence acts on the effective lifetime $\tau_{eff}(r_0)$ around the dislocation. Such an independence between the two fitting parameters allows us to extract them confidently and provides robustness to our fitting procedure.

As shown in Figs. 3.3(c) and 3.3(d), the good agreement between our experimental results and the fits (blue lines) allows us to clearly identify the effective radius of dislocation $R_{eff} = 95 \pm 3$ nm, the diffusion coefficient $D = 4.5 \pm 0.2$ nm^2/ps, and the effective lifetime $\tau_{eff,\infty} = 125 \pm 3$ ps. Thus, the diffusion length of D$^\circ$X$_A$ $\left(L_{Diff} = \sqrt{D\tau_{eff,\infty}}\right)$ can be estimated to be ~24 nm, which indicates that D$^\circ$X$_A$ are able to diffuse over a short distance by hopping between donor levels [70, 96]. Note that the CL intensity at initial delay is defined as $I_{CL}(r_0, t = 0) \propto n_0 \mathcal{N}/\tau_r$. Considering that no diffusion happens at this moment, the decrease of $I_{CL}(r_0, t = 0)$ near the dislocation can be due to either the increase of τ_r or the reduction of n_0. However, the convoluted ~1.3 meV local potential fluctuation of dislocation unlikely changes the wave function overlap of excitons, which justifies why we consider τ_r to be constant over the sample. Therefore, the decrease of $I_{CL}(r_0, t = 0)$ near the dislocation should be ascribed to the non-radiative an instantaneous depletion of excitons within R_{eff}. In particular, $R_{eff} = 95 \pm 3$ nm is close to the previously reported value (~50 nm) [89]. Even though it is admitted that the core of a pure edge dislocation is at the atomic scale [97], our results clearly demonstrate that its impact on non-radiative recombination occurs up to the nanoscale, potentially because of the decoration of such dislocations by non-radiative defects or impurities [98, 99]. In addition, in figure 3.3(b), the decay curves at different positions are well reproduced by the fitting equation $I_{CL}(r_0, t) \propto n(r_0, t)/\tau_r$, which further support our model.

3.3 Impact of underlayer on point defects

3.3.1 Motivation

InGaN UL or InGaN/GaN SL are commonly used in high efficiency commercial blue LEDs grown by MOCVD. Several hypotheses were proposed to explain the role of such an UL for

improving the performance of LEDs, which includes: the reduction of structural defects, modulation of surface morphology or strain, and the enhancement of oscillator strength. However, recent systematic studies in our group demonstrated that the most likely role of the UL is to reduce the non-radiative defects and/or impurities, as proposed by Armstrong *et al.* [4, 75, 77]. Nitrogen vacancies V_N are one of candidates accounted for the NRCs, which can be created near the surface during high-temperature growth of GaN and segregate at the GaN surface. It is linked to a lower formation energy of V_N at the surface than that in the bulk GaN [100], which acts as non-radiative SD. When an InGaN UL is introduced into the structure of LEDs, the presence of indium atoms quenches the segregation process: V_N are incorporated in the bulk due to a decrease in their formation energy in InGaN [101, 102]. Since indium atoms play an essential role in trapping the defects, InAlN is expected to act as the same functionality. Compared to InGaN UL, InAlN UL possesses unique advantages, such as being able to circumvent strain-related issues by lattice-matched engineering, less optical loss for near ultraviolet (NUV) LEDs because of its large band gap.

3.3.2 Defect trapping mechanism by an underlayer

Here, we studied the defect trapping mechanism of an InAlN UL by varying its thickness. The samples grown by MOCVD share a common structure. A GaN buffer was first grown at 1000 °C on c-plane free-standing GaN substrate with low dislocation density about 10^6 cm^{-2}. An In$_{0.15}$Al$_{0.85}$N UL was subsequently grown at a temperature of 750 °C by varying the thickness (5 nm, 10 nm, 20 nm and 100 nm). Afterwards, a GaN spacer, an InGaN single SQW, and a GaN cap of 50 nm were grown, sequentially. The SQW was grown at 755 °C, with a ~12% indium composition and 2.7 nm width.
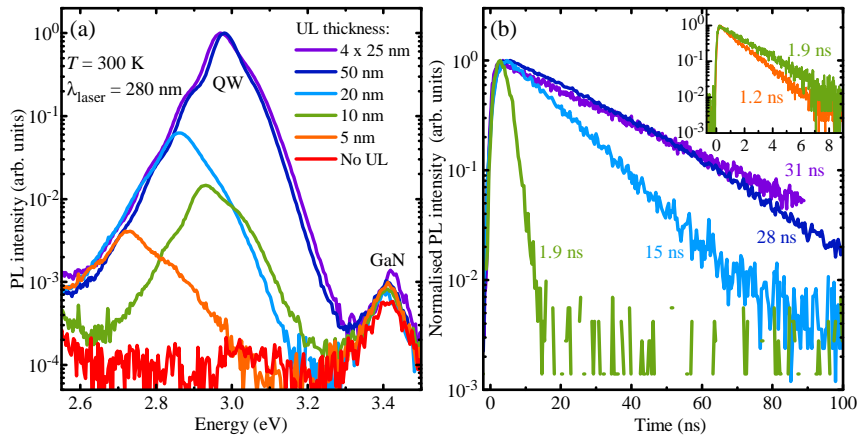
Figure 3.4 – (a) PL spectra recorded at 300 K for different InAlN UL thicknesses. (b) The corresponding normalized PL decay traces of the QW emission for a 100 ns time window and, inset, for a time window of 9 ns.

Figure 3.4 shows the PL spectra and corresponding PL decays of the sample series at 300 K under low excitation, with injected carrier density on the order of 10^{10} cm^{-2}. As the UL thickness increases, the QW PL intensity (I_{PL}) is enhanced significantly by more than two orders of magnitude, accompanied by longer PL decay, which evidences a reduction of the

non-radiative recombination rate. As a matter of fact, it indicates the thicker InAlN ULs reduce more effectively the defect density in the SQW. Figure 3.5 shows the UL thickness dependent decay time of QW emission extracted from a single exponential decay fit. The lifetime rises from ~1 ns to ~20 ns as the UL thickness increases from 5 nm to 50 nm, and then keeps constant around 30 ns when further increasing the UL thickness up to 100 nm. The evolution of the decay time suggests the defect-trapping effect by the UL saturates at the width around 20-50 nm for 15% indium content. As a comparison, in the sample series using GaN UL (grown by 770 °C) in the range of 0-220 nm and keeping other layers unchanged, the decay time of SQW (blue dots in figure 3.5) is below 1 ns and nearly independent of the thickness of the GaN UL, which suggests the inefficient trapping of SD by GaN itself.
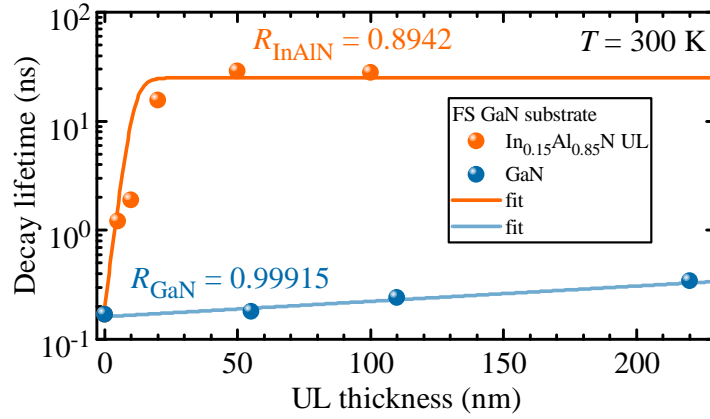

Figure 3.5 – Decay time of QW emission as a function of thickness of InAlN UL (orange dot) and of GaN UL (blue dot) as comparison. The corresponding fits (solid lines) are based on defect trapping model.

To analyze the defect trapping mechanism by UL, we modeled the decay time as a function of the SD concentration in the InGaN/GaN QWs [103]. First, we assume that SDs segregate at the surface during growth, with a surface concentration given by $[SD] = \theta_0 R^M$, where θ_0 is the initial surface density after the GaN growth at high temperature, M is the number of monolayers (MLs) (defined as $M = d/e_{\mathrm{ML}}$ with e_{ML} the InGaN ML thickness), and R is the segregation coefficient [104]. Previous observations by Akasaka *et al.* [76] indicate that the incorporation of SDs in GaN is negligible, i.e., R is close to 1. In contrast, SDs are incorporated in InAlN layers, i.e., R decreases. Assuming that SDs are buried upon interaction with indium atoms, we can write $R = R_{\mathrm{GaN}} - xp$ with R_{GaN} being the segregation coefficient of SDs in GaN, x the indium composition of the InAlN layer, and p the interaction efficiency between indium atoms and SDs. Then, the decay lifetime of the QW can be expressed as $1/\tau_{\mathrm{eff}} = 1/\tau_0 + 1/\tau_{\mathrm{NR,SD}}$, with τ_0 being the QW lifetime when all SDs are trapped into the InAlN UL and $\tau_{\mathrm{NR,SD}}$ is the non-radiative lifetime resulting from the incorporation of SDs. The latter is given by $1/\tau_{\mathrm{NR,SD}} \propto [SD]_{\mathrm{QW}}$, with $[SD]_{\mathrm{QW}}$ being the concentration of SDs in the QW. Finally, the QW effective lifetime can be expressed as:

$$\tau_{\mathrm{eff}} = \tau_0 \frac{1}{1 + \tau_0 \alpha \left(R_{\mathrm{GaN}} - xp\right)^M}, \tag{3.6}$$

with α a constant, which depends on θ_0 and the e-h capture coefficient of the defect. The best

fit is obtained with an interaction efficiency of 0.7 (R = 0.8942), which indicates the strong interaction of SDs with indium atoms.

3.3.3   Influence of point defects on carrier dynamics

In the literature, the capture coefficients for impurities and complexes range between 10^{-6} and 10^{-8} cm^{3}s^{-1} [105, 106, 107, 108], corresponding to a defect density comprised between 10^{15} and 10^{17} cm^{-3}, which corresponds to 10^8 and 10^{10} cm^{-2} in 2D unit for a standard QW with ~3 nm of width. To characterize defect-induced features by CL, such a high defect density makes it difficult to probe the carrier dynamics around an individual defect or cluster of defects, due to averaging effect. In contrast, the use of an ultra-thin active layer with few monolayers enables reducing the 3D defect density and avoid the averaging of the CL signal occurring in the thick QW or bulk structure. To have a nanoscopic insight into point defects, we thus grew ~3 ML (~0.78 nm) thick InGaN active layer on a ×24 $In_{0.17}Al_{0.83}N$/GaN SL (labeled as sample-3A), which serves to trap effectively the non-radiative defects and keep a flat surface during the step flow growth. As a comparison, a second sample was grown with the same active layer but without SL (sample-3B), which results in high defect density in the active layer. Both samples were grown on free-standing GaN substrate to reduce the density of dislocations. A GaN/$Al_{0.05}Ga_{0.95}N$ capping layer of 10/5 nm thickness is grown on top of the sample to prevent any the influence from surface states. The detailed structure of the two samples are shown in figure 3.6.
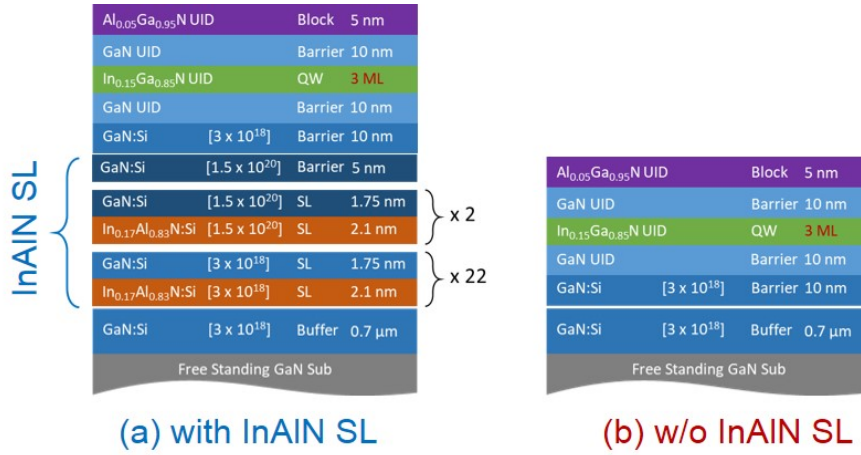
Figure 3.6 – (a) and (b) shows the structure of the two sample with and without InAlN SL, labeled as sample-3A and sample-3B, respectively.

To study the carrier localization and recombination dynamics in the QW, we first performed temperature dependent macro-PL and TR-PL measurements under low excitation, as shown in figure 3.7. Both samples show quite similar S-shape behaviors of the peak energy evolution versus temperature (see figure 3.7 and 3.8(a)): carriers gradually gain kinetic energy and relax down to the potential minima around 70 K and then start to delocalize. At 170 K, the blue shift of the energy saturates and a red shift starts induced by the thermal expansion of lattice constants, which indicates the mobility edge of carriers. These features evidence the

Figure 3.7 – (a) and (b) temperature dependent QW PL spectra for the samples with and without InAlN SL, respectively. (c) and (d) corresponding PL decay traces as a function of temperature for the same two samples.

similar degree of carrier localization between the two samples. Nevertheless, the two samples present a striking difference in the I_{PL} quench at e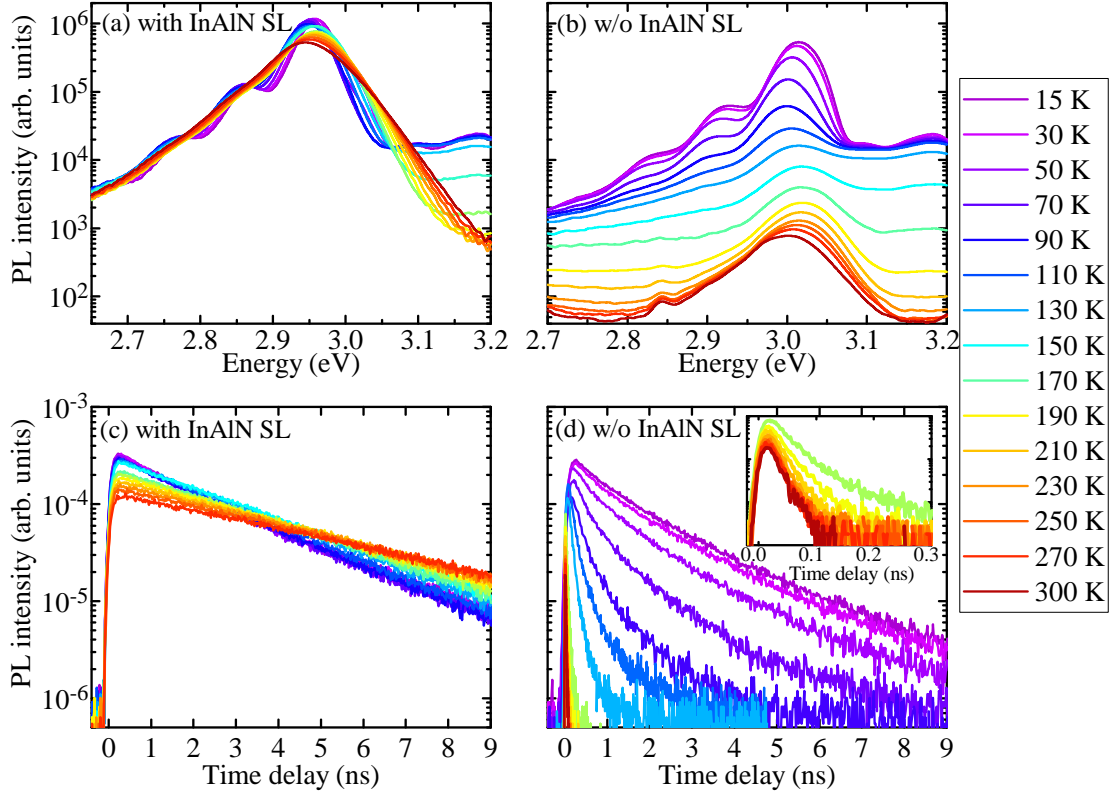levated temperature (see figure 3.8(b)), which indicates a significant difference in defect concentration. However, the difference in I_{PL} at 15 K is less pronounced, which can be well understood by the suppression of defect recombination channels by carrier localization. In agreement with the PL spectrum evolution, the decay time of QW in sample-3A is constant at 2 ns below 70 K. As temperature increases, it rises linearly up to 5 ns. Such behavior indicates that the carrier dynamics is dominated by radiative recombination, which stems from the thermal spreading of carriers near the Γ minimum in k-space. Conversely, within 70 K the decay time of sample-3B already drops from 1.5 ns to 0.5 ns during the carrier relaxation, and then reduces dramatically to 20 ps at 300 K, which evidences a defect-dominated carrier recombination. It also suggests that, in contrast to the common picture, the carrier localization at low temperature cannot fully terminate the non-radiative channels in defective samples. One possible reason is that the high defect density may form amount of *dead zone*, analogous to what we observed with dislocation, where carriers annihilates immediately. The other potential reason is that the tunneling probability from localization centers to defects can be significantly enhanced at high defect density [109, 110]. We then performed 1-kV CL to obtain additional nanoscopic information about the defect-related carrier recombinations.
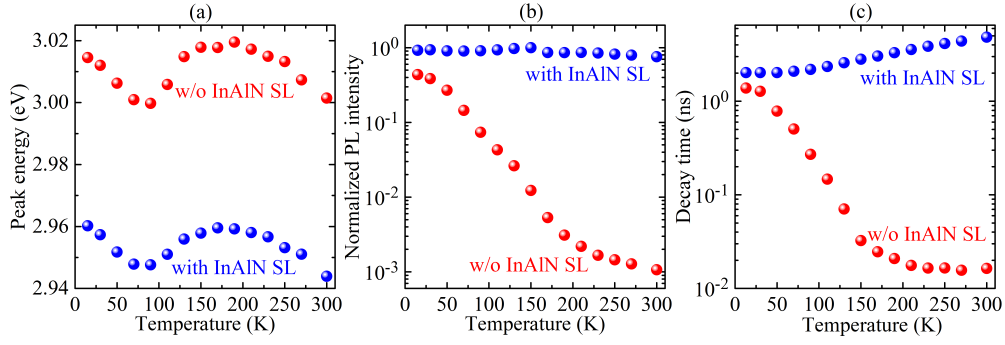
Figure 3.8 – Data extracted from figure 3.7, (a) and (b) are the temperature dependent peak energy and PL intensity of the QW emission in the samples with and without InAlN UL (c) Corresponding QW PL decay time as a function of temperature.

To characterize the surface morphology, we performed AFM on the top AlGaN cladding layer as shown in figure 3.9, which clearly exhibits periodic step edges indicating the identical step-flow growth mode in both samples. In addition, the height of each step measured by AFM
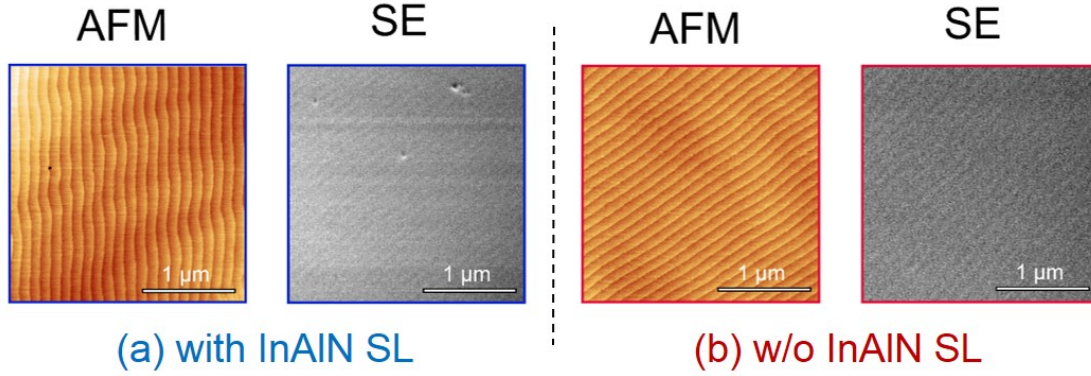
Figure 3.9 – Characterization of the surface morphology of the sample with (a) and without (b) InAlN SL by AFM and SEM (probed in different areas with respect to AFM).

is equal to 2 MLs, and the terrace width is about 150 nm. Moreover, the dislocation-induced V-pits are nearly absent in the two samples, thanks to the use of free-standing GaN substrates. Note that the formation of V-pits is mainly triggered by two factors [111]: (1) a masking effect of indium atoms: due to the strained field, indium atoms are trapped and segregate around the core of dislocations forming a small mask, which hinders Ga atoms from migrating on the {0001} plane; (2) growth kinetics of the GaN layer: at a temperature as low as ~ 800 °C, commonly used for the deposition of InGaN layers, the growth rate of the {10$\bar{1}$1} plane is reduced in comparison with the {0001} plane, which promotes the formation of V-pits. We then employed 1-kV SEM-CL to characterize the nanoscopic optical properties of our samples. The SEM image reveals the same features as AFM, which evidences the nanometer resolution of SE signal. In particular, the relative bright stripes suggest the location of step edges, which can be related to the "edge effect" of SE.

Figure 3.10 presents the spatial fluctuations of normalized CL intensity I_{CL} (normalized to the

maximum at each temperature) integrating full QW emission spectra from 10 to 170 K (same area as that shown in the SEM images of figure 3.9). At 10 K, though both samples exhibit I_{CL}
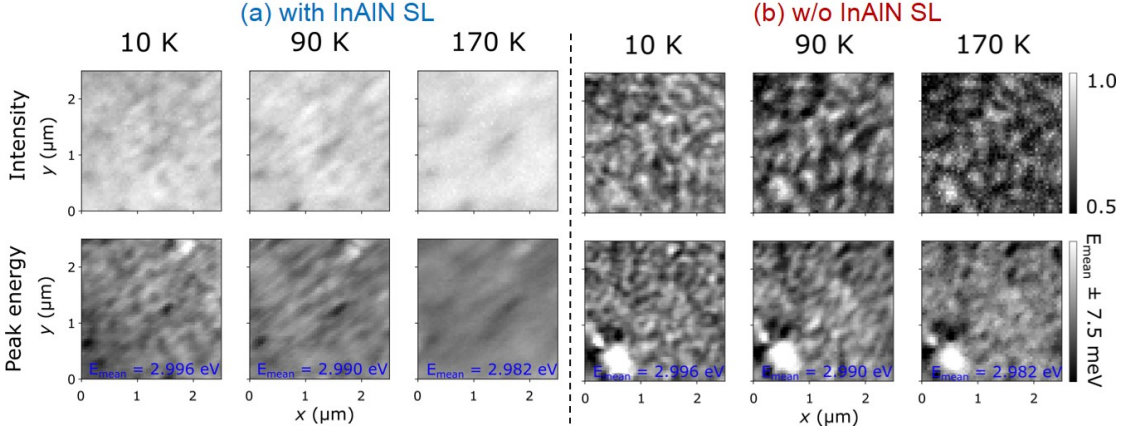

Figure 3.10 – Temperature dependent mappings of the QW CL intensity (normalized to the maximum at each temperature) and corresponding peak energy for samples with (a) and without (b) InAlN SL.

variations, sample-3B exhibits apparently larger I_{CL} fluctuation and higher density of dark spots than that in sample-3A. We tentatively ascribe this difference to the different density of defects or defect clusters between the two samples, as explained in the following. When temperature increases up to 170 K, the I_{CL} exhibits a gradual smoothing of the variations in sample-3A, with dark regions. This smoothing can be related to the increase in the diffusion length of carriers and insignificant defect recombination, as evidenced by the longer decay times deduced at elevated temperatures from TR-PL. In another word, the CL signal is averaged in the area determined by the carrier diffusion. The longer diffusion length in sample-3A is likely due to the significant reduction in defect density by the use of an InAlN UL. On the contrary, the I_{CL} mapping in sample-3B is more inhomogeneous and the dark areas expand and coalesce with each other notably. It can be understood in two ways: (1) as carriers are generated in the defective region, the high defect density prohibits carrier diffusion owing to the fast non-radiative recombination around 20 ps (see figure 3.8), which results in dark spots; (2) when exciting the sample in the defect-free region, the diffusion of carriers is determined by the interplay between carrier localization and the average distance between the high density defects. More precisely, the frozen carriers in the defect-free region are less sensitive to the defects, which gives a bright I_{CL}. As temperature increases, the diffusion length increases until reaching the mean distance between defects, the CL signal originates from the averaging area determined by the diffusion and becomes darker due to larger probability of carrier trapped by defects. On the other hand, the energy mapping at 10 K in both samples shows fluctuations as well. It may be induced by the micrometer-scale indium clustering or interface roughening. As temperature increases, the spatial energy variation becomes more homogeneous for both samples, which can be due to the increase in carrier diffusion and carrier delocalization. The larger smoothing of energy fluctuations in sample-3A further evidences the larger diffusion length. In addition, the observed fluctuations in I_{CL} are unlikely to be caused by spatial variations in the injection efficiency of carriers for two reasons: (1) The defects outside the QW are mainly segregated at the surface of AlGaN cladding layer, where a high density of SDs also exists induced by dangling bonds at the surface. The spatial variation of injection is

homogenized by the surface defects in both samples. (2) there is also spatial homogenization of the carrier injection in depth due to the use of thick GaN barriers.

3.4 Conclusions

In conclusion, using our picosecond TR-CL, we studied the exciton dynamics at 10 K around a single dislocation in bulk epitaxial GaN grown on a free-standing GaN substrate at $T = 0$ K. Edge dislocations are identified by observing and simulating the ~1.3 meV dipole-like energy shift, due to local strain fields induced by such type of dislocation. We determined the effective radius of dislocations to R_{eff} ~95 nm and the diffusion length to L_{diff} ~ 24 nm for $D°X_A$ by fitting the 1D mappings of the CL intensity at early delay time $I_{CL}(r_0, t = 0)$ and the effective lifetime $\tau_{eff}(r_0)$ around this dislocation, through a 2D exciton diffusion model. Therefore, our results pioneer an innovative way to quantitatively study the influence of dislocation on the efficiency of optoelectronic devices.

We studied the defect trapping mechanism by introducing an InAlN UL. The increase of the UL thickness up to 20 nm reduces significantly the non-radiative recombination in the QW, which is due to the burying of defects in the UL. We proposed that indium atoms play an essential role in capturing preexisting V_N at the GaN surface. We further investigated the nanoscopic optical properties of thin QWs with different defect densities modulated by UL. The significant suppression of the point defect density by UL leads to the radiative-dominated carrier recombinations, as evidenced by the increase of the decay time in 10 to 300 K. By using 1-kV CL measurements, we visualized defect-related variations of the I_{CL} at the nanometer scale and the change of carrier diffusion under different defect densities.

4 Carrier-density-dependent recombination dynamics in InGaN/GaN quantum wells

4.1 Introductions

This chapter reexamines both theoretically and experimentally the ABC model to take into account the presence of excitons, residual doping, and phase-space filling. Possible sources of radiative and non-radiative recombination are discussed in detail, as well as the influence of excitons, on blue LED recombination dynamics. Relying on TR-PL spectroscopy of InGaN/GaN m-plane MQWs, we developed a comprehensive model to extract all radiative and non-radiative recombination rates. The model also allows us to estimate the number of excitons in a operating LED. The major results of this study are summarized as follows: establish a comprehensive model to describe the recombination dynamics taking into account the presence of excitons, residual doping inside the quantum wells, and phase-space filling; reveal the asymmetry between electron and hole capture times by defect levels at 300 K; explain the interplay between excitonic population and the residual doping; estimate the amount of excitons in a working LED, which represent up to 63% of excited carriers at room temperature.

This work demonstrates the importance of precise determination of physical parameters to accurately describe efficiency droop, and provides critical information about the limits of the widely-used ABC model. Hence, these results pave the way to the development of a more precise estimation of the mechanism behind efficiency droop in high power LEDs.

4.2   Research background

c-plane InGaN/GaN QWs are the prevailing active layers in III-nitride LEDs, which have already achieved white LEDs with high luminous efficiency ($\sim$150 lm/W) and long lifetime ($\sim$10,000 h) [112, 113]. However, because of the large built-in polarization field ($\sim$MV/cm) along the growth direction, the well thickness of c-plane QWs is typically limited to 2–3 nm to maintain a sufficient radiative recombination rate [114]. Note that at high current injection, such a narrow well thickness results in a high carrier density, which increases the efficiency droop [42]. Thanks to the absence of any built-in polarization field, wider well thicknesses can be used with nonpolar m-plane InGaN/GaN QWs, which therefore possess a great potential for LED applications [115], such as reducing the influence of the efficiency droop [116]. In addition, because of their in-plane asymmetry, m-plane InGaN/GaN QWs are strong candidates for the realization of polarized light sources with an improved efficiency and promising properties for liquid-crystal displays [117]. In addition to their great potential for optoelectronic devices, m-plane InGaN/GaN QWs are a suitable platform to elucidate the complex mechanisms linked to carrier-density-dependent recombinations because of the absence of QCSE [118, 119, 120, 121, 122, 123, 124].

Since Auger recombination is often assumed to be the main reason for the efficiency droop, much effort has been devoted to the study of the Auger recombination process based on the so-called ABC model [43]. Nevertheless, the main difficulty lies in identifying unambiguously the nonradiative coefficient A and the bimolecular coefficient B, both being prerequisites to a proper determination of the Auger coefficient C. Due to the presence of unintentional n-type doping in InGaN/GaN QWs, both the experimentally deduced SRH recombination coefficient and the theoretical one reveal a saturation behavior upon increasing carrier density [125, 126, 127, 128]. In addition, recent study also points out that, in the c-plane QW, SRH rate also depends on the overlap of e-h wavefunction and position of defect in the QW [129]. Therefore, contrary to what is often assumed, A coefficient depends on carrier density. Likewise, the B coefficient cannot be treated as a constant since, at high density, when the system gets degenerate, phase-space filling drastically reduces B [130]. Furthermore, considering the large binding energy of excitons in thin InGaN/GaN QWs (both polar and nonpolar ones), exciton recombination is expected to play an important role even at room temperature [131, 132].

In this chapter, we study the carrier-density-dependent recombination dynamics in m-plane InGaN/GaN multiple QWs at different temperatures by using TR-PL; This enables us to determine both the effective lifetime through the decay of the signal, and the radiative lifetime through the recording of the PL signal at initial time delays. By taking into account n-type doping, phase-space filling, and the equilibrium between excitons and e-h pairs, we evaluate the density-dependent A and B coefficients, and obtain an upper limit for the C coefficient in our sample. After a detailed description of the model accounting for carrier-density-dependent recombination dynamics, the experimental results are critically analyzed within the framework of this model.

4.3 Theoretical framework of recombination dynamics

4.3.1 Modified *ABC* model

In order to model the carrier-density-dependent recombination dynamics, we start from the well-known *ABC* model

$$-\frac{dn}{dt} = An + Bn^2 + Cn^3, \tag{4.1}$$

where n is the carrier density in the active region, the A term takes into account SRH re-combinations, B is the bimolecular recombination coefficient which describes the radiative recombinations, and finally the C coefficient characterizes the dependence of the Auger recombinations as a function of carrier density. Though this model is widely used in the literature, it is only valid when the doping concentration n_0 and the injected carrier density n are low enough ($n_0 < 10^{16}$ cm^{-3} and $n < 10^{18}$ cm^{-3}). Indeed, at low injection ($n < 10^{16}$ cm^{-3}), residual doping could play an important role [127]. Similarly, above 10^{18} cm^{-3}, it has been shown that Fermi filling influences the carrier dynamics [133]. Since we investigate a sample with a relatively high n-type background density ($n_0 \approx 10^{18}$ cm^{-3}), the *ABC* model should be modified accordingly. In addition, the *ABC* model only describes the dynamics of e-h pair recombination. In our case, the exciton binding energy E_B is estimated to be larger than 26 meV due to quantum confinement [134]. As a consequence, even at room temperature ($k_B\mathrm{T} \approx$ 26 meV), the influence of excitons needs to be taken into account. In the following, we will describe our modified *ABC* model.

As discussed before, it has been proven that considering the A coefficient as a constant is invalid as soon as the injected carrier density gets close to that of the residual doping in InGaN/GaN QWs [128]. Since we focus on nonpolar m-plane QW in this chapter, the electric-field-dependent SRH process is not taken into account [129]. According to the SRH model with the presence of an n-type background doping, the lifetime of SRH recombinations $\tau_{nr,SRH}$ should be written as [125, 126, 128]

$$\tau_{nr,SRH} = \tau_{p0} + \tau_{n0}\frac{n_{e-h}}{n_{e-h} + n_0}, \tag{4.2}$$

where τ_{p0} (τ_{n0}) is the hole (electron) capture time by deep level defects (each one of them being occupied by one electron (hole)), n_{e-h} is the excess e-h plasma density (assuming n_{e-h} = n for the moment). The difference between τ_{p0} and τ_{n0} is mainly attributed to the different capture cross sections and velocities for electrons and holes.

Under high injection, the Auger recombination channel becomes the dominant nonradiative recombination mechanism and its lifetime $\tau_{nr,Auger}$ is defined as

$$\tau_{nr,Auger} = [C_{ehe}(n_0 + n_{e-h})^2 + C_{ehh}n_{e-h}(n_0 + n_{e-h})]^{-1}, \tag{4.3}$$

where C_{ehe} (C_{ehh}) is the Auger recombination coefficient, which denotes that the energy from e-h recombinations is transferred to a third particle: another electron (hole). It has been reported that the value of C_{ehe} and that of C_{ehh} are close to each other [135], we thus assume

here for simplicity that $C_{ehe} = C_{ehh} = C_{Auger}$. As a result, the total nonradiative lifetime of the e-h plasma, including SRH and Auger recombinations is expressed as follows:

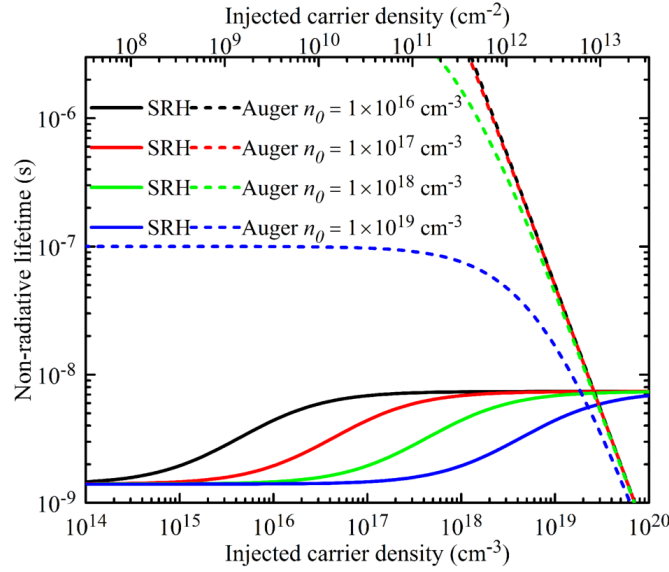$$\tau_{nr,e-h} = (\tau_{nr,SRH}^{-1} + \tau_{nr,Auger}^{-1})^{-1},\tag{4.4}$$

Figure 4.1 – Impact of different n-type background doping concentrations (n_0) on the lifetimes of SRH (solid curves) and Auger (dashed curves) recombination at 300 K, obtained with the following parameters: hole capture time of defects $\tau_{p0} = 1.4 \times 10^{-9}$ s, electron capture time of defects $\tau_{n0} = 6 \times 10^{-9}$ s, and Auger recombination coefficient $C_{Auger} = 1 \times 10^{-31}$ cm^{6}s^{-1}.

Figure 4.1 shows the impact of the n-type background density on the lifetimes of SRH and Auger recombinations at 300 K, with the parameters $\tau_{p0} = 1.4 \times 10^{-9}$ s, $\tau_{n0} = 6 \times 10^{-9}$ s, extracted from our experiment. The upper x axis denotes the 2D n_{e-h}. $C_{Auger} = 1 \times 10^{-31}$ cm^{6}s^{-1}, considering the ~5 nm QW thickness of our sample. As shown in figure 4.1, upon increasing n_{e-h}, $\tau_{nr,SRH}$ shows two plateaus at τ_{p0} for low densities and $\tau_{p0} + \tau_{n0}$ for high densities. The origin of such a behavior lies in: (1) the asymmetric electron and hole capture times and (2) the n_{e-h} dependence of the fraction of defect levels occupied by electrons [126]. At low injection, most defect levels are occupied by background electrons, the annihilation of these electrons on the defect levels only depends on the hole capture time τ_{p0}. At high injection, the fraction of defect levels occupied by electrons decreases, because the photocarrier density exceeds the background doping. Consequently, for these deep levels, $\tau_{nr,SRH}$ becomes dependent on both the electron and hole capture time $\tau_{p0} + \tau_{n0}$, which can be one order of magnitude larger than τ_{p0} in GaN-based QWs [128]. In addition, figure 4.1 demonstrates that Auger recombination only plays a role at very high injection $n > 1 \times 10^{19}$ cm^{-3} and would be slightly enhanced by the n-type background doping when $n_0 > 1 \times 10^{19}$ cm^{-3}.

Concerning the radiative lifetime of the e-h plasma $\tau_{r,e-h}$, instead of using the standard

equation:

$$1/[B(n_{e-h} + n_0)], \tag{4.5}$$

one should consider the phase-space filling effect, which leads to a drastic decrease in the B term when the plasma becomes degenerate [133]. As a consequence, it is necessary to derive $\tau_{r,e-h}$ from Fermi's golden rule. The density-dependent $\tau_{r,e-h}$ is therefore described as follows:

$$R_{sp} = \frac{n_{e-h}}{\tau_{r,e-h}}, \tag{4.6}$$

$$R_{sp} = \frac{1}{\tau_0} \int_{E_{QW}}^{\infty} g_{2D}(E) f_e(E) f_h(E) dE, \tag{4.7}$$

$$g_{2D} = \frac{\mu}{\pi \hbar^2} H(E - E_{QW}), \tag{4.8}$$

$$f_e = \left[\exp \left(\frac{(E - E_{QW}) \mu/m_e - E_{f,e}}{k_B T} \right) + 1 \right]^{-1}, \tag{4.9}$$

$$f_h = \left[\exp \left(\frac{(E - E_{QW}) \mu/m_h - E_{f,h}}{k_B T} \right) + 1 \right]^{-1}, \tag{4.10}$$

$$E_{f,e} = k_B T \ln \left[\exp \left(\frac{\pi \hbar^2 (n_0 + n_{e-h})}{m_e k_B T} \right) - 1 \right], \tag{4.11}$$

$$E_{f,h} = k_B T \ln \left[\exp \left(\frac{\pi \hbar^2 n_{e-h}}{m_h k_B T} \right) - 1 \right], \tag{4.12}$$

$$\mu = m_e m_h/(m_e + m_h), \tag{4.13}$$

where R_{sp} is the spontaneous recombination rate, $\tau_{r,e-h}$ is the radiative lifetime of the e-h plasma, $1/\tau_0$ is the rate constant which depends on the oscillator strength, g_{2D} is the 2D joint density of states, $H(E - E_{QW})$ is the Heaviside step function, E_{QW} is the optical band gap of the QWs, E is the emission energy, f_e (f_h) is the Fermi-Dirac distribution for electrons (holes), $E_{f,e}$ ($E_{f,h}$) is the quasi-Fermi level energy of electrons (holes), and μ is the in-plane

carrier reduced mass. $m_e = 0.2\, m_0$ is the effective electron mass and $m_h = \sqrt{m_\parallel m_\perp}$ is the geometric mean value of the in-plane effective hole mass in the first valence band. By using $\mathbf{k} \cdot \mathbf{p}$ simulations [136], the effective mass along the c axis is estimated to be $m_\parallel = 1.83\, m_0$ and the one in the perpendicular direction to be $m_\perp = 0.185\, m_0$. Note that here only the transition between the conduction band and the first valence band is considered. This is a valid approximation because the energy splitting between the first and second valence bands in m-plane InGaN/GaN QWs (35 meV in the present sample as deduced from $\mathbf{k} \cdot \mathbf{p}$ simulations) [136] is larger than the thermal activation energy at 300 K. In addition, $\hbar$ is the reduced Planck constant, and m_0 is the electron rest mass.

Figure 4.2 evidences the influence of the n-type background doping on the radiative lifetime of the e-h plasma at 300 K.
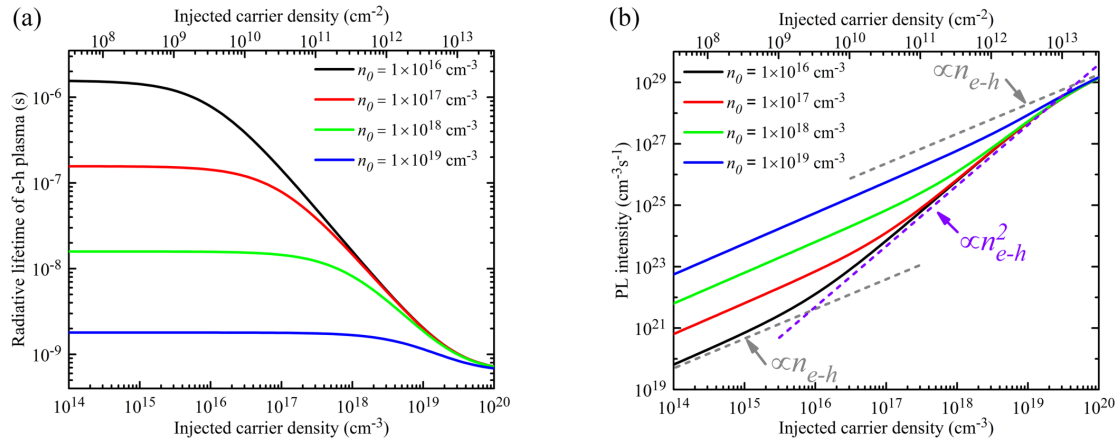

Figure 4.2 – Injected carrier-density-dependent $\tau_{r,e-h}$ for different n-type background concentrations (n_0 at 300 K, with the average recombination time $\tau_0 = 6.2 \times 10^{-6}$ s. (b) Corresponding injected carrier-density-dependent PL intensity given by $I_{pl} \propto n_{e-h}/\tau_{r,e-h}$

It is clear that $\tau_{r,e-h}$ can be significantly reduced when increasing n_0 at low injection. In addition, because of the effect of phase-space filling, $\tau_{r,e-h}$ saturates at high n values around 1×10^{20} cm^{-3}. Figure 4.2(b) presents the corresponding PL intensity as a function of n_{e-h} at 300 K, defined as $I_{pl} \propto R_{sp}$. It clearly shows that the quadratic increase in I_{pl} as a function of n_{e-h}, expected from the bimolecular recombination mechanism is only valid when n_{e-h} lies in between n_0 and the degenerate density. These results justify the use of Fermi's golden rule to properly describe the e-h plasma radiative recombination over a wide range of carrier densities.

4.3.2 Mott transition by first order correlated Saha's equation

As stated previously, considering the large exciton binding energy in m-plane InGaN/GaN QWs, it is necessary to evaluate the impact of excitons on the recombination dynamics at 300 K. In our TR-PL experiment, the equilibrium between excitons and e-h plasma can be established by interparticle collisions within a few femtoseconds timescale, which is much faster than the time scale for carrier recombination [137]. Therefore, it can be assumed that

equilibrium is established initially just after the excitation pulse. The ratio between exciton and the e-h plasma densities in a QW is usually determined by the standard Saha's equation derived from the Boltzmann distribution [138]. This equation does not consider any Coulomb screening. Here we use instead the first order corrected Saha's equation (in the 2D case), which accounts for the Mott transition [139]:

$$\frac{(n_{e-h} + n_0)\, n_{e-h}}{n_x} = \frac{\mu k_B T}{2\pi \hbar^2} \frac{1}{\exp\left(E_B / k_B T\right) - 1}, \tag{4.14}$$

$$n = n_x + n_{e-h}, \tag{4.15}$$

where n_x is the 2D density of excitons. Due to Coulomb screening and phase-space filling effects, one should consider the reduction of E_B as n increases. In the model of abrupt Mott transition[139], it results in a strong temperature dependent Mott density, which is not observed in III-nitride QW [130]. We thus assume a smooth Mott transition [130, 140]. To describe such a behavior in a simple way, an equation analogous to the Debye screening model is used here [141]:

$$E_B(n) = E_{B0} \exp\left(-\frac{n}{n_{Mott}}\right), \tag{4.16}$$

where E_{B0} is the exciton binding energy at low carrier density [134] and n_{Mott} is the 2D critical Mott density, which is about 10^{12} cm^{-2} for GaN-based QWs [130, 140]. Since we investigate InGaN QWs with a relatively low In content (<10%), we assume that the critical Mott density remains unchanged.

Figure 4.3(a) shows the modeling of the excitonic fraction phase diagrams at different injected carrier densities and temperatures in the absence of any residual doping using $n_{Mott} = 1 \times 10^{12}$ cm^{-2}. $E_{B0} = 42$ meV is further determined through a self-consistent Schrödinger-Poisson calculation, as described in Ref. [142]. This value is in agreement with that given in Ref. [143]. All the above-mentioned 2D densities are then transformed into three-dimensional ones, considering a quantum well thickness of ~5 nm. Figure 4.3(a) reveals that, when $n < n_{Mott} = 3 \times 10^{18}$ cm^{-3} and $T < 50$ K, the injected carrier population is mainly composed of excitons. At 300 K, however, the maximum exciton fraction occurs for a total carrier density around 10^{18} cm^{-3} and then quickly vanishes. Figure 4.3(c) presents the phase diagram of the exciton fraction under n-type background doping with $n_0 = 1 \times 10^{18}$ cm^{-3}, keeping all other parameters identical to those of figure 4.3(a). This reveals that n-type background doping facilitates the formation of excitons. This naturally stems from the principle of Saha's equation: the equilibrium corresponds to the minimum of total free energy for the e-h plasma and the exciton gas.

Since the ratio between excitons and e-h plasma populations is determined by the first order corrected Saha's equation, we can further model the phase diagram of the fraction of exciton
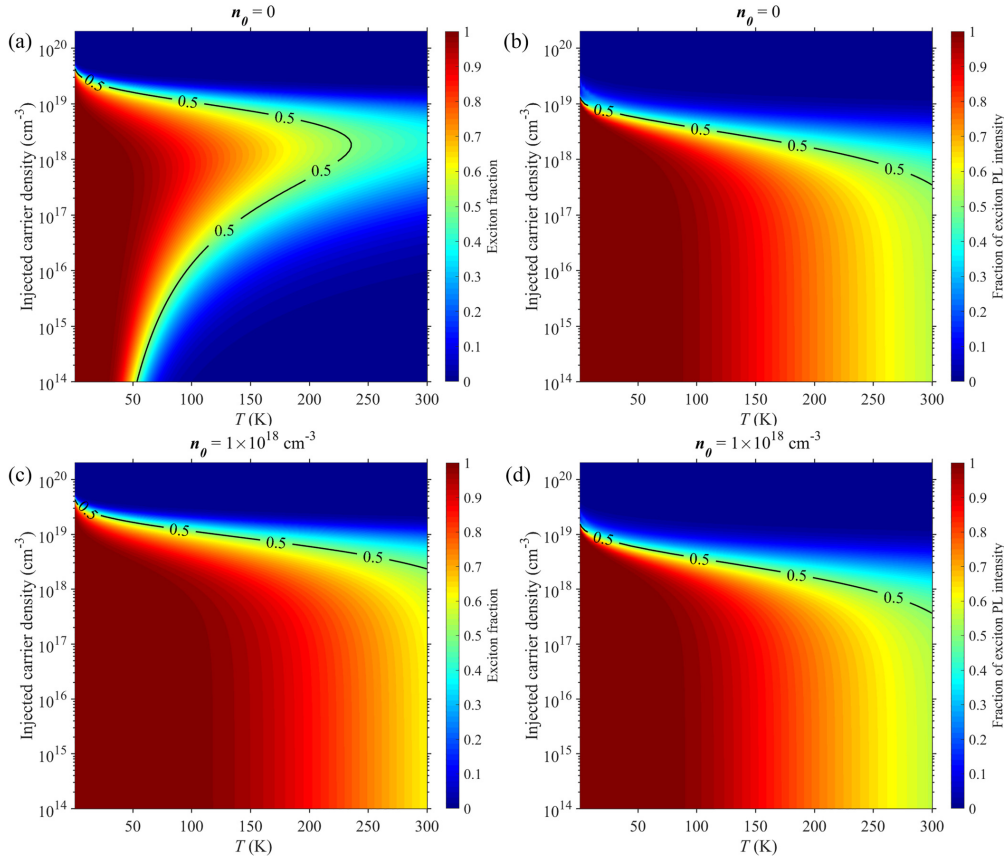
Figure 4.3 – (a) Computed phase diagrams of the exciton fraction vs total photoexcited carrier density in the QWs without n-type backgroung doping, with the parameters: $n_{Mott} = 1 \times 10^{12}$ cm^{-2}, $E_{B0} = 42$ meV. (b) Computed phase diagrams of the fraction of exciton PL intensity vs total PL intensity without n-type background doping, with the parameters: $n_{Mott} = 1 \times 10^{12}$ cm^{-2}. For simplicity, $\tau_{r,x}$ has been chosen to vary linearly between 1.7×10^{-8} at 300 K and 5.0×10^{-10} s at 4 K, and $\tau_{r,e-h}$ linearly decreases from 5×10^{-6} s from 300 to 4 K. Those values are extracted from the following experiments (see section 4.5). (c) and (d) Corresponding phase diagrams with an n-type background doping $n_0 = 1 \times 10^{18}$ cm^{-3}.

PL intensity by the following set of equations:

$$R_x(n, T) = \frac{n_x / \tau_{r,x}(T)}{n / \tau_r(T)}, \tag{4.17}$$

$$\tau_r(T) = \left(\frac{n_x}{n} \tau_{r,x}^{-1}(T) + \frac{n_{e-h}}{n} \tau_{r,e-h}^{-1}(T) \right)^{-1}, \tag{4.18}$$

where $R_x(n, T)$ is the fraction of the exciton PL intensity for a given set of n and T values. $\tau_r(T)$, $\tau_{r,x}(T)$ and $\tau_{r,e-h}(T)$ are the effective radiative lifetime, the exciton radiative lifetime, and the e-h plasma radiative lifetime at T. Figures 3(b) and 3(d) present the phase diagrams

of the fraction of exciton PL intensity without any n-type background doping and with $n_0 = 1 \times 10^{18}$ cm^{-3}. First of all, it reveals that n-type background doping does not change the phase diagrams of $R_x(n, T)$. Secondly, below the Mott density, the fraction of exciton PL intensity is independent of the injected density and only depends on temperature. To elucidate the physics in a simple way, considering the low injection regime ($n \ll n_{\text{Mott}}$), $R_x(n, T)$ can be derived through Saha's Eqs. (4.14) and (4.5), as detailed below:

$$R_x(T) = \frac{1/\tau_{r,x}(T)}{B \cdot r(T) + 1/\tau_{r,x}(T)}, \tag{4.19}$$

and

$$r(T) = \frac{\mu k_B T}{2\pi\hbar^2} \frac{1}{\exp\left(E_{B0}/k_B T\right) - 1}. \tag{4.20}$$

Thus, it is clear that $R_x(T)$ is independent of n_0 and n.
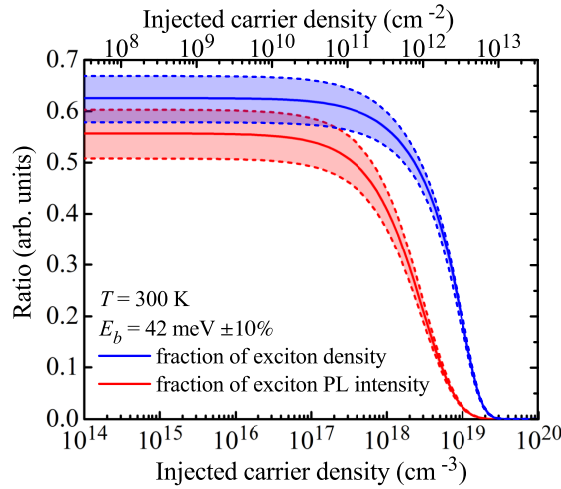
Figure 4.4 – Influence of the exciton binding energy with $E_{B0} = 42 \pm 4$ meV on the estimated fractions of excitonic density (blue lines) and PL intensity (red lines) at 300 K.

In addition, to evaluate the impact of exciton binding energy on the exciton fraction around $E_{B0} = 42$ meV at low injection, we change its value by $\pm 10\%$. As shown in figure 4.4, it corresponds to a $63 \pm 6\%$ fraction of exciton density and a $56 \pm 10\%$ fraction of exciton PL intensity at low carrier density at 300 K.

In the end, to properly model our experiments, and according to the usual definition of PL intensity decay:

$$I_{pl}(t) \propto \frac{n}{\tau_r} \exp\left(-\frac{t}{\tau_{eff}}\right), \tag{4.21}$$

the initial PL intensity $I_{pl}(t=0)$ can be described as

$$I_{pl}(t=0) \propto \frac{n}{\tau_r},$$

(4.22)

where a proportionality constant links experiment and modeling, which is only given by the TR-PL system and does not change with either temperature or sample design. The effective lifetime τ_{eff} is expressed as

$$\tau_{eff} = \left(\tau_{nr}^{-1} + \tau_r^{-1}\right)^{-1}.$$

(4.23)

The nonradiative lifetime τ_{nr} and the radiative lifetime τ_r contain both the contributions from excitons and the e-h plasma, which are detailed below:

$$\tau_{nr} = \left(\frac{n_x}{n}\tau_{nr,x}^{-1} + \frac{n_{e-h}}{n}\tau_{nr,e-h}^{-1}\right)^{-1},$$

(4.24)

$$\tau_r = \left(\frac{n_x}{n}\tau_{r,x}^{-1} + \frac{n_{e-h}}{n}\tau_{r,e-h}^{-1}\right)^{-1},$$

(4.25)

where $\tau_{r,x}$ and $\tau_{nr,x}$ are the radiative and nonradiative lifetimes of excitons.

As a consequence, apart from the injected carrier density, the initial PL intensity only depends on the radiative lifetime, whereas the effective lifetime provides the relative contribution from the radiative and nonradiative recombinations. As our experiments are performed under identical conditions, a direct comparison of the PL intensities is meaningful.

4.4 Sample structure and experimental detail

The sample is grown by MOCVD (provided by Dr. A. Dussaigne, Leti Grenoble): based on the growth condition, the active layer consists of 5 × InGaN/GaN (~5 nm/12 nm) QWs with ~10% indium composition, capped by a 50-nm-thick top GaN barrier. The m-plane free-standing GaN substrate is overgrown by a 1-μm-thick GaN buffer layer prior to the growth of the QW region. In particular, to optimize the homogeneous distribution of indium in the QWs, the growth conditions of the QWs are set to T = 750 °C and the V/III ratio = 10 000. The n-type background n_0 in the MQWs is estimated in the order of 10^{18} cm^{-3} from a similar series of samples by electrochemical capacitance-voltage (ECV) measurements, as shown in figure 4.5.

TR-PL experiments in this study are detailed in chapter 2. In particular, a pulse picker is employed to reduce frequency of pulse f by 22 times to avoid any heating of the sample, which provides a temporal resolution better than 100 ps in long time windows of detection. To estimate the power density impinging on our sample, supposing the laser beam has a Gaussian distribution of fluence, we first determine the FWHM = 0.8 mm as the diameter of the beam before the UV objective using the knife-edge method [144]. The radius of the focused laser beam on the sample is then estimated to be 5 ± 1 μm. The beam transmission through the whole excitation path is about 52%. The reflectance of the GaN surface, taking into account the refractive index of 2.6 at 280 nm [145], is estimated to be around 20%. Since
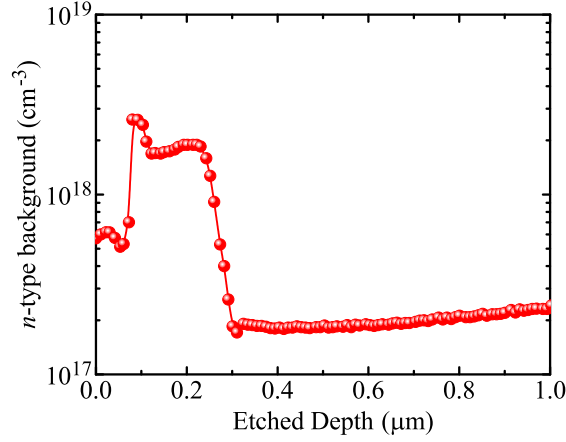
Figure 4.5 – *n*-type background concentration by ECV measurements in the similar series of sample.

the absorption in the sample mainly happens in the first GaN capping layer and active layers, in our high quality sample (as will be evidenced in the following section), it is reasonable to assume that about half the carriers generated in the first capping layer are trapped by the QWs (the other half is assumed to diffuse to the surface), and all the carriers created in the active region are captured by the QWs. Therefore, the final fraction of carriers captured by the QWs is estimated to be ~60%, considering a GaN absorption coefficient equal to 1.5×10^5 cm^{-1} at 280 nm [146]. As a result, a 1 mW laser power at the output of the tripler finally generates a carrier density of about 6×10^{19} cm^{-3} in the five QWs with ±40% relative uncertainty, which arises from the accuracy of the estimation of the laser spot size and the absorption by the QWs and the barriers.

4.5 High-density excitonic effects

The first set of experiments relies on high power nonresonant TR-PL performed at low temperature. In order to characterize the phase-space filling occurring under high excitation conditions, we probe the PL spectrum at early delay at 4 K. Figure 4.6(a) presents the power-dependent PL spectra measured at initial delay (between 0 and 20 ps). The laser fluence on the sample ranges from 0.0075 to 22 μJ cm^{-2}. The main outcome is that, above 0.95 μJ cm^{-2}, the spectra become significantly broader as a result of phase-space filling. As shown in Fig. 4(b), below 0.95 μJ cm^{-2}, the FWHM of the PL spectra and the peak energy remain nearly constant around 38 meV and 3.15 eV, respectively, whereas, above 0.95 μJ cm^{-2}, the FWHM gets wider by 20 meV and the peak energy shifts toward higher energy by 6 meV. The significant spectral broadening and the slight blueshift in the emission energy are the signatures of phase-space filling and provide further evidence of the fact that the initially injected carrier density is close to the Mott density, which is typically observed to occur between 5×10^{11} and 2×10^{12} cm^{-2} for GaN based QWs [130, 140]. Since the temperature has a significant impact on the recombination dynamics and on the equilibrium between the exciton gas and the e-h plasma, we performed TR-PL experiments at 4 and 300 K under identical conditions.
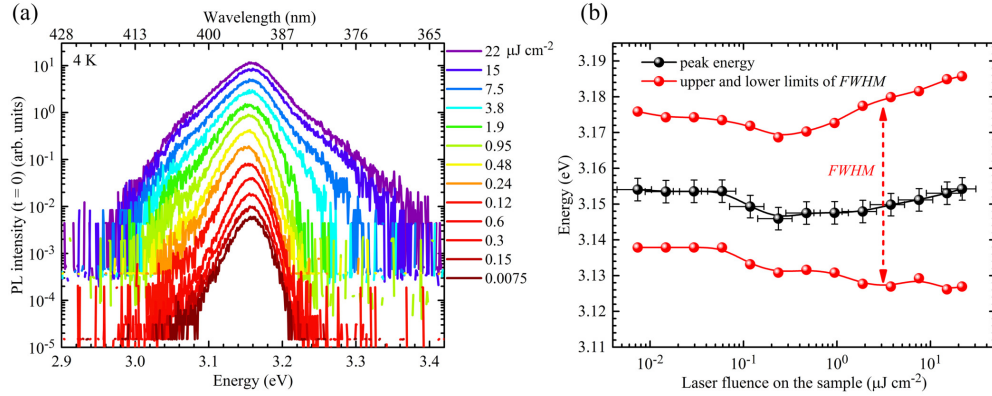
Figure 4.6 – (a) Power-dependent PL spectra at early time delay (between 0 and 20 ps) at 4 K for various laser fluences on the sample ranging from 0.0075 to 22 μJ cm^{-2}. (b) Corresponding power-dependent peak energies (black dots) and the upper and lower limits of the FWHM (red dots) of the PL spectra measured at initial delay.

Figures 4.7(a) and 4.7(b) show the power-dependent decay curves integrated over the whole energy range of the QW emission spectra at 4 and 300 K. Through the whole excitation range, τ_{eff} values are much longer at 300 K than they are at 4 K. We can account for this observation on the basis of Eq. (4.23): the increase in the radiative lifetime τ_r, caused by the spreading of the thermal distribution of the carriers, is more prominent than the decrease in the nonradiative lifetime τ_{nr} [147].
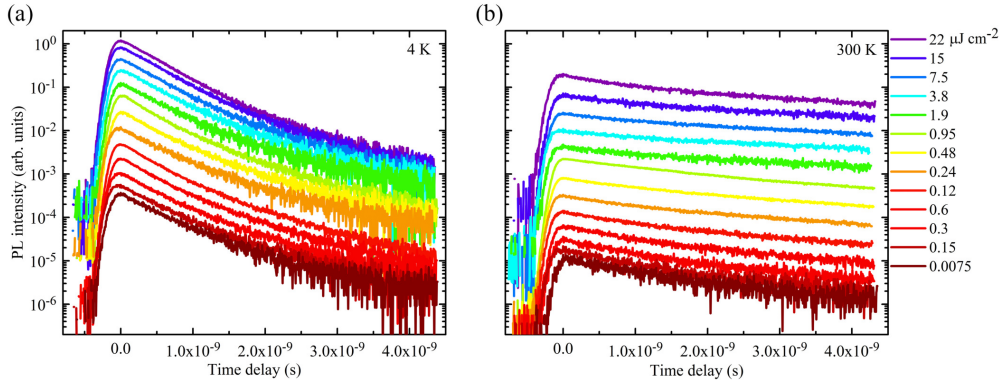
Figure 4.7 – (a) and (b) Power-dependent decay curves integrated over the whole energy range of QW emission spectra measured at 4 and 300 K under conditions otherwise identical for laser fluences on the sample ranging from 0.0075 to 22 μJcm^{-2}

To get more insight into the recombination dynamics of carriers at early delays, we extract both the initial PL intensity $I_{pl}(t = 0)$ and the effective carrier lifetime τ_{eff} by single exponential decay fitting at early delay (within 1 ns). As mentioned before, $I_{pl}(t = 0)$ only depends on the radiative lifetime and the injected carrier density [147]. The high temporal resolution of our TR-PL setup fulfils the requirements allowing us to probe the initial PL signal.

In figure 4.8(a) we plot the injected carrier density n-dependent $I_{pl}(t = 0)$ at both 4 K (black dots) and 300 K (red dots). $I_{pl}(t = 0, 4\,\text{K})$ shows a linear dependence on n as well as an invariant

measured effective lifetime, $\tau_{eff,\,4\,\text{K}} \approx 500$ ps, as shown in figure 4.8(b). On the contrary, at 300 K, the slope of $I_{pl}(t=0,300$ K$)$ changes from 1 to 2 above $n = 10^{18}$ cm^{-3}. Meanwhile, the effective lifetime $\tau_{eff,300K}$ first increases from 1.3 to 3.0 ns when n $< 10^{18}$ cm^{-3}, and then decreases down to 1.6 ns at n $= 1 \times 10^{19}$ cm^{-3}.

To obtain a better understanding about these phenomena, we further extract the radiative lifetime using

$$\frac{I_{pl}(t=0,300\text{ K})}{I_{pl}(t=0,4\text{ K})} = \eta_{inj} \frac{\tau_{r,4\text{ K}}}{\tau_{r,300\text{ K}}}, \tag{4.26}$$

where $\tau_{r,\,300\,\text{K}}$ and $\tau_{r,\,4\,\text{K}}$ denote the radiative lifetime at a temperature of 300 and 4 K, respectively, η_{inj} is the ratio of the injected carrier density at 300 and 4 K, and $\tau_{r,\,4\,\text{K}} = \tau_{eff,\,300\,\text{K}} \approx 500$ ps assuming that nonradiative recombinations are negligible at 4 K. Since we use a nonresonant excitation scheme, the injection efficiency η_{inj} may vary from 4 to 300 K because of the thermal activation of nonradiative defects in the barriers and recombinations occurring at the sample surface. According to Eq. 4.26, this may lead to a change in the estimation of the radiative lifetime at 300 K. Here the upper limit of η_{inj} is set to 100%. The lower limit of η_{inj} is obtained by fulfilling the lifetime inequality $\tau_{r,\,300\,\text{K}} \geq \tau_{eff,\,300\,\text{K}}$. As a consequence, to satisfy the last inequality, the lower limit is bounded to 80%. As shown in figure 4.8(b), $\tau_{r,\,300\,\text{K}}$ is evolving within the green shaded region, which stays approximately constant around 1.7×10^{-8} s when $n < 10^{18}$ cm^{-3}, after which $\tau_{r,\,300\,\text{K}}$ reduces to about 2.5×10^{-9} s at about $n = 1 \times 10^{19}$ cm^{-3}. In order to estimate the contributions of residual doping, bimolecular recombination, and the presence of excitons, we subsequently model the recombination dynamics according to the formalism described in the previous section 4.3.

The experimental $I_{pl}(t=0,4$ K$)$ data can be fitted by only considering pure exciton recombination. To analyze the 300 K data, we start from $I_{pl}(t=0,300$ K$)$ and $\tau_{r,\,300\,\text{K}}$. The parameters that we have used are: $n_0 = 1 \times 10^{18}$ cm^{-3} as obtained from the capacitance-voltage measurements, $n_{\text{Mott}} = 1 \times 10^{12}$ cm^{-2} as measured in our previous reports [20, 31] and $\tau_{r,\,x,\,4\,\text{K}} = \tau_{eff,\,4\,\text{K}} \approx 500$ ps. Finally, the unknown rate constant of the e-h plasma $1/\tau_0$ is 2×10^5 s^{-1}, as obtained from the best fit of the radiative lifetime under high injection. Similarly, the excitonic radiative lifetime is determined through the fitting of the experimental radiative lifetime under low injection $\tau_{r,\,x,\,300\,\text{K}} = 1.7 \times 10^{-8}$ s. The above-mentioned parameters are summarized in Table 4.1.

Table 4.1 – Fitting parameters for the measured radiative recombination properties measured at 300 K based on Saha's equation.

$n_0 \left(\text{cm}^{-3}\right)$	$n_{\text{Mott}} \left(\text{cm}^{-2}\right)$	$\tau_0(\text{s})$	$\tau_{x,r}(\text{s})$
1×10^{18}	1×10^{12}	5×10^{-6}	1.7×10^{-8}

As shown in figure 4.8(a), the fitting curve of $I_{pl}(t=0,300$ K$)$ (red solid curve) reproduces quite well the change in slope occurring above 10^{18} cm^{-3}. We then decompose, through Saha's equation, the total $I_{pl}(t=0,300$ K$)$ into e-h plasma PL intensity $I_{pl,\,e-h}(t=0,300$ K$)$ and exciton PL intensity $I_{pl,\,x}(t=0,300$ K$)$. This allows us to show that $I_{pl}(t=0,300$ K$)$ is
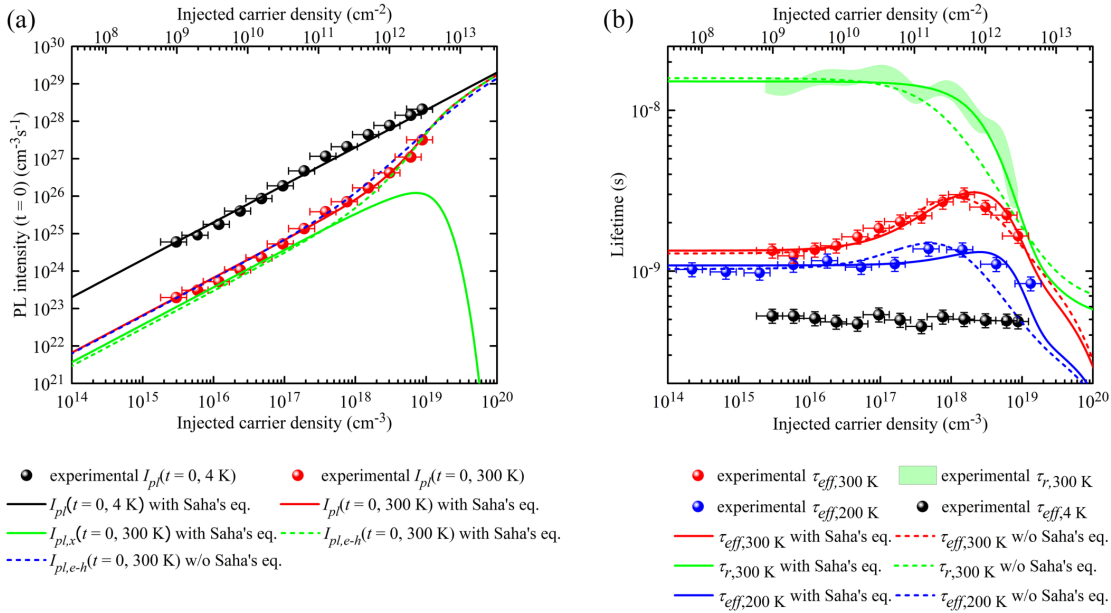
Figure 4.8 – (a) Injected carrier-density-dependent PL intensity at the initial delay $I_{pl}(t = 0)$ measured at 4 K (black dots) and 300 K (red dots) extracted from the decay curves shown in figure 4.7 and related fits deduced from modeling with and without Saha's equation. The black solid line is the fit obtained by assuming that pure excitonic recombination is at play at 4 K. Modeling with Saha's equation at 300 K, the red solid curve is the total $I_{pl}(t = 0)$ containing the recombination of excitons and that of the e-h plasma, the green dashed curve is the e-h plasma $I_{pl,e-h}(t = 0)$, while the green solid curve is the exciton one $I_{pl,x}(t = 0)$. The blue dashed curve is the result of modeling without Saha's equation at 300 K, namely, a pure e-h plasma system. (b) Corresponding injected carrier-density-dependent effective lifetimes $\tau_{eff,\,4\,K}$ (black dots) at 4 K, $\tau_{eff,\,200\,K}$ (blue dots) at 200 K, $\tau_{eff,\,300\,K}$ (red dots) at 300 K, and the estimated radiative lifetime at 300 K $\tau_{r,\,300\,K}$ (green dashed region). The solid curves are the related fits deduced from modeling using Saha's equation. The dashed curves are the related fits based on the modeling without Saha's equation. The error bar of the injected carrier density is $\approx 40\%$. It is mainly coming from the estimation of the excitation spot diameter and the uncertainty on the injection efficiency η_{inj} at room temperature. Concerning the precision on the effective lifetime, we estimate the error to be less than 10%, due to the nonzero time windows (1 ns) to estimate the effective lifetime at early delays.

dominated by $I_{pl,\,e-h}(t = 0, 300\ \text{K})$ [green dashed curve in figure 4.8(a)]. The change in slope of $I_{pl,\,e-h}(t = 0, 300\ \text{K})$ from 1 to 2 is mainly due to the injected carrier density exceeding the n-type background doping one. To be more specific, the recombination rate at low injection is given by $I_{pl}(n) = Bn_0 n_{e-h}$ and the slope is equal to one. When the injected carrier density exceeds n_0, it transforms into $I_{pl}(n) = Bn_{e-h}^2$ and the slope becomes equal to 2. Fermi's golden rule further predits that the slope of $I_{pl,\,e-h}(t = 0, 300\ \text{K})$ will return to 1 for n above $1 \times 10^{20}\ \text{cm}^{-3}$, because of phase-space filling.

On the other hand, the exciton dynamics around the Mott transition region is featured by $I_{pl,\,x}(t = 0, 300\ \text{K})$ (green solid line) in figure 4.8(a). The maximum of $I_{pl,\,x}(t = 0, 300\ \text{K})$ occurs around $10^{19}\ \text{cm}^{-3}$, which corresponds to the lower boundary of the Mott transition region. When $n > 1 \times 10^{19}\ \text{cm}^{-3}$, the drastic collapse in $I_{pl,\,x}(t = 0, 300\ \text{K})$ is due to exciton dissociation occurring through Coulomb screening.

Table 4.2 – Fitting parameters related to nonradiative recombinations at 300 K based on Saha's equation.

$\tau_{\mathrm{nr},\,x}\,(\mathrm{s})$	$\tau_{n0}\,(\mathrm{s})$	$\tau_{p0}\,(\mathrm{s})$	$C_{Auger}\,(\mathrm{cm^6 s^{-1}})$
6×10^{-9}	6×10^{-9}	6.5×10^{-10}	1×10^{-31}

In figure 4.8(b), the good correspondence between the fit (green solid curve) and experimental data (green shaded region) of $\tau_{r,\,300\,\mathrm{K}}$, further attests the validity of our model. In brief, the nearly constant $\tau_{r,\,300\,\mathrm{K}} \approx 1.7 \times 10^{-8}$ when $n < 1 \times 10^{18}$ cm^{-3} results from the rather large n-type background doping and the presence of an exciton population. Between $n = 1 \times 10^{18}$ and 1×10^{19} cm^{-3}, the rapid decrease in $\tau_{r,\,300\,\mathrm{K}}$ is due to the enhancement of bimolecular recombination.

The previous determination of $\tau_{r,\,300K}$ allows us to analyze further and unambiguously the effective nonradiative carrier lifetime $\tau_{nr,\,300\,\mathrm{K}}$. As mentioned before, the increasing $\tau_{eff,\,300\,\mathrm{K}}$ at low injection is interpreted as the saturation of SRH recombinations. As for the exciton nonradiative lifetime $\tau_{\mathrm{nr},\,x}$, we assume that it mainly depends on the trapping of the carrier with the longer capture time: in our case, $\tau_{\mathrm{nr},\,x} = \tau_{n0}$ [148]. As a results, we are able to determine the hole capture time, $\tau_{p0} = 6.5 \times 10^{-10}$ s, via the fit of $\tau_{eff,\,300\,\mathrm{K}}$ at low injection. The electron capture time $\tau_{n0} = 6 \times 10^{-9}$ s is further determined by fitting $\tau_{eff,\,300\,\mathrm{K}}$ at higher injection. The only parameter left is the Auger coefficient C_{Auger} which is used to match the decreasing trend of $\tau_{eff,\,300\,\mathrm{K}}$ when the carrier density is above $n > 1 \times 10^{18}$ cm^{-3}. It turns out that C_{Auger} should be less than 1×10^{-31} cm^{6}s^{-1}, since the decrease in $\tau_{eff,\,300\,\mathrm{K}}$ is mainly dominated by $\tau_{r,\,300\,\mathrm{K}}$ in our sample. This result is consistent with theoretical works that state that decreasing the weight of disorder reduces Auger recombination [135]. The above fitting parameters, allowing us to reproduce the observed variations in τ_{eff}, 300 K related to nonradiative recombinations, are summarized in Table 4.2. Finally, the curve given by the model for $\tau_{eff,\,300}$ K (red solid line) reproduces very satisfactorily the experiment, and demonstrates that the reduction in $\tau_{eff,\,300\,\mathrm{K}}$ between $n = 1 \times 10^{18}$ and 1×10^{19} cm^{-3} is dominated by radiative recombinations.

As a comparison, to illustrate the impact of excitons on the recombination dynamics at 300 K, we further model the change in lifetime assuming that all the injected carriers stay in the form of an e-h plasma, while keeping the same n_0, n_{Mott}, τ_{n0}, and C_{Auger} values used in the model with Saha's equation at 300 K, but with different $\tau_0 = 6.2 \times 10^{-6}$ s and $\tau_{p0} = 1.4 \times 10^{-9}$. As shown in figure 4.8(a), even though the pure e-h plasma contribution $I_{pl}(t = 0, 300\,\mathrm{K})$ (blue dashed line) reproduces accurately the experimental data below the Mott transition, it is slightly above the experimental data in the Mott transition region. Correspondingly, in figure 4.8(b), $\tau_{r,\,300\,\mathrm{K}}$ (green dashed line) derived from a pure e-h plasma model is shorter than the experimental one. Considering the fitting procedure and the analog radiative lifetime $\tau_{r,\,e-h,300\,\mathrm{K}} = 1/(Bn_0)$ at low injection, the B term (related to τ_0 in Fermi's golden rule) is determined by both the known n_0 value and the nearly constant radiative lifetime at low injection. Therefore, in the Mott transition region, the discrepancy in the fitting of $\tau_{r,\,e-h,\,300\,\mathrm{K}}$ results from an overestimated n_{e-h} value if the formation of excitons is neglected, even though the reduction in B by phase-space filling has been properly considered.

To observe more pronounced excitonic effects and confirm our conclusions, we further perform experiments at 200 K and fit the $\tau_{eff,\,200\,K}$ dependence using the two possible models as highlighted above. For the fit of a pure e-h plasma at 200 K, $\tau_0 = 2.3 \times 10^{-6}$ s, which is the only fitting parameter different from the one used at 300 K. For the fit with Saha's equation at 200 K, We take $\tau_0 = 2.6 \times 10^{-6}$ and $\tau_{r,\,x} = 1.6 \times 10^{-9}$ s. As shown in figure 4.8(b), the pure e-h plasma scenario (blue dashed curve) cannot fit $\tau_{eff,\,200\,K}$ in the Mott density region, which strongly indicates the overestimation of n_{e-h}. Conversely, the model with Saha's equation reproduces very well the smooth reduction in $\tau_{eff,\,200K}$ in the Mott transition region. At 200 K, $87 \pm 5\%$ of the injected carrier density is bound into excitons when $n < 1 \times 10^{18}$ cm^{-3}, and then gradually reduces to $\sim 30\%$ at $n = 1 \times 10^{19}$ cm^{-3}, due to coulomb screening. In addition, the weight of $I_{pl,\,x}(t = 0, 200\,K)$ is supposed to be $95 \pm 2\%$, compared to $56 \pm 10\%$ of that at 300 K. Therefore, exciton recombination is far more prominent at 200 K.
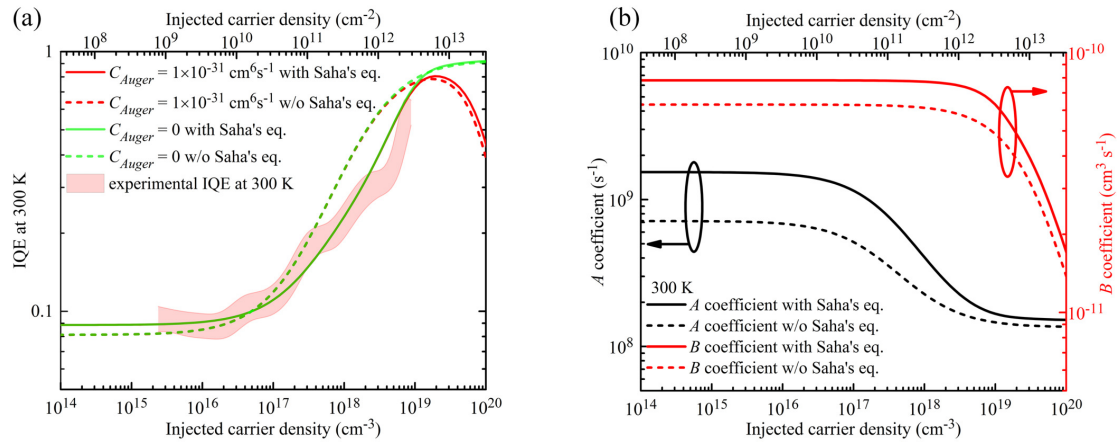

Figure 4.9 – (a) Injected carrier-density-dependent internal quantum efficiency derived from IQE= $\tau_{eff,\,300\,K}/\tau_{r,\,300\,K}$ (red shaded region). The red solid and red dashed curves are fits based on models with and without Saha's equation, the fitting parameters of which are the same as the fits shown in figure 4.8. The green solid curve and the green dashed curve are the fits based on models with and without Saha's equation, keeping the same fitting parameters as for the previous fits except for $C_{Auger} = 0$. (b) Injected carrier-density-dependent B coefficients (red curves) and A coefficients (black curves) extracted from the experimental data shown in figure 4.8. The solid (dashed) curves are fits based on the moel with and without Saha's equation, respectively.

As shown in figure 4.9(a), when using the above-mentioned model, we are able to derive the injected carrier-density-dependent internal quantum efficiency (red shaded region), defined as IQE = $\tau_{eff,\,300\,K}/\tau_{r,\,300\,K}$. The model with Saha's equation gives a better fit (red solid curve) compared to the one based on a pure e-h plasma (red dashed curve). Both models predict a similar decrease in IQE due to Auger recombination at high injection density, for $C_{Auger} = 1 \times 10^{-31}$ cm^{6}s^{-1}. As a comparison, setting $C_{Auger} = 0$ for both models, with and without Saha's equation (green solid and dashed curves) predict IQEs larger than 90% at high injection. The density-dependent A and B coefficients can be further derived by $A = 1/\tau_{nr,\,SRH,\,300\,K}$ and $B = 1/\left[(n_0 + n_{e-h})\tau_{r,\,e-h,\,300\,K}\right]$, as presented in figure 4.9(b). Note that getting A and B coefficients in a convincing way is a prerequisite to properly determine C_{Auger}. Therefore our experiments and the model including Saha's equation provide an effective way to analyze in better detail the Auger related efficiency droop at high injection in GaN-based heterostructures.

4.6 Conclusions

Based on high injection time-resolved photoluminescence experiments, we have studied the carrier-density-dependent recombination dynamics in m-plane InGaN/GaN QWs with large n-type background doping ($\sim 1 \times 10^{18}$ cm^{-3}). At low temperature, pure excitonic recombination is evidenced, even under high injection conditions, through a nearly invariant effective lifetime of about 500 ps. Thanks to the high temporal resolution of our setup, we are able to probe the recombination dynamics even at very early times after injection, which allows us to extract the carrier-density-dependent radiative lifetime at all temperatures. As a result, we could extract convincingly the injected carrier-density-dependent bimolecular recombination coefficient, taking into account n-type background doping, phase-space filling effects, equilibrium between excitons and the e-h plasma, and the Mott transition. Saha's equation reveals that the n-type background doping not only facilitates bimolecular recombination at low injection, but also promotes the formation of excitons. The validity of Saha's equation is further attested by its ability to reproduce the carrier-density-dependent effective lifetime at 200 K where stronger excitonic effects take place. Based on the SRH model, we could extract the electron and hole capture times by deep levels at 300 K. We have also demonstrated that the increasing effective lifetime with increasing carrier density at 300 K stems from asymmetric capture times between electrons and holes and the presence of n-type background doping. The SRH model also predicts that, in QWs with heavier n-type background doping, higher injection will be required to saturate the SRH recombination. Finally, because of the reasonable determination of density-dependent A and B coefficients in the Mott transition region, our method provides a way to evaluate the impact of Auger recombination.

5 Auger recombination in InGaN/GaN quantum wells

5.1 Introduction

As mentioned in section 1.3.1, efficiency droop occurs when the driving current density is raised above a few amperes per square centimeter [42, 149, 150]. Auger recombination is one of the widely accepted mechanisms for the efficiency droop in InGaN/GaN-based LEDs. This hypothesis has been strengthened by experimental results [43, 151], which demonstrates the hot electron emission from LEDs under the droop regime. The direct band-to-band Auger process in wide band gap semiconductors is expected to be weak, in the order of 10^{-34} cm^{6}s^{-1}, considering the strict conditions for conserving the momentum and energy between the initial and final states. In theory, indirect Auger processes are supposed to be the main reason for the droop, which can be elevated significantly through various carrier scatterings by alloy disorder, phonons, and defects [152, 153, 135]. On the other hand, the reduced dimensionality potentially results in relieving momentum conservation, since quantum confinement causes strong carrier localization in the real space, or expands the wavefunction in the reciprocal space. Up to date, experimental evidences about indirect Auger processes have been rarely reported yet, which are imperative to understand the carrier scattering mechanisms and the related effects on the quantum efficiency of LEDs.

In this chapter, we investigate the impact of carrier localization on the Auger recombination in InGaN/GaN QWs via high injection TR-PL at 4 K. Based on a modified time-derivative *ABC* model, we estimate accurately the Auger coefficient in the InGaN alloy system with different degree of disorder. Apart from alloy disorder, SRH-type point defects can also be scattering centers, which allows relaxing the momentum conservation and energy threshold for Auger recombination. Thanks to the tuning of defect densities in the InGaN/GaN QWs by AlInN UL as detailed in section 3.3.3, we studied the defect-assisted Auger process in the InGaN/GaN QW with different defect densities by high injection TR-PL at 300 K and the modeling.

5.2 Auger recombination intensified by carrier localization

5.2.1 Introduction

A precise measurement of the Auger coefficient is often plagued by uncertainties in determining the carrier density in the active region [154]. Here, using a TR-PL setup that allows achieving high fluence, combined with a formalism developed previously [130, 140], we accurately estimated the carrier density and therefore precisely determine the Auger coefficient in InGaN/GaN and GaN/AlGaN QWs. By comparing the PL dynamics recorded on two c-plane QW samples, we observe no signature of Auger loss on low Al content GaN/AlGaN QWs, in contrast to the InGaN/GaN QW sample. Then by considering two m-plane samples with different degrees of disorder, we demonstrate the predominant role played by potential disorder in the Auger recombination mechanism in m-plane InGaN/GaN QWs. More precisely, we point out that, despite the beneficial role of alloy fluctuations for alleviating the detrimental impact of non-radiative recombination by dislocations and defects at low injection [79, 155], the corresponding localization causes fast Auger recombination at higher carrier densities.

5.2.2 Samples Characterization

The investigated samples consist of a total of four QW samples grown by MOCVD on freestanding GaN substrates with low dislocation density (10^6 cm^{-2}): two m-plane InGaN/GaN MQWs (provided by Dr. A. Dussaigne, Leti Grenoble), one c-plane InGaN/GaN SQW and the other c-plane GaN/AlGaN SQW. The m-plane GaN substrate was overgrown by a 1 μm thick GaN buffer layer prior to the growth of the QWs. The two m-plane InGaN/GaN samples feature 5 QWs which are 5.0 $\pm$0.5 nm thick for m-QW1 and 4.5 $\pm$ 0.5 nm thick for m-QW2, separated by 12 nm thick GaN barrier, and capped by a 50 nm thick top GaN barrier. The In composition of the wells was estimated to be ~10% in the first sample and ~12% in the second one based on Schrödinger-Poisson simulations and energy dispersive x-ray (EDX) analysis. In order to increase the disorder in m-QW2, the growth temperature has been reduced by 60 °C and the V/III ratio has been lowered by a factor of eight compared to m-QW1 in order to maintain a similar In incorporation. As deduced from high-resolution TEM images (figure 5.1), the change in the growth conditions modifies the structural properties of the InGaN QWs: m-QW1 [figure 5.1(a)] exhibits sharp interfaces between the GaN barriers and the InGaN QWs. On the other hand, in the case of m-QW2 [figure 5.1(b)], the GaN/InGaN interface remains relatively sharp, but the InGaN/GaN interface is much more diffuse.

In addition to these two m-plane QWs, two c-plane SQW samples were also investigated: (i) a c-plane InGaN/GaN SQW which consists of a 2 nm thick $In_{0.09}Ga_{0.91}N$ QW embedded between two GaN barriers, for which the top and bottom barrier thicknesses are 50 and 200 nm, respectively; (ii) a c-plane GaN/AlGaN SQW which consists of a 3 nm thick GaN QW embedded between two $Al_{0.09}Ga_{0.91}N$ barriers, for which the top and bottom barrier thicknesses are 30 and 150 nm, respectively. The built-in electric field in the QW is estimated to be around 350 kV/cm in the case of c-plane GaN/AlGaN QW [156] and around 1.0 MV/cm in the c-plane InGaN/GaN QW [157].

First, to characterize the luminescence properties of the different samples, we perform low injection PL as a function of temperature (~100 nJ/cm^2 per pulse, λ = 280 nm, repetition rate
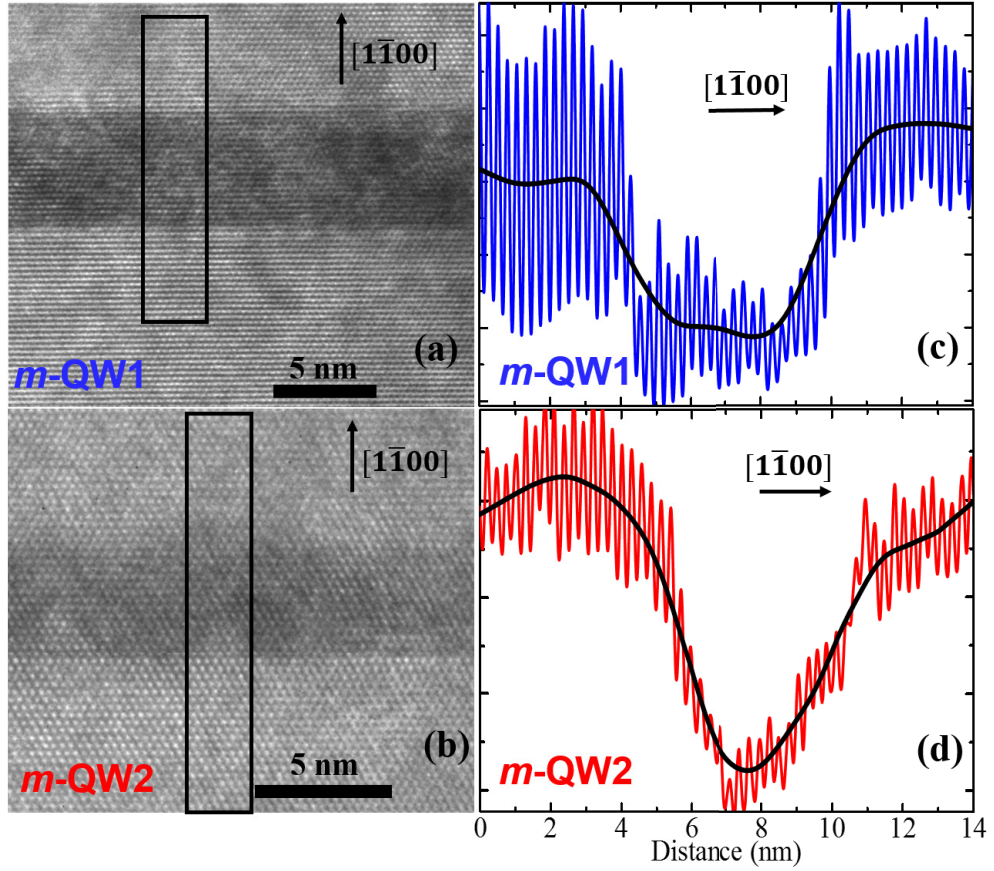
Figure 5.1 – high-resolution TEM images (performed by Dr. C. Bougerol, CNRS Grenoble) of the *m*-plane QWs, in (a) the *m*-QW1 sample and (b) the *m*-QW2 sample. Contrast line scans along the growth direction (c) in the m-QW1 sample, and (d) the *m*-QW2 sample.

80.7 MHz). The evolution of the QWs emission energy and that of the corresponding FWHM are summarized in figure 5.2 for for the four samples. For *c*-plane samples, the InGaN/GaN SQW exhibits a stronger S-shaped behavior [158] compared to its GaN/AlGaN counterpart. In addition, the broadening at low temperature is lower for the GaN/AlGaN SQW (8 meV) compared to the InGaN/GaN SQW (26 meV). It indicates that the *c*-plane InGaN/GaN SQW sample is characterized by a deeper fluctuation potential compared to the GaN/AlGaN ones. This can be easily explained by the presence of alloy fluctuations in the well material as well as by the larger internal electric field in the case of the InGaN/GaN QW [159].

Similar differences at low fluence between the two *m*-plane InGaN/GaN QW samples should be highlighted here. In sample *m*-QW1, the QW emission energy shows a typical S-shaped behavior when increasing the temperature [see figure 5.2(c)]: it undergoes a redshift which is followed by a blueshift upon increasing the lattice temperature from 15 to approximately 170 K. For higher temperatures, it starts to monotonously redshift and follows the expected Varshni's law. In the case of m-QW2, the S-shaped behavior of the emission energy is shifted toward much higher temperatures: the redshift in the emission energy continues up to 200 K and then starts to blueshift from 200 up to 300 K. The final redshift in the emission energy
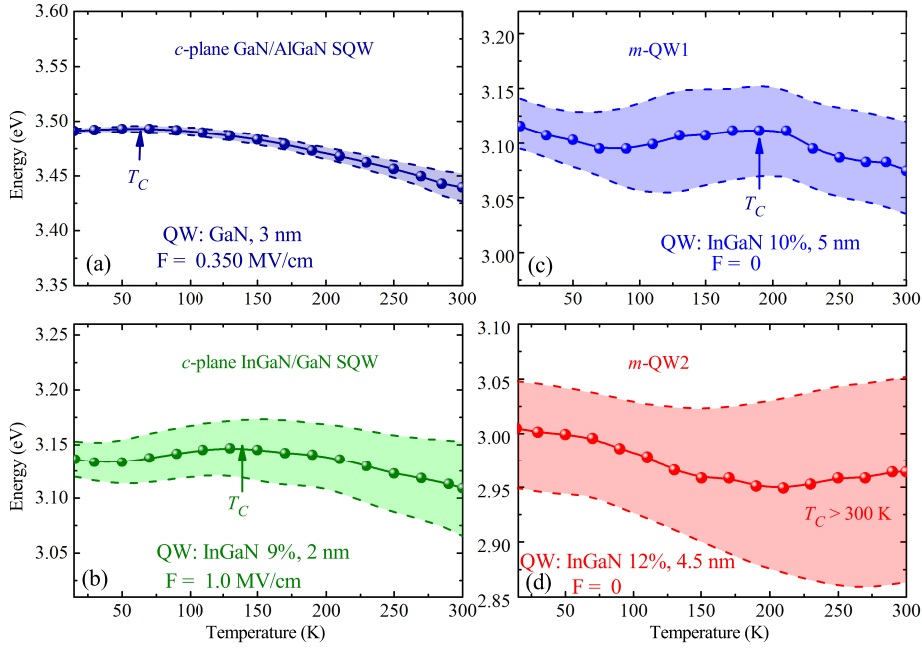
Figure 5.2 – Temperature dependence of the emission energy of the four QW samples and their corresponding FWHM. (a) *c*-plane GaN/AlGaN SQW, (b) *c*-plane InGaN/GaN SQW, (c) m-QW1, and (d) m-QW2.

likely occurs for temperatures higher than 300 K. This S-shaped variation of the emission peak covering a wide range of temperatures clearly evidences a deeper localization potential landscape in m-QW2, which is also consistent with the larger FWHM measured at 10 K for this sample (100 meV), compared to the 45 meV measured for the *m*-QW1 sample in good agreement with the structural analysis.

In order to emphasize the varying weight of carrier localization in the four QW samples, one can compare the characteristic temperature T_c, which corresponds to the temperature beyond which carriers are delocalized (mobility edge [160]), when the peak energy starts to recover its Varshni dependence. From figure 5.2, in agreement with structural analysis and the FWHM measured at low temperature, we observe that m-QW1 has a $T_c = 175$ K significantly smaller than *m*-QW2 ($T_c > 300$ K) which confirms that the carrier recombination dynamics in *m*-QW2 are much more influenced by disorder compared to *m*-QW1. A similar trend is obtained when comparing the two *c*-plane samples. The InGaN/GaN SQW exhibits a $T_c = 140$ K almost twice larger than that of the GaN/AlGaN SQW ($T_c = 75$ K).

In addition, figure 5.3 shows the Arrhenius dependence of the PL intensity of the four studied QW samples. It confirms that both *m*-plane QWs are less sensitive to non-radiative recombinations compared to their *c*-plane counterparts. We also observe that the *c*-plane GaN/AlGaN SQW shows a less pronounced decrease in PL intensity at relatively low temperature compared
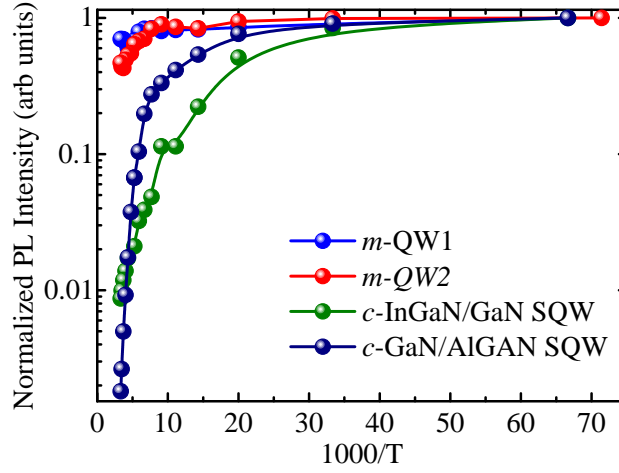
to the *c*-plane InGaN/GaN SQW.

Figure 5.3 – Arrhenius plots of the integrated PL intensities normalized to their value at 15 K probed under low injection non resonant excitation.

Hence, with the structural and temperature-dependent PL study, we deduce that the four samples have various electric fields and different degrees of disorder. The two *c*-plane samples (GaN/AlGaN SQW and InGaN/GaN SQW) will be used in the following to probe the influence of carrier localization in the presence of an electric field. The influence of disorder in the absence of any internal electric field will then be studied thanks to the two *m*-plane samples. The structural parameters and PL linewidths at low temperature are summarized in Table 5.1.

Table 5.1 – Structural parameters and PL linewidths at low temperature of the analyzed samples.

	c-plane GaN/AlGaN	*c*-plane InGaN/GaN	*m*-QW1	*m*-QW2
In content in the QWs (%)	0	9	10	12
Al content in the barriers (%)	9	0	0	0
QW thickness (nm)	3	2	5.0±0.5	4.5±0.5
Number of QWs	1	1	5	5
Electric field (MV/cm)	0.35	1.0	none	none
FWHM at 10 K (meV)	8	26	45	100
T_c(K)	75	140	175	>300

5.2.3 Temperature-dependent TR-PL

In order to evaluate the impact of localization, the temperature dependent PL decay time is employed to estimate the localization center density as well as their characteristic localization energy [147]. The temperature dependence of the QW effective lifetime of these samples was measured at a low excitation fluence of about ∼ 100 nJ/cm^2, which corresponds to an estimated injected carrier density < 10^{10} cm^{-2}, a value much lower than the estimated Mott

density for these QWs [140, 130]. Under this condition, the effective lifetime τ_{eff} was measured by integrating over the whole QW emission energy range and by fitting the corresponding PL decay with a single exponential.

Both c-plane QWs exhibit a reduction in τ_{eff} when increasing the temperature (above 50 K for the InGaN/GaN SQW and above 150 K for the GaN/AlGaN SQW), demonstrating the predominance of non-radiative recombinations in the dynamical behavior of these samples at high temperatures (see figure 5.4). the fast activation on non-radiative channels in both c-plane QWs conceals the localization effect, thus only the two m-plane samples are investigated.
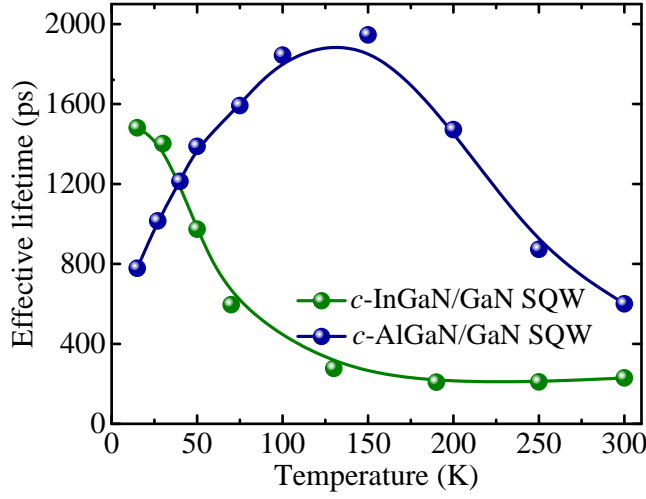

Figure 5.4 – QW PL effective lifetime for the c-plane GaN/AlGaN SQW and the c-plane InGaN/GaN SQW samples probed under low injection condition.

The τ_{eff} value of m-QW1 remains constant when increasing the temperature up to ∼ 100 K and then starts to monotonously increase for higher temperatures. However, τ_{eff} of m-QW2, apart from a slight increase for temperatures below 100 K, remains constant when increasing the temperature up to ∼200 K and then only slightly increases for higher temperatures. The small increase observed in τ_{eff} around 100 K may be attributed to the relaxation of carriers into deeper localization states, which is consistent with the onset of the emission redshift occurring at those temperatures.

The τ_{eff} dependence upon temperature was modeled using the same model as the one used in Ref. [147]. In this model, the effective lifetime τ_{eff} of excitons is modeled assuming that thermal equilibrium between the free and localized exciton populations holds. The radiative lifetime of free excitons is given by [161]

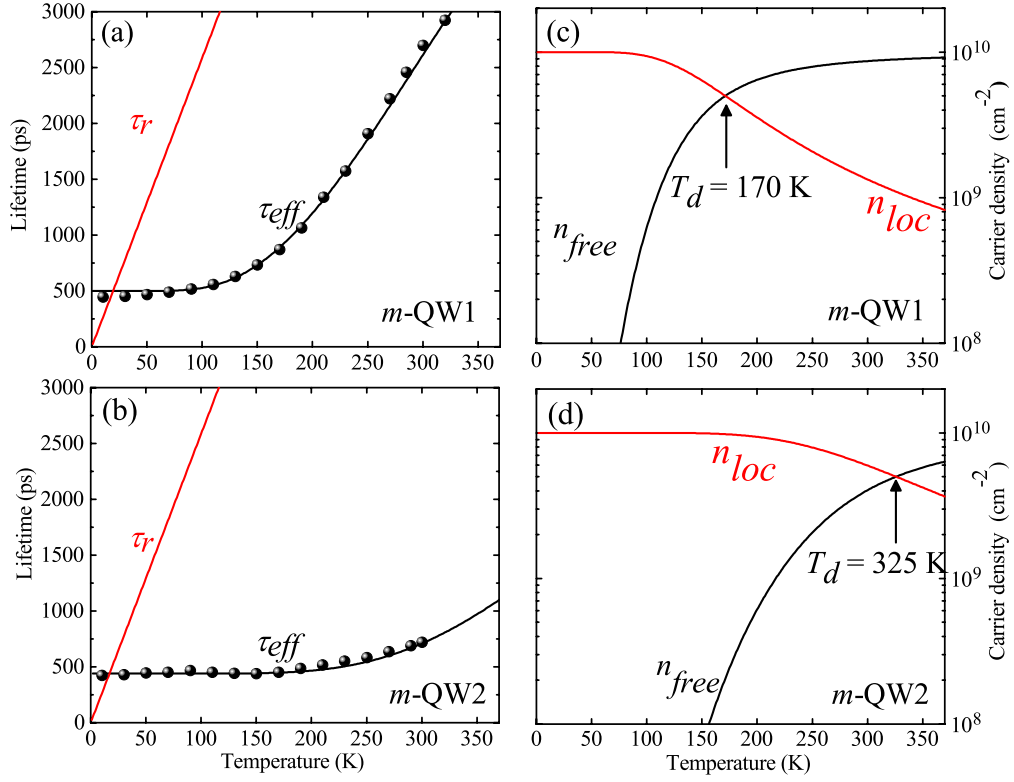$$\tau_r = \frac{6Mk_BT}{\hbar^2 k_\parallel^2}\tau_0, \tag{5.1}$$

Figure 5.5 – Comparison of the PL characteristics of the two m-plane InGaN/GaN QW samples probed under low injection condition ($\sim$ 100nJ/cm^2). Measured QW effective lifetime (black circles), as well as theoretical radiative (red solid line) and computed effective lifetime (black solid line) for samples (a) m-QW1 and (b) m-QW2. Densities of free and localized excitons, deduced from our modeling, are shown for (c) m-QW1 and (d) m-QW2. The arrows mark the temperature at which the free and localized carrier densities become equal, i.e., the delocalization temperature T_{d}.

where τ_0 denotes the radiative lifetime of free excitons at $k_\parallel = 0$, M denotes the exciton effective mass, and $k_\parallel$ is the in-plane wave vector of free excitons within the light cone. The linear dependence of the free exciton lifetime on temperature originates from the excitation of excitons out of the light cone when raising the temperature. The effective free exciton lifetime $\tau_{\mathrm{eff}}^{\mathrm{fr}}$ in the presence of non-radiative recombinations can be modified according to

$$\frac{1}{\tau_{eff}^{fr}} = \frac{1}{\tau_r} + \frac{1}{\tau_{nr}},$$
(5.2)

where τ_{nr} usually features a thermally activated behavior with a characteristic activation energy E_A given by

$$\tau_{\mathrm{nr}} = \tau_{\mathrm{nr},0} \exp\left(-\frac{E_A}{k_B T}\right).$$
(5.3)

Eventually, in the presence of disorder in our structure, we should consider the effect of localization. The latter was modeled assuming thermal equilibrium between free exciton and

localized exciton populations via Saha's law [138]. The ratio between localized and free exciton densities are then defined by

$$\frac{n_{fr}}{n_{loc}} = \frac{2M_x k_B T}{\pi \hbar^2 N_D} \exp\left(-\frac{E_{loc}}{k_B T}\right) \tag{5.4}$$

where M_x is the exciton mass, E_{loc} is the localization energy, and N_D is the density of localization centers. Considering a characteristic decay time for localized excitons τ_{loc}, the effective decay time of excitons (considering both localized and free excitons) in the QW can be written as

$$\frac{1}{\tau_{\text{eff}}} = \left(\frac{n_{\text{loc}}}{\tau_{\text{loc}}} + \frac{n_{\text{fr}}}{\tau_{\text{eff}}^{\text{fr}}}\right) / (n_{\text{loc}} + n_{\text{fr}}), \tag{5.5}$$

where n_{loc} and n_{fr} denote the localized and free exciton densities, respectively. Owing to the quenched diffusion of localized excitons toward non-radiative centers and their 0D-like character, their effective lifetime is expected to be temperature independent. The value of τ_0 was taken equal to 10 ps in our simulations, in agreement with Ref. [147]. Hence, this fitting procedure implies five main parameters: τ_{loc}, E_{loc}, N_D, $\tau_{nr,0}$, and E_A. Since E_{loc} is a measure of the localization energy, it has been chosen equal to the FWHM at low temperature. Here, τ_{loc} has been set to reproduce the lifetime measured at low temperature (i.e., below 100 K). N_D has been used to obtain a good fitting in the intermediate temperature range (100-200 K) where free excitons start to contribute to the luminescence. Finally, $\tau_{nr,0}$ and E_A have been tuned to take into account the activation of non-radiative defects at elevated temperature (200-300 K). More precisely, $\tau_{nr,0}$ gives the amplitude of the lifetime reduction and E_A monitors at which temperature it occurs.

The black solid line in figure 5.5(a) shows the results of this fitting for m-QW1 using the parameters: $\tau_{loc} = 500\pm20$ ps, $N_D = 8 \pm 1 \times 10^{11}$ cm^{-2}, and $E_{loc} = 45$ meV. The value of the non-radiative lifetime and the activation energy for the non-radiative recombination channel were considered to be $\tau_{nr,0} = 100$ ps, and $E_A = 200$ meV. Note that, due to the relatively small contribution of non-radiative recombinations at room temperature, the value of $\tau_{nr,0}$ and E_A should be considered with caution since different couples of $(\tau_{nr,0}, E_A)$ lead to similar fitting results.

From this model, the density of free and delocalized carriers as a function of temperature as shown in figure 5.5(c). The two densities become equal at $T_d = 170$ K, which remains in reasonable agreement with the delocalization temperature (T_c) of carriers deduced from the variation in the QW emission energy. When applying the same model to m-QW2, the localized excitons were found to dominate the population of carriers in the QW up to room temperature ($T_d = 325$ K). The black solid line in figure 5.5(b) shows the results of this fitting, with τ_{1oc}, N_D and E_{loc} values of 450 ±20 ps, $1.0 \pm 0.1 \times 10^{12}$ cm^{-2}, and 100 meV, respectively.

It should be pointed out that, contrary to what has been observed in other systems [162], both samples exhibit a similar lifetime at low temperature. This exemplifies that, in our case, localization effects cannot be just considered as a perturbation, but instead they drastically affect the recombination properties of carriers at low temperature [163].

Comparing the two samples, we can notice that the density of localized centers are similar in the two cases and are in agreement with the typical scale of indium fluctuation observed by atom probe tomography [28]. The increased degree of QW disorder in sample m-QW2, as manifested by larger values for the localization energy, causes recombination dynamics that are governed by carrier localization even up to room temperature. By contrast, the carrier dynamics in sample m-QW1 appear to be far less affected by localization, i.e., for temperatures above 170 K, the emission is dominated by the recombination of free carriers.

5.2.4 High injection TR-PL at low temperature

This section discusses a set of experiments carried out on all samples under high optical injection and modeling of carrier recombination dynamics.

A. Modeling of TR-PL in the high density regime

High injection TR-PL as detailed in chapter 2 at 4 K were performed on the four samples. The spectral shape has been fitted following the model used in Refs. [140, 130]. In this model, the necessary parameters are the effective masses of electrons and holes as well as the band splitting between the A and B excitons. For the c-plane samples (InGaN/GaN and GaN/AlGaN), the transverse masses have been extracted from $\mathbf{k} \cdot \mathbf{p}$ simulations and taken equal to: $m_{A*} = 1.8\ m_0$, $m_{B*} = 0.45\ m_0$, and $m_e = 0.2\ m_0$ [130]. The valence band splitting has been estimated to be around 8 meV. Concerning m-plane samples, since the effective masses are highly anisotropic, we use the geometric mean value of the in-plane effective masses [164]

$$m_m^* = \sqrt{m_{\mathrm{m}\parallel}^* m_{\mathrm{m}\perp}^*},$$
(5.6)

where $m_{\mathrm{m}\parallel}^*$ is the effective mass along the c axis, and $m_{m\perp}^*$ is the one in the perpendicular direction. The value of hole masses has been extracted from $\mathbf{k} \cdot \mathbf{p}$ simulations (see figure 5.6) applied to a 5.0 nm thick m-plane $In_{0.1}Ga_{0.9}N$/GaN QW: $m_{A\perp} = 0.185\ m_0$, $m_{A\parallel} = 1.83\ m_0$, $m_{B\perp} = 1.60\ m_0$, $n_{B\parallel} = 0.2\ m_0$ and $m_e = 0.2\ m_0$. Note that the valence band A2 (first excited state of the A band) is not considered for the modeling of experimental PL spectra since this subband has a negligible overlap with the first conduction band due to the symmetry of its wavefunction.

Once the carrier density is determined, we are able to accurately estimate the Auger coefficient thanks to the temporal behavior of the luminescence. Hence, experimental PL decays at $T = 4$ K were fitted with a time derivative ABC model

$$\frac{dn}{dt} = -An - \int_{E_{\mathrm{OW}}}^{\infty} R_{\mathrm{sp}}(E)dE - Cn^3.$$
(5.7)

The only free parameter is the characteristic radiative lifetime τ_r, whose value is considered to be the same in the two m-plane samples. To avoid extra complexity at this stage, the Auger coefficient was chosen to be independent of the carrier density and without discrimination of the electron-electron-hole and electron-hole-hole Auger recombinations. It is worth mentioning that the initial carrier density is in the range of a few times 10^{12} cm^{-2}, which is above the Mott density for GaN QWs [130]. Moreover, the SRH non-radiative recombination rate is
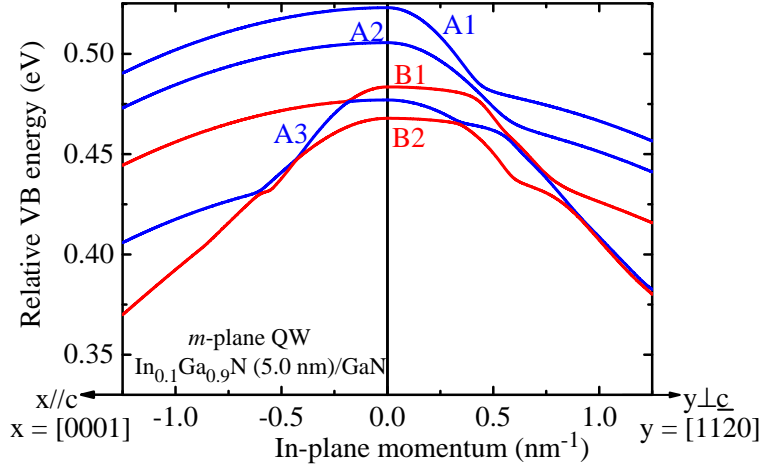
Figure 5.6 – In-plane VB dispersion of the fundamental QW energy levels as calculated from Schrödinger-$\mathbf{k} \cdot \mathbf{p}$ simulations for an m-plane $In_{0.1}Ga_{0.9}N$ (5.0 nm)/GaN QW.

considered to be negligible in all of the studied samples at low temperature ($A = 0$).

The carrier density at early delays is determined by fitting the PL spectral lineshape. Since m-QW1 does not show any droop signature on TR-PL data, we adjust the B term to fit the PL decay of m-QW1 under high injection condition (assuming $C = 0$). Finally, since both samples present similar lifetimes at low injection at $T = 4$ K, we assume that the radiative term is equal for the two samples. Thus, to fit the dynamics of m-QW2 under high injection, C is the only free parameter. Hence, for each decay trace, we consider a single/unique fitting parameter, which ensures the robustness of this procedure.

B. c-plane GaN/AlGaN and InGaN/GaN QWs

Figures 5.7(a) and 5.7(b) show streak images for the two c-plane SQW samples [c-plane GaN (3 nm)/$Al_{0.09}Ga_{0.91}N$ and c-plane $In_{0.09}Ga_{0.91}N$ (2 nm)/GaN SQWs] recorded at 4 K under identical high injection conditions (~ 300 μJ/cm^2). In both cases, it reveals that, at early delays, the broad emission of the QW and then a progressive narrowing of its emission line with increasing time delay. These features are attributed to the initial band filling associated with the presence of a high density e-h plasma followed by its subsequent decay, as explained in detail in Refs. [130] and [162].

These streak images have been analyzed following the model and parameters used in Ref. [130]. Figure 5.7(c) presents time-resolved spectra extracted from streak images at early delays (t= 0-20 ps) for both samples. By fitting the experimental results with our e-h plasma modeling, a similar QW carrier density is deduced at early delays ($t \approx 10$ ps) for both samples: $n_0 = (1.50 \pm 0.15) \times 10^{13}$ cm^{-2} in the GaN/AlGaN SQW and $n_0 = (1.45 \pm 0.15) \times 10^{13}$ cm^{-2} in the InGaN/GaN SQW, evidencing the efficient transfer of carriers from the barriers to the QW. However, as shown in figure 5.7(b), even if the initial carrier density is identical, the dynamics of the two samples differ dramatically. The InGaN/GaN QW sample experiences a fast decay
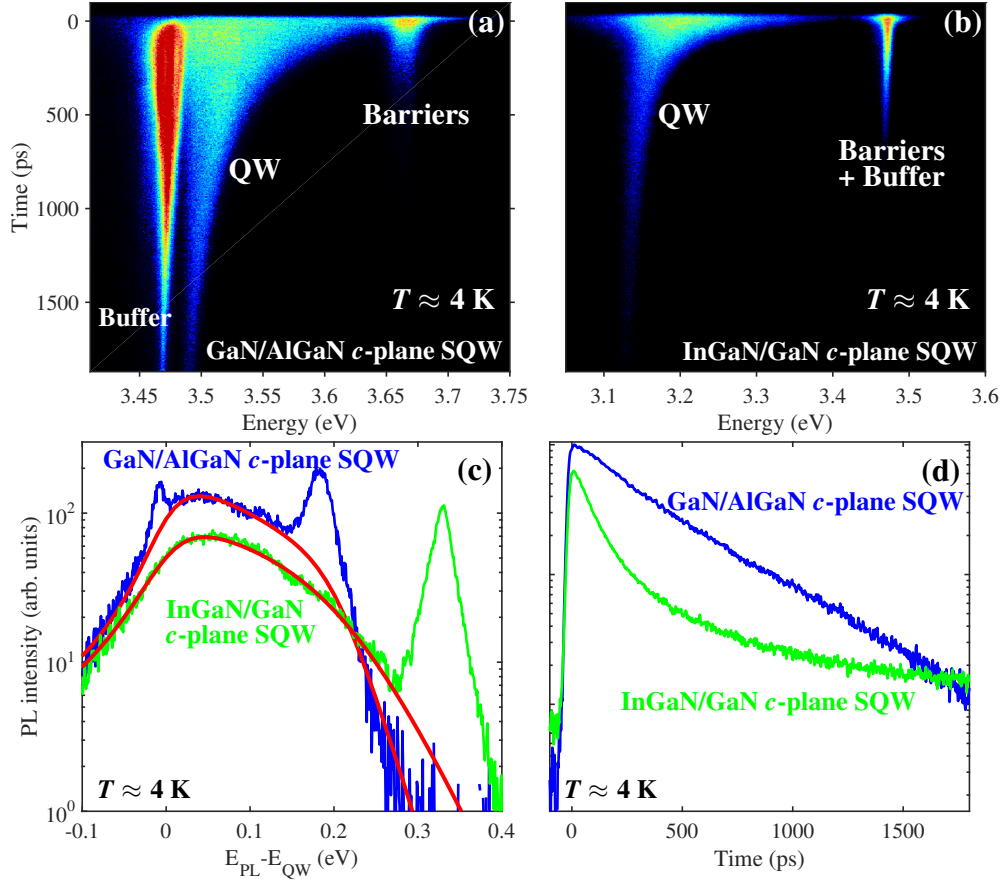
Figure 5.7 – Comparison of the c-plane GaN/AlGaN and the c-plane InGaN/GaN SQW systems probed under high injection (300 μJ/cm^2 at T = 4 K. Streak image of (a) the c-plane GaN(3 nm)/Al$_{0.09}$Ga$_{0.91}$N In$_{0.09}$Ga$_{0.91}$N(2 nm)/GaN SQW recorded at T = 4 K. (c) time-resolved spectra (from 0 to 20 ps) obtained at 4 K and under high injection conditions for the GaN/AlGaN QW (blue) and the InGaN/GaN QW (green) and the corresponding e-h plasma modeling (red lines). For the sake of comparison, the spectral axis has been shifted to match the position of the two QW ground states (E$_{QW}$) in the low density regime. (d) PL intensity decays integrated over the whole QW emission energy range [GaN/AlGaN QW (blue line) and InGaN/GaN QW (green line)].

at early delays (i.e., at high carrier density). At this stage, this fast decay can be ascribed to either radiative or non-radiative processes. Nonetheless, it is important ot recall that the instantaneous PL intensity is proportional to the radiative rate [165, 166] and to the carrier density which is similar in the two samples at early delays. The PL intensity at early delay is slightly higher in the GaN/AlGaN sample [see figure 5.7(d)]. As a consequence, since the initial carrier density is nearly the same, the difference in PL intensity at early delays demonstrates that the initial radiative lifetime is shorter in the case of the GaN/AlGaN SQW sample. Such a difference is due to the smaller built-in electric field in low Al-content GaN/AlGaN QWs compared to their InGaN/GaN counterparts [159].

In order to exclude any influence of the screening of the built-in electric field, we performed Schrödinger-Poisson simulations. The square modulus of the e-h wave function overlap at low carrier density is estimated to be around $\left| \langle f_e | f_h \rangle \right|^2 \approx 0.62$, assuming an internal electric

field value of 1 MV/cm [157]. This relatively high overlap is the consequence of a very thin QW (2 nm). At early delays, the e-h wave function overlap is increased up to $|\langle f_e | f_h \rangle|^2 \approx 0.9$ due to the screening of the electric field induced by free carriers. Therefore, an increase in the radiative rate by at most a factor of 1.5 at early delays is expected in our c-plane InGaN/GaN QW. However, the observed change by a factor larger than 13 in the lifetime between early delays ($\tau = 105 \pm 5$ps) and longer delays ($\tau = 1400 \pm 100$ps) indicates that the main contribution to the lifetime increase cannot be attributed to a time-dependent screening of the internal electric field.

Hence, since it cannot originate from the radiative component, we can unambiguously attribute the fast decay observed in the InGaN/GaN SQW to a non-radiative recombination process that is activated under high injection conditions. This confirms that, compared to its GaN/AlGaN counterpart, the c-plane InGaN/GaN SQW is indeed affected by the efficiency droop. The main difference between the two systems is the use of a ternary alloy as well material for the InGaN/GaN QW. Hence, the different behavior between the two types of heterostructures likely originates from disorder in the InGaN compound. However, as the internal electric field is more pronounced in the InGaN/GaN SQW compared to its GaN/AlGaN counterpart, at this stage, it cannot fully discard the influence of a stronger internal electric field [167, 168].
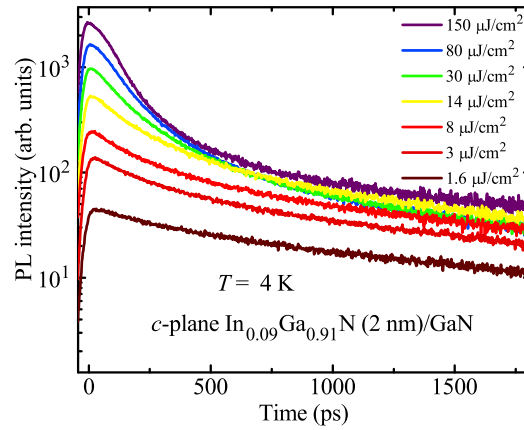
Figure 5.8 – Power-dependent tr-PL for the c-plane InGaN/GaN SQW measured at $T = 4$ K. The PL intensity has been integrated between 3.1 and 3.3 eV

To further confirm the origin of the fast initial decay, we performed power-dependent TR-PL measurements for the c-plane InGaN/GaN SQW sample. As depicted in Fig. 5, we observe that the fast initial decay is only activated when the fluence increases. This power-dependent behavior indicates the presence of Auger recombination: the Auger term becomes predominant only in the high density regime.

C. *m*-plane InGaN/GaN QWs

In order to verify our hypothesis concerning the major impact of carrier localization on the

high density recombination dynamics, parasitic influence of the QCSE is necessary to be eliminated. The latter is expected to affect radiative and non-radiative rates when the carrier density changes [168]. We thus investigate the two above mentioned *m*-plane samples that are free from built-in polarization field and primarily differ only by the QW disorder potential. It should be noted here that the efficiency droop has also been observed in *m*-plane QW samples by electrical [169, 170] and optical injections [171], which confirms the relevance of our approach.
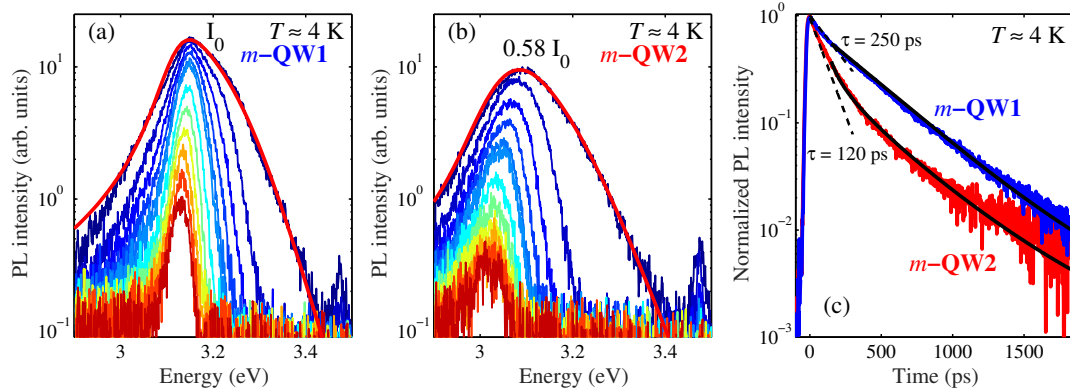

Figure 5.9 – Comparison of *m*-QW1 and *m*-QW2 probed under high injection (300 μJ/cm^2) at $T \approx$ 4K. (a) and (b) tr spectra obtained at 4 K, and under high injection conditions for samples *m*-QW1 and *m*-QW2, respectively. The PL spectra are extracted every 50 ps after the excitation up to a time delay of 250 ps and then every 100 ps. The red solid line shows a typical fit of the spectra with our e-h plasma model. The integrated PL intensity at early delays is displayed on top of each series of spectra for both samples. I_0 is the integrated PL intensity at early delays for *m*-plane QW1 and is taken as a reference. (c) PL decays, integrated over the whole QW emission energy range, for the two *m*-plane InGaN/GaN QWs. The dashed lines show the initial decay time. The black solid lines illustrate the fitting of the decays of the investigated samples.

Figures 5.9(a) and 5.9(b) show TR-PL spectra obtained at 4 K at high excitation densities for the two *m*-plane InGaN/GaN MQW samples. As a result of phase space filling, both *m*-QW1 and *m*-QW2 samples exhibit a large and asymmetric broadening at early delays followed by a reduction in the emission linewidth with increasing delay time. By modeling the PL spectra at early delays, we can extract the initial carrier densities in both samples leading to: $n_0 = 7.4 \pm 0.8 \times 10^{12}$ cm^{-2} in *m*-QW1 and $n_0 = 7.5 \pm 0.8 \times 10^{12}$ cm^{-2} in *m*-QW2 samples. Despite these similarities, the two samples exhibit notable differences. the PL peak energy as a function of time delay remains constant for *m*-QW1, while *m*-QW2 experiences a large redshift (~80 meV). This behavior indicates that not all localization centers are saturated even at those large excitation densities in *m*-QW2, which is consistent with the higher value for the estimated localization energy in this sample. Hence, even if excitons are localized at low temperature under low injection in both samples, the degree of localization plays an important role in the dynamics under high injection.

Figure 5.9(c) displays the PL decays, integrated over the whole QW emission energy range, for the two *m*-plane InGaN/GaN MQWs measured at T $\approx$ 4K. The dynamics of carrier recombination in *m*-QW1 differ significantly from those in *m*-QW2. While the PL intensity decays

almost monoexponentially in *m*-QW1, the decay rate shows a noticeable time/carrier density dependence in *m*-QW2. As shown by the black dashed line, the PL intensity of *m*-QW2 exhibits a decay rate that is twice faster at early delays ($\tau \sim 120$ ps for *m*-QW2 and 250 ps for *m*-QW1). The comparison of the absolute PL intensity in both samples together with the dynamics of the PL intensity decay provides clear evidence for a fast non-radiative channel that becomes active at high injection densities in the *m*-QW2 sample, i.e., the *m*-plane MQW with a higher degree of disorder.

In order to comfort our assignment of the fast recombination component under high injection in *m*-QW2 to non-radiative recombinations, we performed fluence-dependent PL measurements on the two *m*-plane samples. They have been excited by a 355 nm pulsed
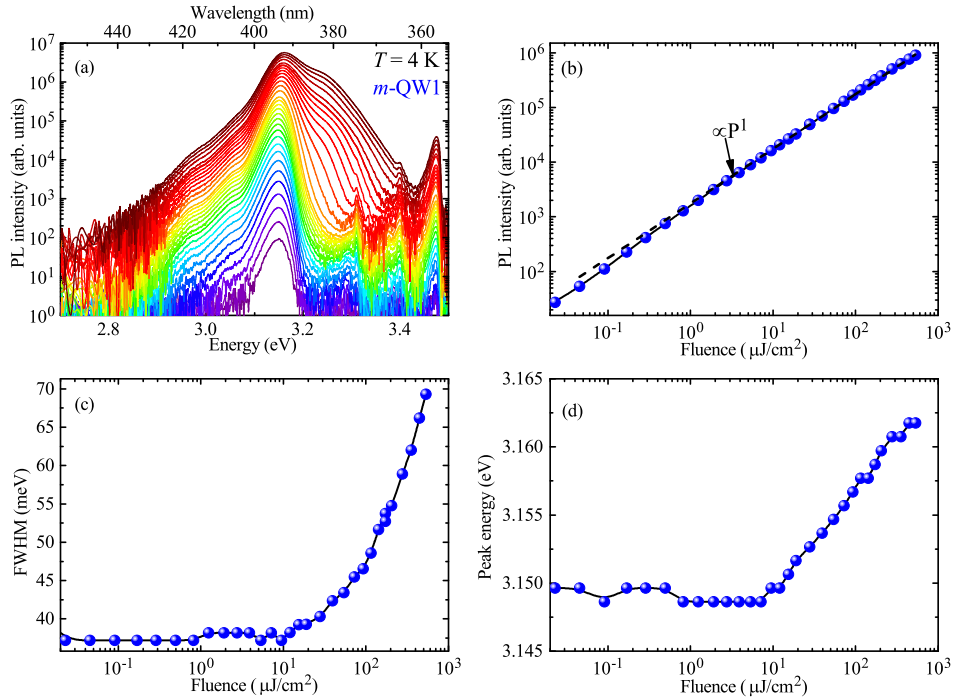

Figure 5.10 – Fluence dependent emission characteristics of *m*-QW2 recorded at $T = 4$ K. (a) PL spectra as a function of fluence from 0.02 up to 500 μJ/cm^2. (b) Integrated PL intensity of the QW emission as a function of fluence. (c) FWHM of the QW PL emission as a function of fluence. (d) Energy of the PL peak of the QW emission as a function of fluence.

laser with a pulse width of 5 ps and a repetition rate of 80.5 MHz. Figure 5.10(a) displays PL spectra of *m*-QW1 recorded at $T = 4$ K as function of fluence ranging from 0.02 up to 500 μJ/cm^2. We observe an important broadening on the high energy side when the fluence is increasing above 10 μJ/cm^2 which demonstrates that band filling occurs under high injection. Contrary to the TR-PL results presented, we can notice that the spectral shape does not exactly correspond to the emission coming from an e-h plasma. This is due to the time-integrated nature of the measurement, the recorded PL spectrum corresponds to an average over a large range of carrier densities and results in a mixture of e-h plasma and excitonic PL emission.

Therefore, it is difficult to extract quantitative information about the efficiency droop from such measurements but it can however provide some useful qualitative insights. Indeed, as suggested by our TR-PL measurements on m-QW1, we do not observe any signature of the efficiency droop in figure 5.10(b), which exhibits a nearly linear relationship between the QW PL intensity and the laser fluence.

Fluence-dependent PL measurements performed on m-QW2 exhibit a different behavior from those performed on m-QW1. As shown in figure 5.11, m-QW2 presents a similar broadening on the high energy side when the laser power is increasing. However, here, we observe that above 30 μJ/cm^2, the integrated PL intensity experiences a sub-linear dependence with laser fluence, highlighting the appearance of a non-radiative channel under high injection. This observation is in agreement with the non-radiative fast component observed under high injection in our TR-PL experiments.
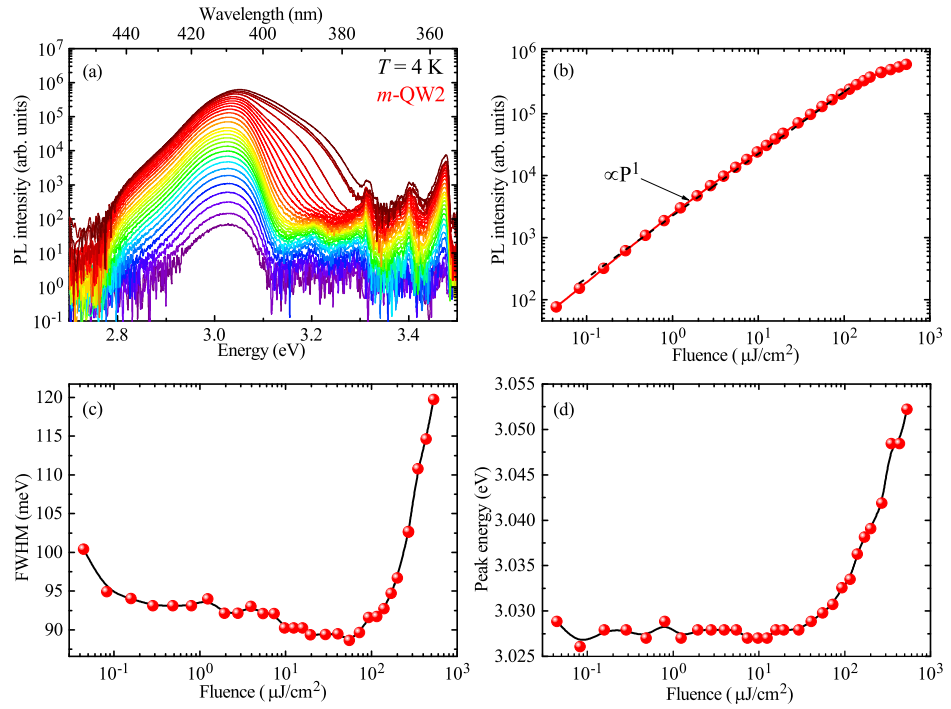
Figure 5.11 – Fluence dependent emission characteristics of m-QW2 recorded at T = 4 K. (a) PL spectra as a function of fluence from 0.02 up to 500 μJ/cm^2. (b) Integrated PL intensity of the QW emission as a function of fluence. (c) FWHM of the QW PL emission as a function of fluence. (d) Energy of the PL peak of the QW emission as a function of fluence.

To further illustrate the difference between the two samples, figure 5.12 shows the evolution of the normalized PL efficiency (defined as the PL intensity divided by the laser power) as a function of fluence. From this figure, we clearly observe that (i) m-QW2 exhibits a more pronounced decrease in the PL efficiency and that (ii) it occurs for a lower fluence compared to m-QW1.

Figure 5.12 – Normalized PL efficiency (PL intensity divided by fluence) as a function of the fluence recorded at T = 4 K for m-QW1 and m-QW2 samples.
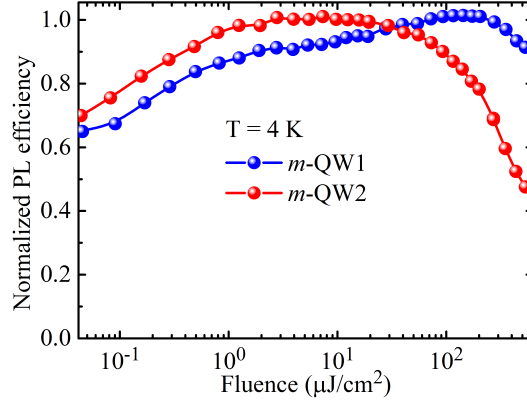
To obtain a quantitative evaluation about the fast non-radiative channel activated under high injection, we fit the PL decays with a modified ABC model taking into account Fermi filling effects. Finally, to prevent the possible influence of any feeding of carriers from the barriers resulting from our nonresonant pumping scheme, the fit is performed only 150 ps after the excitation pulse. At such delays, the luminescence from the barriers has completely disappeared, indicating that there is no significant carrier feeding from the barriers anymore. Moreover, the SRH non-radiative recombination rate is considered to be negligible in all the studied samples at low temperature ($A = 0$). For m-QW1, the PL decay curve is reproduced accurately with $C = 0$ [see figure 5.9(c)], which means that the recombination in this sample can be considered as of fully radiative origin. On the other hand, to reproduce the PL decay in m-QW2, it is necessary to take into account a finite C coefficient: $C_{2D} = 2.8 \times 10^{-16}$ cm^4/s ($C_{3D} = 7.0 \times 10^{-29}$ cm^6/s). This value is relatively high compared to previous reports [154]. However, our extracted B coefficient is also higher: $B_{2D} = 2.9 \times 10^{-2}$ cm^2/s ($B_{3D} = 1.4 \times 10^{-8}$ cm^3/s). Such high values can be understood by the absence of QCSE in m-plane QWs [168] and the low temperature, hence explaining the carrier dynamics.

To further assess the carrier density dependence of the observed non-radiative channel, we performed power-dependent TR-PL measurements at low temperature ($T = 6$ K) on the two above mentioned m-plane samples. Figure 5.13 presents the evolution of the initial PL lifetime e as a function of laser fluence. This confirms that, at low fluences (i.e., below 2 μJ/cm^2), the initial lifetime is similar for both m-plane samples. When the fluence is increasing, the PL lifetime of m-QW2 shows a slight decrease, whereas the of m-QW2 decreases by more than a factor 2.3. This behavior confirms the dominance of a density activated non-radiative channel in the case of m-QW2. In addition, time-integrated power-dependent PL measurements performed at low temperature on both samples evidenced a much more pronounced efficiency droop in m-QW2 in line with TR-PL results.

This pronounced difference between the two samples is attributed to the effect of the much larger carrier localization in m-QW2. We tentatively attribute this large value of the Auger coefficient to the three-dimensional (3D) confinement of carriers in this system. Because

of this confinement in real space, a spread of the carrier wave function is expected in the reciprocal space. Since the Auger process requires both energy and momentum conservation, an extension of the wave function in k space increases the number of possible particles that can interact in this three-particle process. Hence, the Auger recombination rate is indeed expected to be enhanced by the relaxation of the k-selection rule in the Auger scattering process. Such an enhancement has been already observed in other systems such as SiGe nanocrystals [172] or CdTe quantum dots [173]. In a similar way, one may expect that the breakdown of the k-selection rule, induced by localization, should lead to the enhancement of the Auger recombination process in InGaN. We note that Kioupakis et al. [152, 135] also reported, through a theoretical study, that phonon and alloy scattering in III-nitrides can significantly enhance the Auger recombination rate because of the relaxation of momentum conservation during the scattering process.
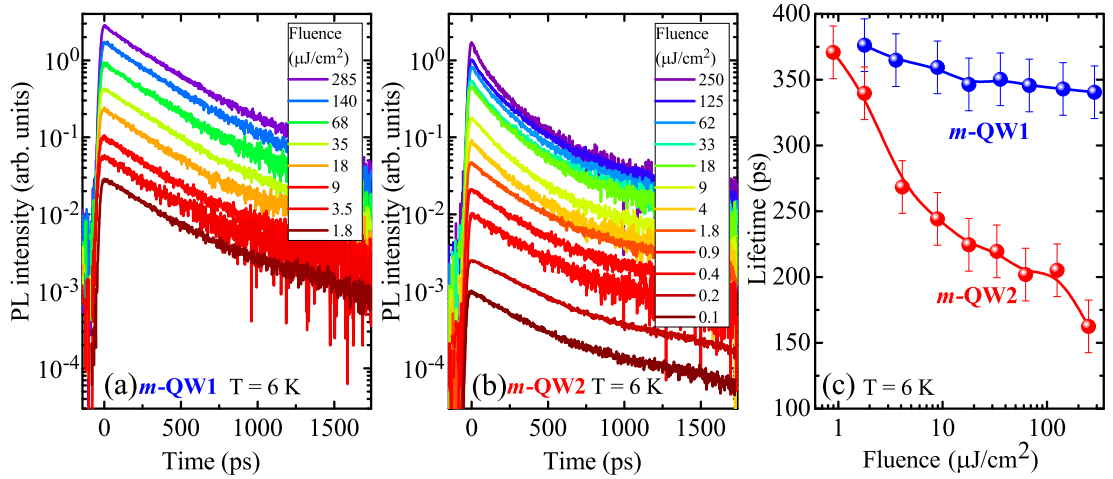
Figure 5.13 – (a) and (b) Comparison of m-QW1 and m-QW2 QW PL decay probed at low temperature (T = 6 K) as a function of laser fluence. The PL intensity has been spectrally integrated over the entire QW emission range. (c) Corresponding fluence dependence of the QW PL lifetime at early delays for m-QW1 and m-QW2.

Finally, when we compare the dynamics under high injection of m-QW1 and the c-plane samples, we notice that m-QW1 behaves like the c-plane GaN/AlGaN SQW. However, when the FWHM at low temperature is considered, the structural disorder of m-QW1 is a priori higher than the one of the c-plane InGaN/GaN SQW. As a possible explanation, the enhanced Auger recombination in this sample may be due to the influence of the internal electric field which is known to enhance the weight of localization effects [174]. However, other mechanisms than disorder may play a role in the enhancement of Auger recombination in c-plane InGaN/GaN QWs.

5.3 Defect-assisted Auger recombination

5.3.1 Introduction

Regardless of alloy disorder, indirect Auger processes can also be strengthened by carrier scattering through phonons, and point defects, which relieve the energy and momentum conservation. In particular, the dependence of the Auger process on non-radiative defects has been recently pointed out [47]. As demonstrated in section 3.3, we elucidated the role of UL on the point defect density, which provides a pathway to investigate defect density dependent Auger processes. Here, we tune the defect density in InGaN/GaN single QW samples through a change in the thickness of an AlInN UL and evaluate its impact on Auger recombination using TR-PL at 300 K. The results are analyzed in the framework of a modified *ABC* model, which includes defect-assisted Auger recombination.

5.3.2 Laser fluence dependent PL and TR-PL

In this study, we characterize three samples having the same InGaN/GaN SQW with a ~12% In content and 2.7 nm width, but different thickness of $In_{0.15}Al_{0.85}N$ UL (0, 10 and 55 nm). First, we performed micro-PL and TR-PL as a function of laser fluence in the three samples, from low carrier density to the degenerate regime. Figure 5.14(a) presents the time-integrated PL
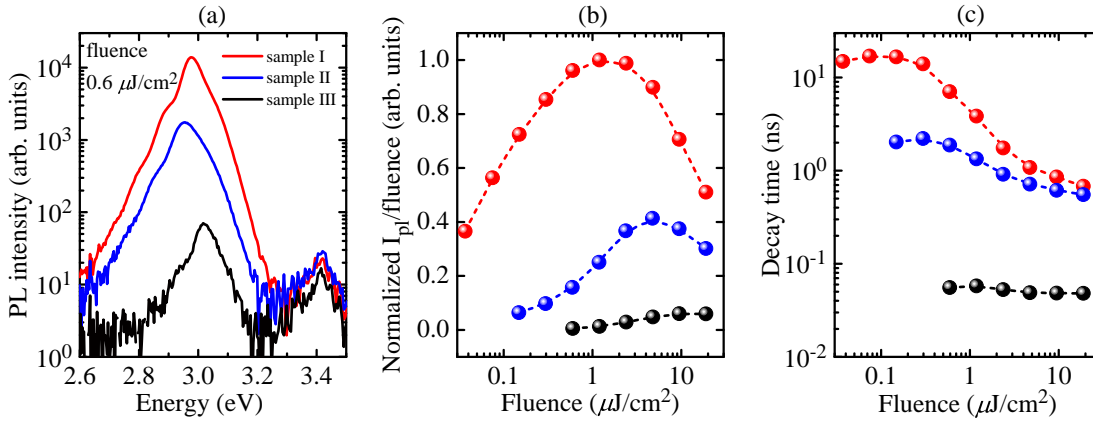
Figure 5.14 – (a) Time-integrated PL spectra of sample-I, II, III with 55, 10 and 0 nm thickness of InAlN UL measured at 0.6 μJ/cm^2 and 300 K. (b) Normalized ratios of QW I_{PL} to fluence in the three samples. (c) Corresponding QW PL decay time as a function of fluence in the three samples.

spectra of the three samples at 0.6 μJ/cm^2, corresponding to intermediate injection. The peak I_{PL} of QW luminescence is enhanced by more than two orders of magnitudes as the InAlN UL thickness increases from 0 to 55 nm, which indicates significant modulation of the defect density in the QW through variation of the UL thickness. Figure 5.14(b) presents the evolution of normalized ratios of QW I_{PL} to the fluence among the three samples, which corresponds to relative PL efficiency. The PL efficiency in defective sample-III only shows a monotonically increasing behavior, which indicates the dominant role of SRH recombination, even in the degenerate regime. On the contrary, the maximum PL efficiency in sample-II and -I shifts to lower fluence, which is in line with the fact that as the defect concentration increases, a

larger carrier density is required to enhance bimolecular recombination and saturate the SRH one. These features are consistent with the fluence dependent decay time shown in figure 5.14(c), which are extracted from the monoexponential fit of PL decays (figure 5.15 (a-c)) at early delay. For instance, the decay time for sample-III is dramatically shorter than that of sample-II and -I, and keeps nearly constant around 0.5 ns. The fast decay and low I_{PL} for sample-III evidence the strong SRH recombination. In contrast, in the case of sample-I, a slight increase of τ_{eff} within 0.2 μJ/cm^2 implies the saturation of SRH recombination. The τ_{eff} becomes shorter between 0.2-1 μJ/cm^2 together with an increase of PL efficiency in figure 5.14(b), which evidences the enhancement of bimolecular recombination, related to its approximate Bn^2 dependence and the screening of QCSE. As fluence increases up to 19 μJ/cm^2, the further decrease in decay time and the drop in PL efficiency suggest extra carrier losses, which result in efficiency droop.

Figures 5.15 (a-c) show the fluence dependent PL decays for sample-I, -II and -III, respectively. The decay times of sample-III are within ~ 50 ps, and appear as nearly monoexponential traces.
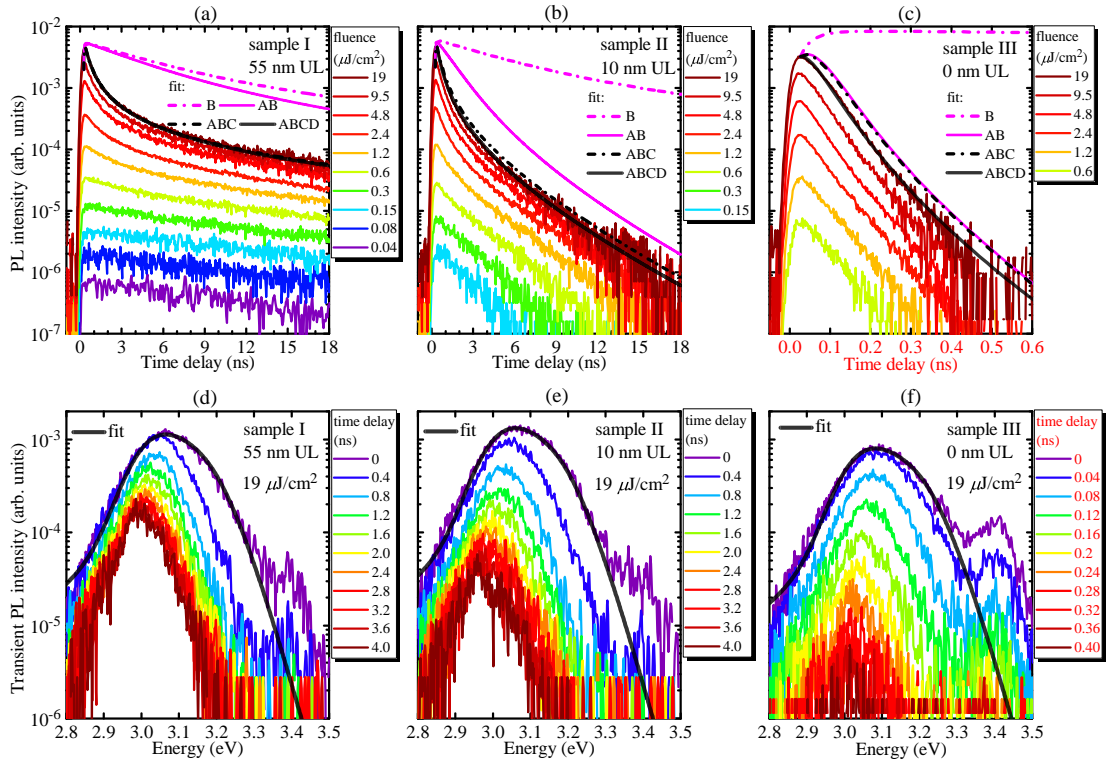
Figure 5.15 – (a-c) present the fluence dependent PL decay of QW emission (rainbow colors) of sample-I, -II, and -III, respectively. The simulated decays only considering the radiative recombination are presented as pink dash-dotted traces; The pink solid lines stand for the dynamics including radiative and SRH recombinations; The black dash-dotted lines are the fit with contribution of radiative, SRH and band-to-band Auger recombinations; the black solid lines are the fits taking into account the radiative, SRH, band-to-band and defect-assisted Auger recombinations. (d-f) are the corresponding time dependent spectra evolution of sample-I, -II and -III (rainbow colors). The black curves are the fits to extract carrier density based on Fermi's golden rule, which is estimated to be 1.4×10^{13} cm^{-2} for sample-I and -II, and 1.5×10^{13} cm^{-2} for sample-III.

Comparing sample-II and -I, they present a long monoexponential decay up to intermediate fluence, and subsequently fast non-exponential features occur at early delays. However, the decay time of sample-II (low fluence regime) is ~2 ns, which is much faster than in the case of sample-I, which is about 20 ns. Figures 5.15(d-f) show the corresponding time-dependent-spectrum evolutions for three samples at 19 μJ/cm^2 injection. All samples exhibit a red shift of the emission spectra as time evolves, which is mainly related to the descreening of the built-in field. Meanwhile, the broadened QW spectra toward GaN emission at early decay suggests that the carrier density is in the degenerate regime, and the subsequent linewidth narrowing is linked to the depopulation of injected carriers. To study the impact of point defects on Auger recombination in the droop regime, we quantified the carrier dynamics based on a modified *ABC* model taking into account defect-assisted Auger recombination.

We first extracted the initial carrier density by fitting the initial spectral line shape under 19 μJ/cm^2 fluence based on Fermi's golden rule [130, 140]. The fitting results are illustrated as black lines in figure 5.15, which well reproduce the Fermi's filling induced broadening of QW emission, and give the initial density 1.5×10^{13} cm^{-2} for sample-III and 1.4×10^{13} cm^{-2} for both sample-II and -I. Subsequently, we simulate the wavefunction overlap as a function of carrier density by the self-consistent Schrödinger-Poisson method in order to account for the descreening of QCSE during the decay. As shown in figure 5.16(a), the square of the
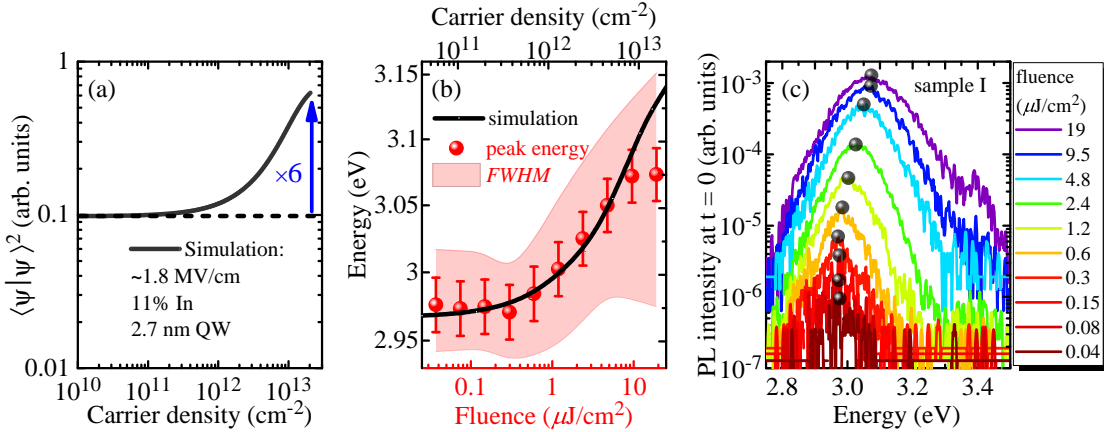
Figure 5.16 – (a) Carrier density dependent $\langle\Psi|\Psi\rangle^2$ square of the ground-state wave function simulated by Schrödinger-Poisson simulations. (b) Corresponding simulated blue shift of the ground state transition as a function of carrier density (black solid curve) and peak energy of I_{PL} at t=0 at each fluence in sample-I as shown in the next subfigure. (c) Fluence dependent transient PL spectra at t=0 of sample-I, where peak position of each I_{PL} are labeled as black dots.

ground-state wave function *osc* = $\langle\Psi|\Psi\rangle^2$ of e-h pairs remains constant around 0.1 when the density is below 5×10^{12} cm^{-2}. $\langle\Psi|\Psi\rangle^2$ for the ground state then increases by a factor of 6, as density increases up to 2×10^{13} cm^{-2}. To verify the relevance of our simulations, in figure 5.16(b) we compare the blue shift between the simulated QW energy and the measured peak energy of the transient PL spectra at t=0 (see figure 5.16(c)). The blue shift expected from simulations well matches the experiment as long as the density is below $\sim 5\times10^{12}$ cm^{-2}. The discrepancy visible at higher density is likely linked to the band gap renormalization effect [130, 175, 176], which was not included into the simulation for the sake of simplicity.

5.3.3 Modeling of carrier recombination dynamics

Next, we quantified the carrier recombination dynamics in a general form so as to compare our results with the standard *ABC* model:

$$\frac{dn}{dt} = -An - Bn^2 - Cn^3 - Dn^2, \tag{5.8}$$

where the four terms on the right-hand side of equation 5.8 account for the SRH, bimolecular, standard Auger, and defect-assisted Auger recombination, respectively. First, to evaluate the impact of QCSE on SRH recombination, we use a phenomenological formula, as proposed by A. David *et al.* [47, 129]:

$$An = osc^p \cdot A_0 n, \tag{5.9}$$

where the factor p depends on the degree of correlation between SRH and wavefuction overlap, A_0 is the SRH coefficient in the low injection regime. Second, the bimolecular recombination rate is expressed as:

$$Bn^2 = osc \cdot \int_{E_{QW}}^{\infty} R_{sp}(n, E) dE, \tag{5.10}$$

where $R_{sp}(n, E)$ is spontaneous emission rate described by Fermi's golden rule [130, 140], which captures the phase-space filling effect in the degenerate regime, the prefactor *osc* accounts for QCSE. Third, in the three-particle Auger process, the inter-band transition of e-h pairs is also subjected to the QCSE and phase-space filling [133], equivalent to radiative recombination. For the sake of simplicity while preserving the physical meaning, we assume that in Auger process the third particle is excited by the energy transfer from a bimolecular-like recombination of an e-h pair:

$$Cn^3 = C_0 \cdot n \cdot Bn^2, \tag{5.11}$$

where C_0 features the Coulomb interaction between the third particle and the e-h pair, which also depends on energy and momentum conversation.

Theoretically, the defect-assisted Auger process is expected to become significant as defect density increases, due to carrier scattering via defects [177]. As reported in Ref. [47], the rate of defect-assisted Auger is observed to be propositioned to n^3 in the low carrier density regime of thick InGaN/GaN QWs (4 nm). This relation suggests that the defect levels act as virtual scattering states (without carrier population build-up). On the other hand, as reported in Refs. [178, 179], a defect can also be an actual scattering center, which captures one particle and subsequently excites a second free particle during the process. Since the A coefficient contains information about the defect density and their capture cross section in average, the defect-assisted Auger process is supposed to be intrinsically linked to SRH recombination. To further examine this scenario, we thus assume the defect-assisted Auger rate can be expressed as:

$$Dn^2 = k_D \cdot An^2, \tag{5.12}$$

where k_D is a coefficient that depends on the interaction between the first particle captured
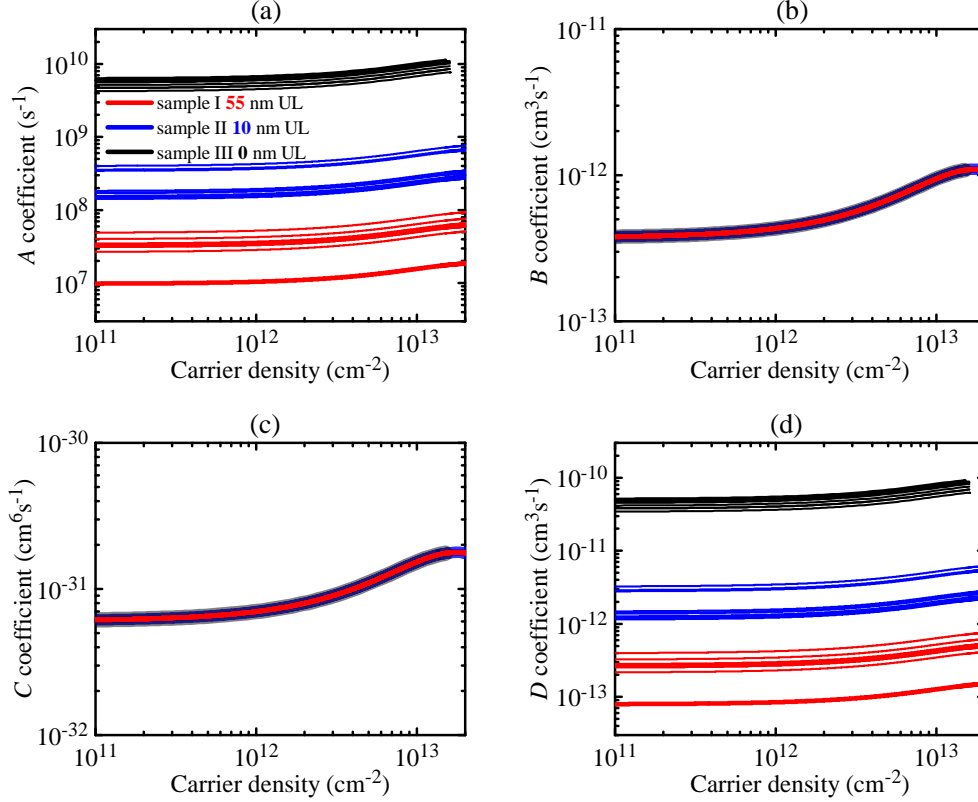
by the defects and the second free particle.

Figure 5.17 – (a-c) Carrier density dependent A, B, C and D coefficients extracted, in the frame work of the *ABCD* model, from the fitting of PL decays in the three sample at 19 μJ/cm^2, as shown in figure 5.15 (a-c).

We extracted the related coefficients by applying the model to simulate the PL decays at high fluence (19 μJ/cm^2). We first decomposed the SRH and radiative recombination channels in sample I by matching the PL decay at long delays and the derived ~ 20% maximum IQE [180]. The standard Auger coefficient can be subsequently determined by fitting the nonexponential decay at early delay. The radiative recombination has been kept identical for the three samples, considering that they share the same QW structure. The same is true for the standard Auger recombination. We noticed, for the more defective sample-II and -III, a discrepancy between the PL decays and the modeling when only the standard Auger recombination is considered, which can be reconciled by adding the defect-assisted Auger recombination term. As shown in figure 5.15(a-c), the pink dash-dotted lines illustrate the decay fits including only radiative recombination, labeled as *B*. The pink solid lines are the decays containing radiative and SRH recombinations, labeled as *AB*, which govern the PL decay at longer delays. The black dash-dotted curves represent the contributions of radiative, SRH and standard Auger recombinations, labeled as *ABC*. Apart from the *ABC* recombinations, the black curves are the fits taking into account the defect-assisted Auger channel, labeled as *ABCD*, which well reproduce the experiments. In sample III, the curves of *ABC* and *ABCD* almost overlap with each other, which suggests a marginal impact of defect-assisted Auger recombination. However, as the point defect density increases, the difference between the curves *ABC* and

ABCD become more and more obvious in sample-II and -III.

Figure 5.17 summarizes the density dependent coefficients by measuring at different positions in each sample. As illustrated in figure 5.17(a), the *A* coefficient is reduced by more than two orders of magnitude when switching from samples III to I, as the defect density in the QW is reduced by the increase of UL thickness. On the other hand, the *A* coefficient is marginally dependent on the carrier density, due to its weak dependence on QCSE with $osc^{0.35}$ in our samples. This can be related to the relatively thin QW we use. As shown in figure 5.17(b), the *B* coefficient remains constant at 4×10^{-13} cm^{3}s^{-1} below a carrier density of 5×10^{11} cm^{-2}, and then increases by a factor of two when reaching 10^{13} cm^{-2}. The lesser enhancement of the *B* term compared to the density dependent $\langle \Psi | \Psi \rangle^2$ is related to the phase-space filling effect in the degenerate regime. This leads to a reduction in the *B* coefficient because of the transition from bimolecular to monomolecular recombinations in the degenerate regime [181]. Meanwhile, the two joint effects also lead to a carrier density dependent *C* coefficient, which varies from 6×10^{-32} cm^6 s^{-1} to 2×10^{-31} cm^6 s^{-1} in the density range from 10^{11} cm^{-2} to 2×10^{13} cm^{-2}. Figure 5.17(d) reveals that the *D* coefficient varies from 10^{-13} cm^3 s^{-1} to 10^{-10} cm^{3}s^{-1} from samples I to III. In the end, in figure 5.18 we deduced a linear correlation between A and D as $D = k_D \cdot A$, with $k_D = 8 \times 10^{-21}$ cm^3. More importantly, the derived *D* value is in a similar range to the *B* coefficient, which indicates a closed competition between radiative and defect-assisted Auger processes. It is worth mentioning that the defect-assisted Auger process is supposed to be less sensitive to QCSE. It is because the two involved free particles have the same charge, i.e., either e-e or h-h pairs. Consequently, the defect-assisted Auger process is expected to be a critical carrier loss channel in green and red LEDs, in which the *B* coefficient is significantly reduced due to the QCSE.
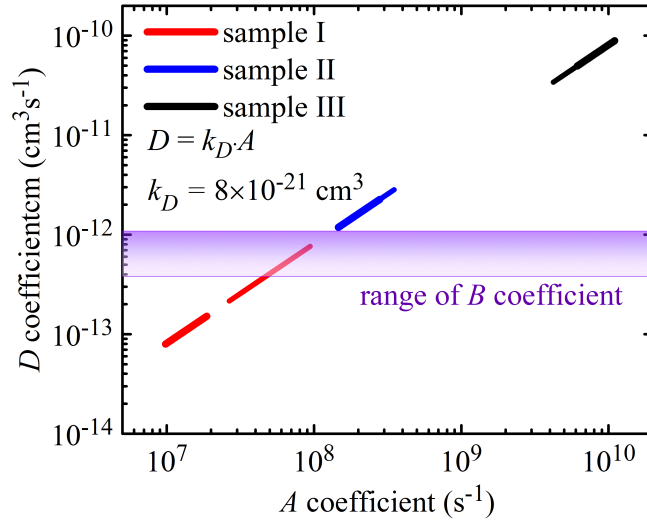

Figure 5.18 – Extracted linear correlation between A and D coefficients.

Based on the derived coefficients and the carrier density evolution during the PL decay, we further deduced the carrier density dependent IQE with and without the impact of defect-

assisted Auger recombination, as presented in figure 5.19 (a). It is well known that SRH and standard Auger recombination limit the IQE at low and high carrier densities, respectively. Comparatively, we observe that the reduction of IQE by the defect-assisted Auger process mainly occurs at the carrier density corresponding to the maximum IQE, which is around the operation condition for LEDs. To link the TR-PL results to LED devices, figure 5.19(b) displays the current density versus carrier density, assuming that there is no injection loss [182]. With the reduction of defect density, sample I exhibits a change of slope from 1, to 2, and then to 3, which corresponds to a progressive change in the dominant recombination process from SRH, to the combination of bimolecular and defect assisted Auger, and in the end to standard Auger. Due to the much larger defect density in sample III, the strong SRH recombination results in a slope 1 over a wide range of carrier density, even in the degenerate regime. On the other hand, as defect density reduces, the current density at maximum IQE reduces from nearly 100 kA/cm^2 to 10 A/cm^2 from sample III to I, as indicated by the colored dots in figure 5.19(b).
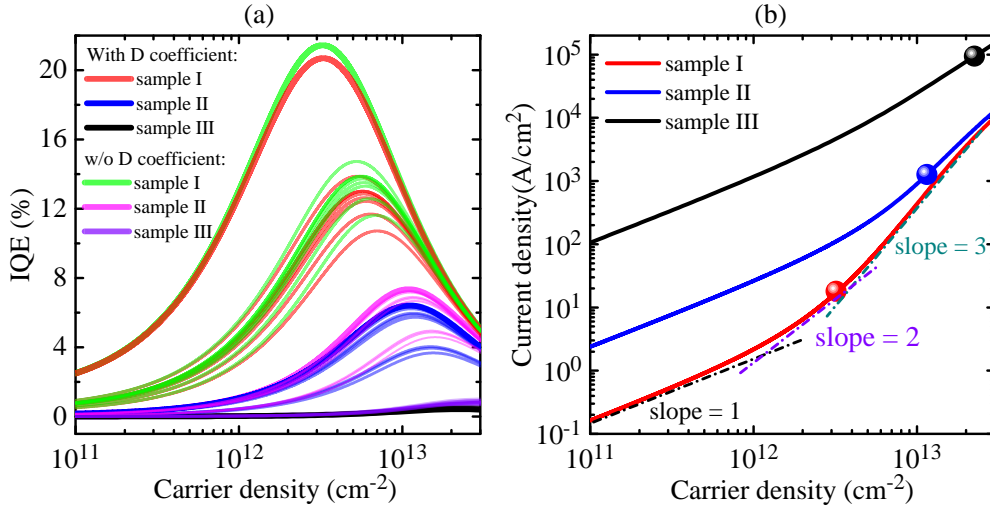
Figure 5.19 – (a) IQEs taken from different positions as a function of carrier density for the three samples. The red, blue and black curves represent the simulations taking the D coefficient into account for sample-I, -II, -III, respectively. Comparatively, the green, pink and purple curves are the cases without adding the D term. (b) Correlation between carrier density and derived current density for the three samples. The solid dots denote the condition of maximum IQE for each sample.

5.4 Conclusions

Experimental investigations of the efficiency droop in InGaN/GaN QWs under large optical excitation density clearly demonstrate that carrier localization strongly enhances the Auger recombination process in those QWs. We have shown that the relaxation of the k-selection rule in the Auger recombination process, resulting from carrier localization, can explain this enhancement. Hence, depending on the operating conditions, the disorder may be engineered to get either high IQE at low current density or low Auger recombination at higher currents. By comparing c-plane and m-plane QWs, we highlighted the increasing weight of the Auger recombination process by the internal electric field.

We study the impact of point defects on Auger recombination in c-plane InGaN/GaN QWs in the droop regime. The defect density in the active layer is tuned by varying the InALN UL thickness. By using high injection TR-PL measurements and modeling of the PL decays, we notice that, apart from the SRH and standard Auger recombination, additional carrier loss is necessary to reconciliate the discrepancy observed between the usual ABC model and experimental observations. We further introduce a defect-assisted Auger process, in which SRH-type defects can act as actual scattering centers. A linear dependence bewteen the SRH coefficient A and the defect-assisted Auger coefficient D is derived as $D = k_D \cdot A$, with $k_D = 8 \times 10^{-21}$ cm^3. Our results suggest that the increase of A from 10^7 s^{-1} to 10^{10} s^{-1} corresponds to D values in the range from 10^{-13} cm^3 s^{-1} to 10^{-10} cm^{3}s^{-1}, which is about equal to the bimolecular recombination coefficient B. It further suggests that the defect-assisted Auger recombination is expected to be a critical carrier loss mechanism in green and red LEDs, which suffer from a low B term due to the large QCSE. In addition, it would be worth further studying the impact of QW geometry and carrier density on the scattering mechanism at play in the defect-assisted Auger process.

6 Carrier recombination dynamics in InGaN/GaN core-shell microrods

6.1 Introductions

III-nitride microrods (MRs) have emerged as potential candidates for a variety of applications, such as micro-display, solid state lighting, on-chip communication, deep UV LEDs, and flexible devices [60, 61, 183, 184, 185, 186, 187, 188]. In particular, MRs-based micro-LEDs have received a large interest for micro-display, because of their insensitivity to the surface defects compared to the etched planar LEDs [60, 61]. On the other hand, MRs are expected to mitigate the efficiency droop of LEDs by reducing the carrier density, thanks to their nonpolar surface orientation, high surface-to-volume ratios, and absence of non-radiative extended defects [189, 190]. Nevertheless, the frequent presence of alloy and layer thickness gradients along the MR causes non-uniform current injection and poor control of color steering for white LEDs [70, 191, 192]. Additionally, catalyst-free growth can generate a gradient of the background electron concentration along the rod, which influences the carrier recombination rate [193, 194]. To improve the performance of InGaN/GaN core-shell MR LEDs, it is thus essential to understand the impacts of the inhomogeneities on carrier recombination dynamics.

In this chapter, we first take advantage of the picosecond TR-CL setup to probe the influence of the inhomogeneities in MRs on both radiative and SRH recombinations by recording simultaneously position dependent CL intensity and decay from 4 to 300 K. The major results of the present study includes: direct measurement of the radiative and non-radiative lifetime as a function of the temperature with a nanoscale resolution; revealing the relation between high indium content and higher point defect density (known as the green gap issue); demonstrate the short radiative lifetime of such MRs at room temperature, which is promising for pushing the onset of the efficiency droop to higher current densities and for fast visible light communication; confirm the great potential of core-shell MRs for lighting devices.

With the above understanding of nanoscopic optical properties, by using on high injection picosecond TR-PL setup, we further investigate the influence of inhomogeneities on Auger recombination, through the simultaneous recording of position dependent PL intensity and decay traces. The major results of the present study may be summarized as follows: evaluate precisely the radiative and Auger recombination coefficients under different degrees of InGaN alloy disorder along a single MR at 10 K, based on TR-PL experiment and theoretical modeling; confirm that Auger recombination is the dominant mechanism for the loss of efficiency

in the high injection regime, and reveal the close relation between efficiency droop and carrier localization; demonstrate that, despite the beneficial role of alloy fluctuations at low injection for InGaN LEDs based on MRs, the corresponding localization triggers fast Auger recombination at higher carrier densities.

6.2 Nanoscopic carrier dynamics in single InGaN/GaN core-shell microrod

6.2.1 Introduction

Here, we investigate highly efficient single InGaN/GaN core-shell MRs containing a single m-plane InGaN/GaN QW by TR-CL at nanometer scale. The influence of the inhomogeneities on both radiative and SRH recombinations is studied by recording simultaneously position dependent CL intensity (I_{cl}) and CL decay from 4 to 300 K [1, 70, 195].

6.2.2 Sample structures and optical properties

Organized InGaN/GaN core-shell MRs were grown by selective area MOCVD (provided by Osram) on an n-GaN/sapphire template [193]. First, a heavily n-doped ($\sim 10^{20}$ cm^{-3}) GaN core is grown vertically with a diameter of ~1.3 μm and a length of ~ 10 μm [194]. Then, an InGaN UL with an ~1% In-content is grown, which serves to improve the spatial resolution of CL by blocking the diffusion of the excited carrier from the core region to the active region [69] and may also improve the efficiency of the QW [4, 196]. The active region consists of a single InGaN QW in between two GaN barriers, with the inner barrier being n-type and the outer one being undoped. The outer barrier has ~6 nm thickness to protect the InGaN layer from any possible impacts of the surface [197], and the thickness of the inner barrier is about 60 nm. The In-content of the InGaN layer varies from around 11% to 13% and its width varies from about 6 to 13 nm from the bottom to top of the MR, respectively [198, 199]. A schematic of the core-shell MR structure is displayed in figure 6.1(a). Both CL and TR-CL measurements were performed under pulsed excitation conditions [1, 70, 195]. To investigate the influence of these inhomogeneities on the optical properties of the MR, we first perform CL mappings on single dispersed MRs. The CL measurements were carried out at 4 K and under 6 kV acceleration voltage. Figure 1(b) shows a plan view SE image of a MR detached from its original substrate and lying on a SiO$_2$ mask. Figure 6.1(c) reports a spectrally resolved I_{cl} line scan along the MR.

The prominent emission peak around 2.9 eV visible in figure 6.1(d) stems from the m-plane InGaN/GaN QW. From the bottom to the top of the rod, the peak energy of the QW decreases from 2.98 down to 2.80 eV and its FWHM increases from 170 to 210 meV (obtained through Gaussian fitting). These findings are in agreement with the observations of Müller *et al*. [198] in a similar series of samples by scanning transmission electron microscopy (STEM). It shows that the In-composition increases from around 11% to 13% and the well thickness from about 6 to 13 nm from the bottom to the top. The peak energy of the rod is consistent with that of planar m-plane InGaN/GaN QW having a similar In-content, which excludes the possible presence of the radial QCSE by pinning of the Fermi level in the surface of the sidewall [3, 197].
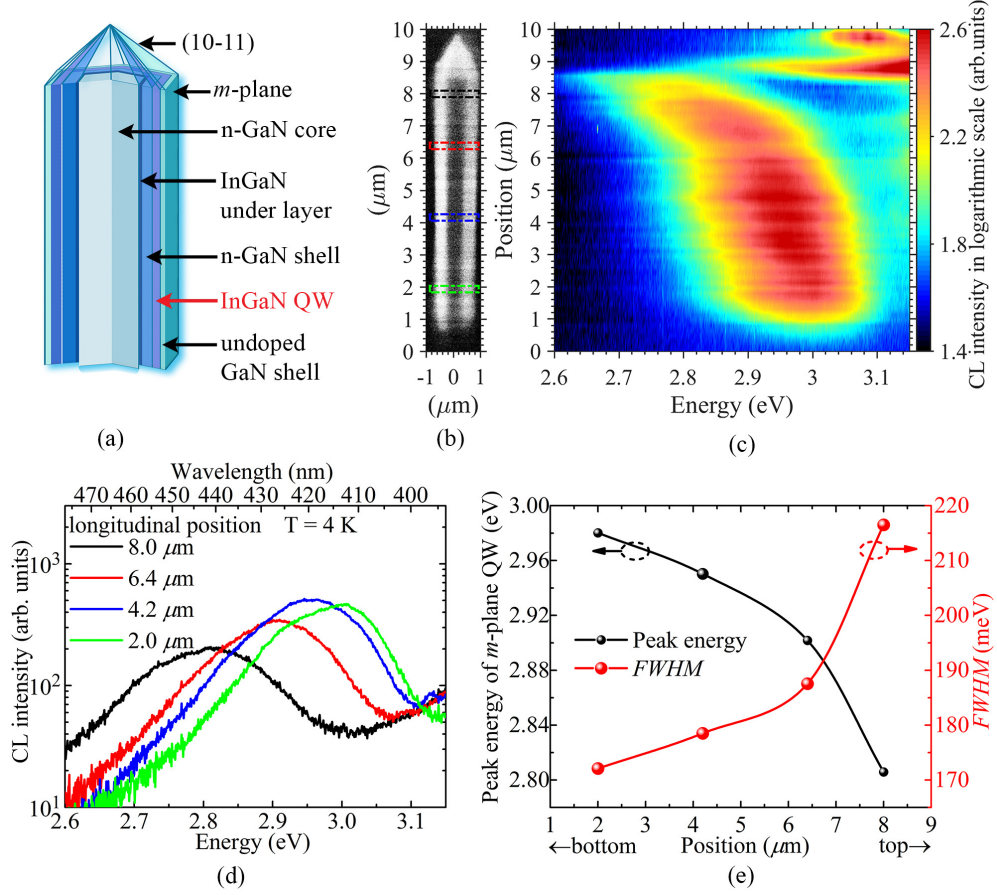
Figure 6.1 – (a) 3D profile of a core-shell microrod. (b) Plan view SE image of a detached rod lying on a SiO$_2$ mask. (c) Spectrally resolved CL intensity mapping along the rod (bottom to tip) under pulsed excitation and at 4 K. (d) Longitudinal position dependent CL spectra at the position marked by corresponding colored rectangles in (b). (e) Peak energies and FWHMs of QW emission as a function of position by Gaussian fitting from the spectra in (a).

Given the relatively large QW thickness, the variation of confinement energy is less sensitive to the change in the well thickness. Therefore, the In-gradient is the predominant factor for the position dependent redshift and broadening [198, 199]. Additionally, as shown in figure 6.1(e), the redshift is less steep between the bottom and middle than that near the top, and the same is true for the FWHM. This is attributed to a limited gas diffusion towards the base and a higher exposure to the gas-phase precursors near the top of MR during the growth and consequently to a stronger carrier localization through alloy disorder and possibly In-clusters near the top [193].

6.2.3 Temperature and spatially dependent TR-CL on single microrods

The carrier recombination dynamics in the QW determining quantum efficiency and carrier density at the operating condition is also expected to be influenced by the In-composition, well thickness, and background electron concentration n_0. We thus perform temperature

and position dependent TR-CL and CL simultaneously to investigate these impacts. Figure 6.2(a) shows the MR SE image and the corresponding two dimensional I_{cl} mapping of the QW emission within the spectral window (2.6 to 3.15 eV) at 4, 100, and 300 K. We only focus on the m-plane regions, between 1 and 8 μm in the longitudinal position, so as to exclude any impacts of the cleaved base or the semi-polar facet. The QW I_{cl} at 4 K appears with nearly the same intensity all over the m-plane region. figure 6.2(b) shows the longitudinal position dependent I_{cl} at 4 K (by averaging transversely), which is almost flat along the MR. In the meantime, the CL decay becomes longer from the bottom to the top as presented in figure 6.2(d). The positions where the decays are recorded in figure 6.2(d)-(f) are marked by the dots in the SE image of figure 6.2(a) with the corresponding colors.
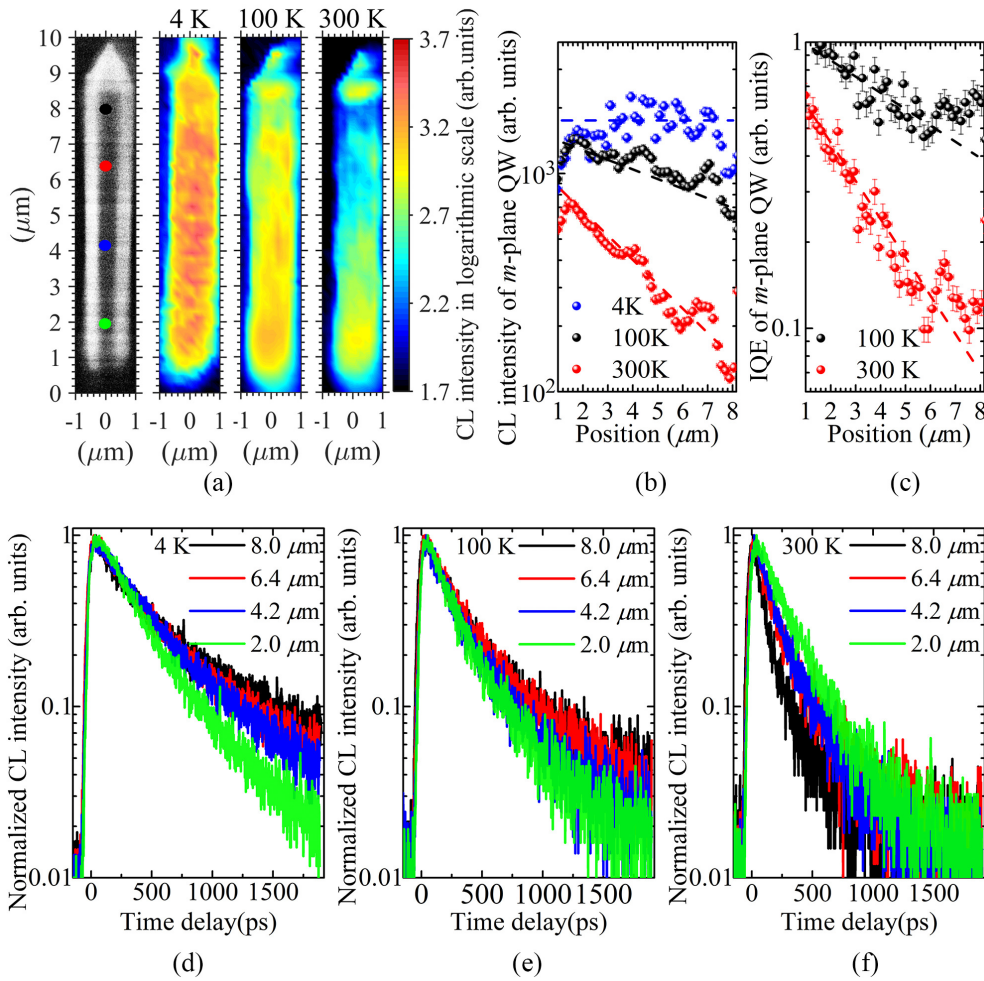
Figure 6.2 – (a) SE image of the rod and corresponding CL intensity mapping of QW emission, integrated within the spectral window from 2.6 to 3.15 eV, at 4, 100, and 300 K. (b) Longitudinal position dependent CL intensity distribution at 4, 100, and 300 K extracted from (a) by averaging transversely. The dashed lines are guides to the eye. (c) Extracted longitudinal position dependent IQE along the rod at 100 and 300 K. The dashed lines are guides to the eye. CL decays of QW emissions at the different positions along the rod at (d) 4, (e) 100, and (f) 300 K, respectively. The probing positions of the CL decays are marked in the SE image in (a) by the dots with the corresponding colors.

The nearly invariant I_{cl} as a function of position together with the change of decay time indicates two possibilities: either the carrier recombination in the QW throughout the rod is fully radiative or non-radiative lifetime (τ_{nr}) increases together with the radiative one (τ_r) keeping a constant ratio from the bottom to the top part of the rod. However, it is very unlikely that τ_{nr} would play a significant role at 4 K and show such an increasing trend. As shown in figure 6.2(e) and 6.2(f) at 100 and 300 K, the decay time and I_{cl} in figure 6.2(b) drop more around the top part of rod, which indicates that non-radiative recombination is more significant at elevated temperatures at this position. Would non-radiative recombination play a significant role at 4 K, one would expect a faster τ_{nr} at the top part, rather than a longer one. In addition, the non-radiative channel at 4 K is generally supposed to be blocked by the strong carrier localization evidenced through the CL linewidth larger than 100 meV and the few nanometer only diffusion length of carriers in the InGaN layer [70]. Therefore, the decay is dominated by the radiative recombination and the IQE is close to 100% at 4 K.

As outlined above, the CL decay at 4 K is dominated by the radiative recombination and reveals a variation along the rod. In detail, figure 6.3(a) shows the effective lifetime (τ_{eff}) at 4 K (purple dots) continuously increasing from ~300 to ~600 ps from the bottom to the top of MR. This trend of τ_{eff} can be mainly attributed to the stronger In-fluctuations in upper MR revealed by the STEM analysis on a similar series of rods, where In-rich clusters may have a few nanometer sizes and more than 18% of In compared to the average 13% [198]. Consequently, the strong alloy disorder results in local electric fields that cause the QCSE along the $\langle 0001 \rangle$ direction and may further induce uncorrelated lateral fluctuation of electron and hole wavefuctions [48].

When increasing temperature to 100 and 300 K, the I_{cl} of QW emission not only reduces due to the increase in SRH recombination but also presents more obvious contrast between bottom and top as illustrated in figure 6.2(a) and 6.2(b). Longitudinal dependent IQE at 100 and 300 K can be estimated by the ratio between the I_{cl} at 100 (300) K and 4 K, considering the negligible SRH recombination at 4 K. It turns out that the IQE at 100 K remains relatively high (between ~95% and ~50% from the bottom to the top), whereas the IQE at 300 K reduces more drastically from ~50% to ~10%, as shown in figure 6.2(c). Despite the fact that the electron beam excites carriers in both QW and barriers, it is consistent with the value reported by Mounir et al. on the similar MRs from the same batch, using below barrier optical excitation [199]. This is related to the following: (1) the presence of InGaN under the layer acts as a trap for both the excited carriers and background electrons in the GaN core, and only the carriers generated in the active region (within 80 nm of depth from the surface) contribute to the QW emission [69]; (2) an efficient carrier transfer, within the active region, from the barrier to the InGaN QW. This is guaranteed by the fact that the diffusion length in GaN is significantly longer than the barrier thicknesses in a wide range of temperatures, from 4 to 300 K [200, 201, 202]. figure 6.2(e) shows that the CL decay at 100 K is much faster at the bottom than that at the top of the MR, whereas figure 6.2 (f) shows the opposite trend for 300 K. To differentiate τ_r and τ_{nr} at 100 and 300 K in the QW, we use the following equations: $I_{cl} \propto \text{IQE} = \tau_{eff}/\tau_r$ and $\tau_{eff} = \left(\tau_{nr}^{-1} + \tau_r^{-1} \right)^{-1}$.

With the increase in temperature, the decrease in τ_{eff} is more pronounced near the top of the MR than near the bottom, as illustrated in figure 6.3(a). It suggests a higher density of point defects acting as non-radiative centers near the top of the MR, which annihilates the carriers during thermally activated diffusion [70]. The strong In-fluctuation and thick QW thickness
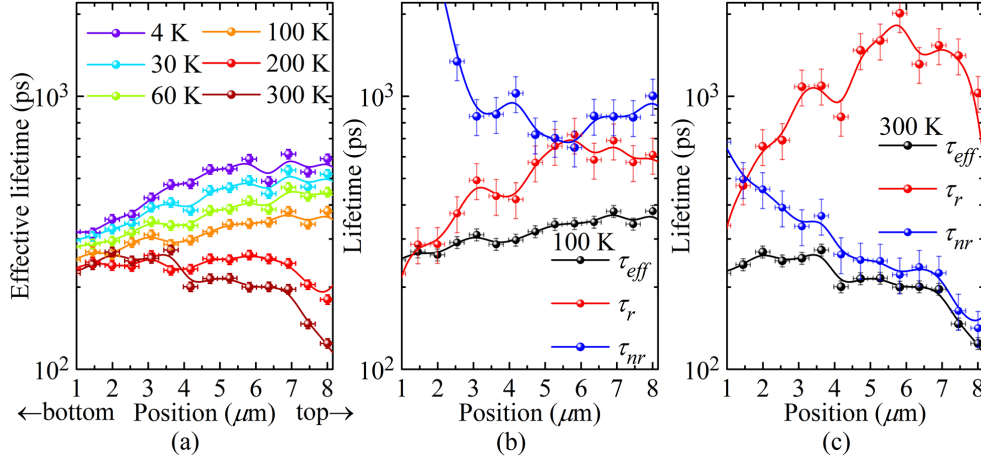
Figure 6.3 – (a) Longitudinal position dependent effective lifetime of QW luminescence along the rod from 4 to 300 K extracted by single exponential fitting of the CL decays. (b) and (c) Longitudinal position dependent effective lifetime, radiative and non-radia- tive lifetimes at (b) 100 and (c) 300 K.

in the upper part of MR may create a higher density of point defects around the vicinity of In-clusters [198, 203]. As displayed in figure 6.3(b), at 100 K, τ_{nr} around 1 ns is getting closer to τ_r in the upper part of the MR than that in the lower part. This competition drives the stronger decrease in τ_{eff} in the upper part of the MR. At 300 K, τ_{nr} decreases from ~500 to ~150 ps from the bottom to top, while τ_r increases from ~0.5 to ~1.5 ns, as shown in figure 6.3(c). The ensemble increase in τ_r at 300 K compared to that at 4 K indicates that the carriers start to delocalize from localization states to confinement states of QW [147]. However, τ_r remains below ~1.5 ns up to room temperature in the wide InGaN layer (6–13 nm). As a comparison, to maintain such a short τ_r for commercial blue LEDs, the well thickness of c-plane InGaN/GaN QWs is limited within 2–3 nm [204].

6.3 Auger recombination in single InGaN/GaN core-shell microrods

6.3.1 Introduction

Though InGaN/GaN core-shell MRs have received substantial attention for mitigating the efficiency droop [189, 183, 35], the MRs suffer from strong alloy disorder and interface roughness as demonstrated in the previous section 6.2 [205, 206]. Consequently, indirect Auger process is expected to be significant in such structure, as detailed in chapter 5 [3, 44, 46, 207]. Compared to planar active layers, it is much more demanding to investigate the carrier recombination dynamics in the droop regime of MRs due to their microscopic dimension. A proper analysis of the different contributions to carrier recombination, including SRH, radiative and Auger terms is also essential. Up to date, Auger recombination in single MRs has been studied by confocal pump-probe transmission method and electroluminescence of single MR devices [190, 208]. However, to our knowledge, the influence of the inhomogeneities on carrier dynamics of Auger processes in single MRs has not been reported yet. Here, relying on our high injection micro-TR-PL with 2 μm spatial resolution [140], we have explored the carrier dynamics at different positions along a single MR. In combination with a modified *ABC* model developed

previously [3], we are able to extract the excited carrier density, radiative and Auger recombination coefficients, and to evaluate the impact of the different degrees of inhomogeneities on Auger recombination along the MR.

6.3.2 Optical properties investigated by micro-PL

The experiments were carried out using the high injection micro-TR-PL setup, as explained in chapter 2. In order to simplify the analysis and neglect any contribution of SRH recombination all measurements in this work were carried out at 10 K [5]. To study the influence of the intrinsic inhomogeneities on the local optical properties, we first performed a micro-PL mapping along a single MR at low fluence (0.84 μJ/cm^2). Figure 6.4(b) shows the spatial dependence of the
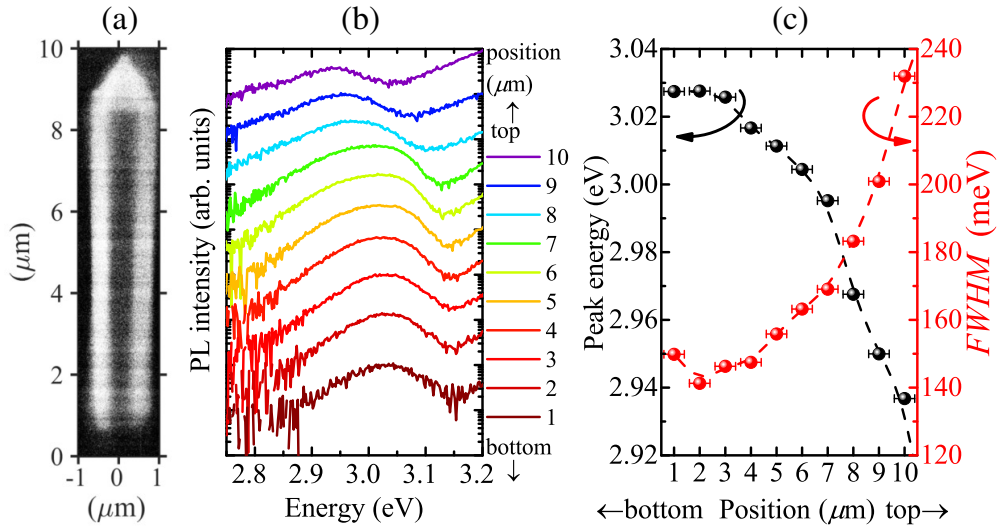

Figure 6.4 – (a) Plan view secondary electron image of a detached microrod lying on a Si/SiO$_2$ substrate; (b) One dimensional mapping of the time-integrated PL spectra of the m-plane InGaN QW from the bottom to top of the MR under low fluence 0.84 μJ/cm^2 measured at 10 K; (c) the corresponding spatial dependent peak energy (black dots) and *FWHM* (red dots) obtained by Gaussian fitting of the spectra shown in figure 6.4(b).

time-integrated PL spectra stemming from the m-plane QW from the bottom to the top of the MR. Figure 6.4(c) shows the corresponding spatially dependent peak energy and FWHM extracted by Gaussian fitting. Upon moving from the bottom to the top of the MR, we notice a redshift of the QW transition energy from 3.03 down to 2.94 eV together with an increase of the broadening from 140 up to 230 meV. This observation is consistent with the variation of the In content and the QW thickness along the MR as specified before. Given the relatively large QW thickness (> 6 nm), the confinement of carriers is predominantly influenced by the local change in the In content. Hence, the variation of the peak energy and the linewidth of the QW along the MR are a result of the In gradient and disorder.

To investigate the Auger-related carrier dynamics in the MR, we then performed fluence dependent micro-PL and TR-PL measurements at 10 K. We probed two positions along the MR with different degrees of disorder, characterized by different peak energy and linewidth. They
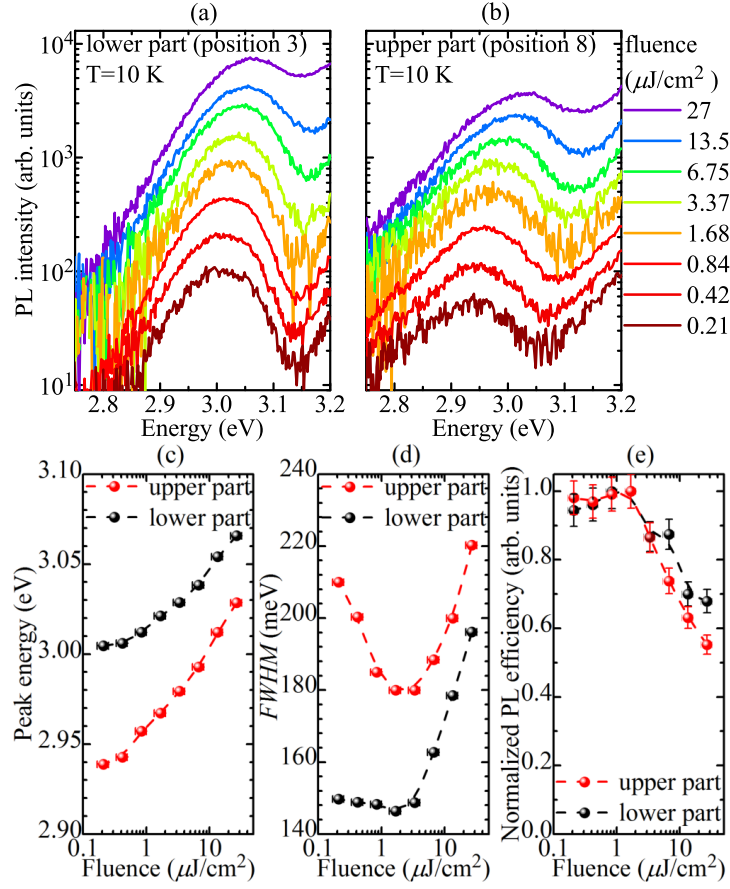
Figure 6.5 – Fluence dependent time-integrated PL spectra of the *m*-plane QW recorded in the lower and the upper part of the MR. (a) and (b) correspond to the probing position at 3 and 8 μm in figure 6.4, respectively. (c) and (d) the fluence dependent peak energy and *FWHM* of QW PL measured in the lower (black dots) and in the upper (red dots) part of the MR extracted by Gaussian fitting. (e) Derived PL efficiencies of the QW at the two recorded positions (normalized ratio between PL intensity and its corresponding fluence).

are used here as an evaluation for the strength of carrier localization [31]. Figure 6.5(a) and 6.5(b) present the fluence dependent time-integrated PL spectra of the *m*-plane QW probed at the lower and upper part of the MR, which correspond to the position at 3 and 8 μm shown in figure 6.4, respectively. Figure 6.5(c) and 6.5(d) show the comparison of the QW PL peak energy and the linewidth between the two positions. Data have been extracted by Gaussian fitting and illustrate in a qualitative manner the carrier-density dependent blue shift and simultaneous spectra broadening, due to varying In content and alloy disorder along the MR. In the upper part of the MR, the peak energy of the QW PL clearly blueshifts from 2.94 to 2.97 eV when the fluence rises from 0.21 to 1.68 μJ/cm^2. This goes together with a slight linewidth narrowing from 210 to 180 meV. These phenomena are different from the typical narrowing where enhanced scattering between carriers enhances relaxation down to lower localization states, resulting in a redshift of the PL spectrum [209, 210]. Alternatively, this behavior can be explained by the existence of an in-plane electric field along the <0001> direction induced

by In-rich clusters with a few nm size [206]. In other words, the screening of the field not only results in a blueshift, but also reduces the field-induced potential fluctuations [211, 212]. For the lower part of the MR, characterized with a lower In content, the blueshift (3.00-3.02 eV) and linewidth narrowing (150-146 meV) are less pronounced, which is in line with our interpretation. In addition, the fluence dependent spectrum evolution can be also related to the interplay between inhomogeneous broadening and the degenerate carrier statistics [136].

As the fluence increases to its maximum (27 μJ/cm^2), a clear blueshift as well as a broadening of the spectra at both positions hints the strong phase-space filling under high injection. The fluence dependent PL efficiency of the InGaN QW emission is then calculated as the ratio between the PL intensity and the corresponding fluence, referenced to the value obtained at low fluence, as shown in figure 6.5(e). For both positions, the efficiency shows a plateau at low injection and drops when the fluence increases up to 27 μJ/cm^2, evidencing the presence of the droop. Moreover, without anticipating the following TR-PL results, we can notice that the decrease of the relative efficiency is more pronounced in the upper part of the MR than in the lower one.

6.3.3 Carrier dynamics probed by micro-TR-PL and modeling

To gain more insight into carrier dynamics of the InGaN QW under high injection, we performed time-resolved studies. Figure 6.6 (a) and 6.6 (b) show the fluence dependent PL decays integrated over the full energy range of QW luminescence measured in the lower and in the upper part of the MR, respectively. At low fluence, below 0.84 μJ/cm^2, the two positions
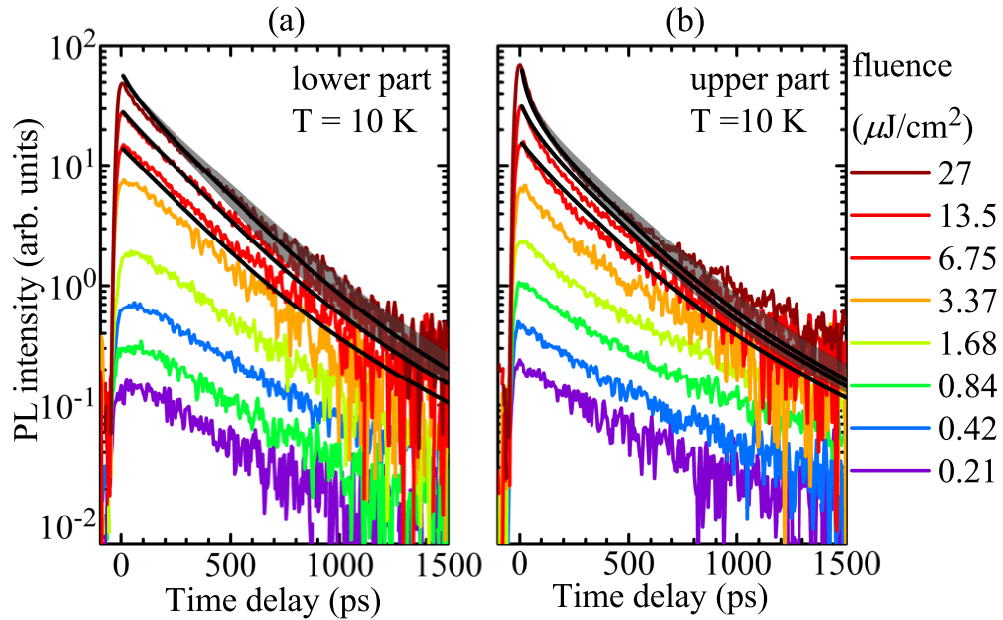

Figure 6.6 – (a) and (b) fluence dependent PL decays (color lines) of the m-plane QW measured in the lower and in the upper parts of the MR, and corresponding best fittings (black lines), and the tolerant ones (grey shaded zones) for the decay at 27 μJ/cm^2 based on a modified *ABC* model.

share a similar and invariant single exponential decay, which is consistent with the observed plateau of PL efficiency in figure 6.5(e) and suggests a dominant radiative recombination process. When the fluence goes beyond 6.75 μJ/cm^2, both series of decays exhibit a fast non-exponential trend at early delay. Note that, under high injection, phase-space filling results in a constant radiative lifetime evidenced by the linear increase of PL intensity at early delays [2, 213, 214]. Additionally, even if SRH recombination was present, its saturation at high carrier density would contribute to a longer decay, not a shorter one [2, 3]. Consequently, the observed non-exponential decay strongly indicates the emergence of Auger recombination.

Figure 6.7(a) and 6.7(b) illustrate the time-dependent evolutions of the spectra of the *m*-plane QW at the two recorded positions. At early delay ($t = 0$), the spectra at both positions reveal a pronounced broadening of the QW PL induced by the high carrier density. At longer decay, both series of spectra show a noticeable redshift, which can be attributed to the carrier relaxation from shallow localization states to deeper ones and to the descreening of the in-plane field along the <0001> direction [140]. Moreover, it is apparent that the time-dependent
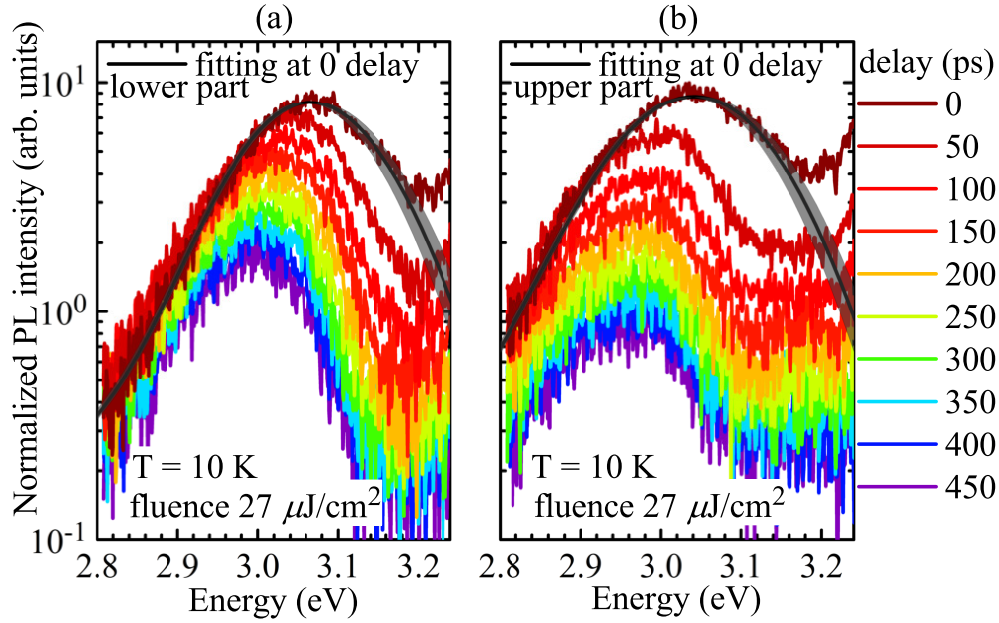
Figure 6.7 – (a) and (b) time-dependent InGaN spectra evolution (from 0 to 450 ps) of the *m*-plane QW measured in the lower and in the upper part of the MR under high injection (27 μJ/cm^2) at 10 K, and corresponding tolerant (grey shaded zones) and best (black lines) fittings of the spectra at early delay ($t = 0$) based on Fermi's golden rule.

PL intensity for the upper part of the MR drops much faster than that in the lower part, which suggests a stronger Auger recombination in the former case.

In order to quantify the coefficient of Auger recombination from TR-PL results, we use a modified *ABC* model [130, 3]:

$$\frac{dn}{dt} = -\int_{E_{QW}}^{\infty} R_{sp}(n,E)dE - \frac{C}{2}((n+n_0)^2 n + (n+n_0)n^2),\tag{6.1}$$

where n, n_0, and C denote the non-equilibrium carrier density, the electron background concentration, and the Auger recombination coefficient, respectively. R_{sp} is the spontaneous radiative rate, which can be expressed as:

$$R_{sp}(n, E) = \sum_{j=A,B} \frac{1}{\tau_0} D(E)_j^{cv} f(n, E)_{e,j} f(n, E)_{h,j}, \tag{6.2}$$

where τ_0 is the average transition lifetime, which depends on the oscillator strength, $D(E)$ is the 2D joint density of states. $f_{e,j}$, $f_{h,j}$ are the electron and hole Fermi-Dirac distribution, with the subscript indicating the transitions from the conduction to the A and B valence bands. The consideration of those two transitions is referred to the report that they are the dominant components measured in polarization-resolved PL spectra when carrier density reaches the degenerate regime [136]. In the last term of Eq. 6.1, the prefactor 1/2 is used to allow for a comparison with the standard *ABC* model by assuming an equal contribution between electron-electron-hole and electron-hole-hole Auger processes [44]. SRH recombination is neglected as mentioned before. The radiative lifetime τ_r, Auger lifetime τ_{Aug}, and the effective lifetime τ_{eff} at early delay can then be obtained via:

$$\tau_r = \frac{n}{\int_{E_{QW}}^{\infty} R_{sp}(n, E) dE}, \tag{6.3}$$

$$\tau_{Aug} = \frac{2}{C[(n+n_0)^2 + (n+n_0)n]}, \tag{6.4}$$

$$\tau_{eff} = (\tau_r^{-1} + \tau_{Aug}^{-1})^{-1}. \tag{6.5}$$

The fitting parameters include n at $t = 0$, n_0, τ_0 and C, which are determined as follows. First, the initial n at 27 μJ/cm^2 is extracted through a fit of the spectral shape at $t = 0$, using Eq. 6.2 convoluted with a Gaussian profile reproducing the inhomogeneous linewidth [3, 140]. The linewidth is taken at a moderate excitation flux of 3.37 μJ/cm^2, corresponding to the minimum value in figure 6.5 (d). The results of such best fits and tolerant fits dependent on the uncertainties of n are displayed in figure 6.7. At low excitation density values, the corresponding initial n at each fluence can be derived assuming a linearity between the laser fluence and the initial carrier density. Then, τ_0, n_0 and C, summarized in Table 6.1, serve to fit simultaneously the PL decay and the initial PL intensity $I_{pl}(t = 0)$ in figure 6.6, and the experimental effective lifetimes τ_{eff} in figure 6.8. Specifically, τ_{eff} denotes the effective carrier lifetime for each fluence and is obtained by fitting the initial decay by a single exponential.

The modeling reveals that the C coefficient shows a variation by about a factor of 4 between the upper and the lower part of the MR with values of 2.2$\pm$0.9 and 0.5$\pm$0.2 $\times 10^{-16}$ cm^{4}s^{-1}, respectively. The estimated value in 3D units amounts to 2.7$\pm$2.0 $\times 10^{-28}$ and 1.8$\pm$1.0 $\times 10^{-29}$ cm^{6}s^{-1}, respectively, by using ~11 and 6 nm QW thickness at the two positions of the MR

[206]. On the other hand, the B coefficient can be estimated by $1/[(n_0 + n)\tau_r]$ and has similar values at both positions, around $1.1\pm0.2 \times 10^{-2}$ cm^{2}s^{-1} at low carrier density ($\sim 10^{11}$ cm^{-2}), which corresponds to 1.21 ± 0.44 and $0.66\pm0.18 \times 10^{-8}$ cm^{3}s^{-1} in 3D units. These extracted coefficients are consistent with our previous report about planar m-plane QW with strong alloy disorder at 4 K [3].

Table 6.1 – Summaries of predominant parameters for fitting and the experimental linewidths

position	n ($\times 10^{12}$ cm^{-2})	τ_0 ($\times 10^{-6}$ s)	C ($\times 10^{-16}$ cm^{4}s^{-1})	$FWHM$ (meV)	n_0 ($\times 10^{11}$ cm^{-2})
upper	9.5 ± 1.0	5.1 ± 0.5	2.2 ∓ 0.9	180 ± 10	1.0 ± 0.3
lower	8.5 ± 1.0	5.0 ± 0.5	0.5 ∓ 0.2	148 ± 10	1.0 ± 0.3
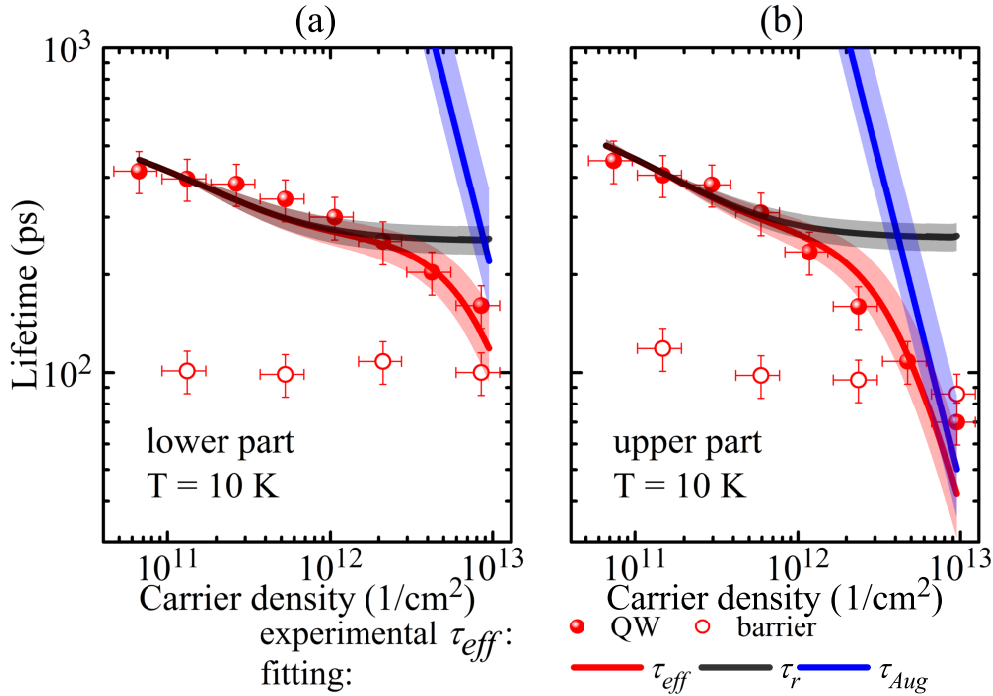
Figure 6.8 – (a) and (b) experimental effective PL lifetime τ_{eff} in the InGaN QW (solid dots) and the GaN barrier (hollow circles) as a function of carrier density measured in the lower and in the upper part of the MR, extracted from a single exponential decay in figure 6.6, and corresponding tolerant (shaded zones) and best (solid lines) theoretical estimations of τ_{eff} (red), radiative lifetime τ_r (black) and Auger one τ_{Aug} (blue).

Finally, figure 6.8 compares the changes of τ_{eff} of the InGaN QW in the lower and in the upper parts of the MR as a function of the injected carrier density. At low carrier density ($\sim 10^{11}$ cm^{-2}), τ_{eff} shows similar values for both positions ($\sim$400 ps). The slightly longer τ_{eff} observed at the top of the MR can be ascribed to the lower electron background concentration n_0 as listed in Table 6.1 [215]. By contrast, at maximum carrier density, τ_{eff} varies significantly between the upper and the lower part of the rod, with values of 70 and 160 ps, respectively. In addition, the τ_{eff} of the barrier exhibited in figure 6.8 is as short as $\sim$100 ps, which suggests an efficient carrier transfer to the InGaN QW and no dependence on the actual position along

the MR. These observations lead us to the conclusion that the decrease of τ_{eff} under high injection is mainly governed by Auger recombination. Moreover, based on the distinct drop in PL efficiency together with the shorter τ_{eff} in the InGaN QW closer to the top of the MR, the stronger Auger recombination is likely related to the inhomogeneous linewidth and thus to the disorder landscape. These observations are in agreement with the outcome of previous studies on planar m-plane samples [3, 46, 44, 207]. Using Eqs. 6.3 and 6.4 enables us to distinguish between the contribution of τ_r and τ_{Aug} to the carrier recombination dynamics, as shown in figure 6.8. As the QW carrier density increases from 10^{11} to 10^{12} cm^{-2}, τ_r governs the evolution of τ_{eff}, and decreases continuously from ~400 to ~300 ps. When n is near 10^{13} cm^{-2}, τ_r is expected to be constant and equal to ~260 ps, due to phase-space filling [2, 213, 214], and the corresponding internal quantum efficiency in the lower and upper part of MR is about 62% and 27%, respectively, given by τ_{eff}/τ_r. Meanwhile, τ_{Aug} dramatically drops and become shorter than τ_r when n is approaching to 10^{13} cm^{-2}. Interestingly, we observe that the τ_{Aug} is 4 times shorter under high injection in the upper part of the MR compared to the lower one. Therefore, considering the similar τ_r value in the two positions, it suggests that stronger Auger recombination takes place in the upper part. This can be understood by taking into account the stronger alloy disorder in this region as characterized by the larger PL linewidth and In content.

6.4 Conclusions

We studied the carrier recombination dynamics at nanometer scale in a single InGaN/GaN core-shell MR by TR-CL. Our results reveal a position dependent redshift of QW emission that is mainly due to the In-content gradient. At 300 K, the drop of the internal quantum efficiency of QW emission from 50% at the bottom to 10% at the top of the rod is related to a change of the effective lifetime from 240 to 120 ps. The correspondent non-radiative SRH lifetime decreases from 500 to 150 ps from the bottom to the top. We attribute this to the increased In-content in the upper part of MR causing a higher density of point defects. However, the QW with a thick InGaN layer (>6 nm) achieves short radiative lifetime faster than ~1.5 ns up to room temperature, which is promising for pushing the onset of the efficiency droop to higher current densities.

By using micro-TR-PL at 10 K, we study the local carrier recombination dynamics in a single dispersed core-shell MR with an m-plane InGaN/GaN QW. The impact of InGaN alloy disorder on the carrier dynamics is quantified by a modified *ABC* model. At low carrier density, the carrier recombination is dominated by radiative processes and the recorded decay times along the MR equally amount to about 400 ps, corresponding to a *B* coefficient of $1.1\pm0.2 \times 10^{-2}$ cm^{2}s^{-1}. As a comparison, at high carrier density ($> 10^{12}$ cm^{-2}), the efficiency and decay time of PL in the QW drop significantly, which indicates the onset of Auger recombination. The extracted *C* coefficient near the top part of the MR is about 4 times larger than that at the base, which is manifested by values of 2.2 ± 0.9 and $0.5\pm0.2 \times 10^{-16}$ cm^{4}s^{-1}, respectively. This is related to a different degree of alloy disorder in the two probed positions, with ~180 and 150 meV inhomogeneous linewidth, respectively. Relaxation of k-selection rule by alloy disorder is expected to play an important role in the increase of Auger coefficient. Therefore, our results confirm that Auger recombination is sensitive to alloy disorder and can be significantly enhanced when this type of disorder is prominent. Our results suggest that it is crucial to

minimize the degree of disorder in the active layer for high power LEDs based on core-shell MRs.

7 Summaries and prospective

In conclusion, we investigate the ultrafast carrier dynamics in III-nitride nanostructures related to the quantum efficiency of LEDs. The major results of this thesis are summarized as follows:

(1) Address the impact of dislocations and point defects on the efficiency of LEDs. By using TR-CL with nanometer and picosecond resolutions, we characterize the exciton dynamics around a single dislocation in bulk GaN at 10 K. By recording and modeling variations of CL decays across an isolated dislocation, we deduce the exciton diffusion length as well as an effective area of the dislocation, where the recombination can be regarded as entirely non-radiative. The edge-component of dislocation is determined by observing dipole-like energy shifts of exciton and the modeling of local strain field distribution. We further unveil that indium atoms in the InGaN and InAlN ULs play an essential role in capturing preexisting point defects segregating at the GaN surface. The significant suppression of the point defect density by UL contributes to the radiative-dominated carrier recombinations, as evidenced by the increase of the decay time from 10 to 300 K by TR-PL. By using 1-kV CL, we demonstrate the nanoscopic features of SRH recombination by point defects and the evolution of the carrier diffusion as a function of defect densities.

(2) Obtain a comprehensive picture about the origin of radiative recombinations and the interplay between excitons and e-h plasma in m-plane InGaN/GaN QWs. By using TR-PL and modeling with Fermi's golden rule and the first order correlated Saha's equation, we decompose the radiative recombination channel into an excitonic and an e-h pair contribution. Contrary to the standard electron-hole picture, our results confirm that excitons can be important portion in the total photoexcited carriers. With an accurate determinations of carrier-density-dependent SRH and bimolecular coefficients in the Mott transition region, our approach provides a way to evaluate the impact of Auger recombination.

(3) Investigate the influence of carrier scattering on indirect Auger processes in InGaN/GaN QW. We demonstrate that carrier localization strongly intensifies the Auger recombination in nonpolar InGaN/GaN QWs. The relaxation of the k-selection rule during the Auger process, resulting from alloy disorder, can account for the increase of the efficiency droop in the QWs. Moreover, we develop a model to accurately predict the initial carrier density and Auger recombination coefficients based on a high injection TR-PL approach. We further study the

impact of point defects on Auger recombination in InGaN/GaN QW in the droop regime. By tuning the defect density in QWs through UL, TR-PL results reveal a defect-assisted Auger process. Modeling of PL decays indicate a linear dependence between SRH and defect-assisted Auger recombination, which suggests that SRH-type defects can be efficient scattering centers for Auger recombination.

(4) We study the optical properties of sidewall m-plane InGaN/GaN QW in single core-shell microwires. Probing the temperature dependent CL decays along the rod enables us to decompose radiative and non-radiative lifetimes. At 300 K, non-radiative lifetimes decreases from 500 ps at the bottom of the rod to 150 ps at its top. This variation results from an increased In-content in the upper part of the rod that causes a higher density of point defects. However, the radiative lifetime remains below 1.5 ns up to room temperature even with a thick active layer. High injection TR-PL is subsequently employed to study the impact of the intrinsic homogeneities of microwires on the Auger recombination at 10 K. Our study evidences a variation of Auger recombination along the length of the rod, which corresponds to the change of PL linewidth. These results confirm that Auger recombination is sensitive to alloy disorder and can be significantly enhanced when this type of disorder is prominent.

Based on the results of these studies, certain topics and open questions are worth being further investigated:

(1) Even though it is admitted that the core of dislocation is at the atomic scale, our results clearly demonstrate that its impact on non-radiative recombination occurs up to the nanoscale. Apart from carrier diffusion, other possible mechanisms should be addressed, such as decoration of such dislocations by point defects or impurities, exciton dissociation around dislocation. It is worth further studying the interplay between dislocation, point defect in InGaN/GaN QW. The local strain variation of dislocation is expected to modulate the distribution of indium and point defect, which may increase the effective area of individual dislocation. As long as the mean distance of effective area of dislocation reaches the diffusion length of carrier, it may has impact on quantum efficiency. In addition, if the point defect can be significantly reduced, the long radiative lifetime of carrier in geen and red LEDs due to the strong QCSE may increase the diffusion length of carriers. It is meaningful to examine to which extent the dislocation remains to be insignificant to the quantum efficiency.

(2) Based on the observed nanoscopic CL features of SRH recombination, by further probing CL decays around defective region by TR-CL, it is possible to evaluate the capture cross section of defect or defect aggregates. Moreover, it is worth studying the efficacy of ULs on AlGaN/AlN QW for UV LEDs and high In-content InGaN/GaN QWs for green-red LEDs. In particular, InAlN can be a promising candidate, considering its advantages of UV transparency and lattice matching for ameliorating strain-related issues. Additionally, it is important to investigate the formation mechanism of the defect during growth, which can be related to the surface properties, such as polarity, atom arrangement and Fermi-level pinning. It can give more insights by comparing the defect trapping mechanism of UL grown on c-plane and m-plane substrates. It is valuable to further determine the type of defect, which may require comprehensive analysis based on positron annihilation spectroscopy, TR-PL measurement and tuning growth conditions.

(3) Carrier localization reveals subtle impacts on carrier recombination dynamics, certain

questions remains to be addressed. For instance, whether or not localization is as strong under low carrier density as in degenerate regime. One would expect a less degree of localization (in average) in the later case, considering the delocalized characteristic of excited states. Besides, joint effect of electric field and interface roughness can be another factor that increases carrier localization in c-plane QWs. Screening (or partially) the field by degenerate carrier contributes to less localization. Moreover, the interplay between localization and Coulomb interaction may play a significant role on extonic effect, considering their similar scale of energy and distance.

(4) To mitigate the carrier localization enhanced Auger recombination, one option is to reduce indium content in the QW. However, as localization is weaken, carriers are expected to be more sensitive to defect, the density of defect has to be reduced. On the other hand, using different misorientation and facet of substrate can be extra dimensions to tailor the alloy disorder. On the other hand, achieving sharp interface of QW is supposed to be important for further reducing localization in the QW with large electric field and width. As to the defect-assisted Auger, it is still an open question whether the defects act as actual or virtual scattering centers.

(5)Though the core-shell microwires with thick m-plane QW provide high radiative rate, more analyses are required to evaluate the impact of inhomogeneities on LEDs based on this structure. At current stage, strong inhomogeneties in core-shell microwires can be a major issue for their application in high power LEDs. However, their unique 3D geometric properties, comparing to planar structures, suggest promising potential for micro-LEDs operating at moderate current.

As a result, this thesis demonstrates insightful physics about carrier recombination dynamics in III-nitride nanostructures, which is expected to further improving the quantum efficiency and overcoming the bottleneck of III-nitride LEDs.

Bibliography

[1] W. Liu, J.-F. Carlin, N. Grandjean, B. Deveaud, and G. Jacopin, "Exciton dynamics at a single dislocation in GaN probed by picosecond time-resolved cathodoluminescence", Applied Physics Letters **109**, 042101 (2016).

[2] W. Liu, R. Butté, A. Dussaigne, N. Grandjean, B. Deveaud, and G. Jacopin, "Carrier-density-dependent recombination dynamics of excitons and electron-hole plasma in m-plane InGaN/GaN quantum wells", Physical Review B **94**, 195411 (2016).

[3] M. Shahmohammadi, W. Liu, G. Rossbach, L. Lahourcade, A. Dussaigne, C. Bougerol, R. Butté, N. Grandjean, B. Deveaud, and G. Jacopin, "Enhancement of Auger recombination induced by carrier localization in InGaN/GaN quantum wells", Physical Review B **95**, 125314 (2017).

[4] C. Haller, J.-F. Carlin, G. Jacopin, W. Liu, D. Martin, R. Butté, and N. Grandjean, "GaN surface as the source of non-radiative defects in InGaN/GaN quantum wells", Applied Physics Letters **113**, 111106 (2018).

[5] W. Liu, C. Mounir, G. Rossbach, T. Schimpke, A. Avramescu, H.-J. Lugauer, M. Strassburg, U. Schwarz, B. Deveaud, and G. Jacopin, "Spatially dependent carrier dynamics in single InGaN/GaN core-shell microrod by time-resolved cathodoluminescence", Applied Physics Letters **112**, 052106 (2018).

[6] L. C. de Carvalho, A. Schleife, and F. Bechstedt, "Influence of exchange and correlation on structural and electronic properties of AlN, GaN, and InN polytypes", Physical Review B **84**, 195105 (2011).

[7] M. Kumagai, S. Chuang, and H. Ando, "Analytical solutions of the block-diagonalized Hamiltonian for strained wurtzite semiconductors", Physical Review B **57**, 15303 (1998).

[8] E. I. Rashba, "Properties of semiconductors with an extremum loop. I. Cyclotron and combinational resonance in a magnetic field perpendicular to the plane of the loop", Soviet Physics, Solid State **2**, 1109–1122 (1960).

[9] B. Gil, O. Briot, and R.-L. Aulombard, "Valence-band physics and the optical properties of GaN epilayers grown onto sapphire with wurtzite symmetry", Physical Review B **52**, R17028(R) (1995).

[10] M. Feneberg, R. A. Leute, B. Neuschl, K. Thonke, and M. Bickermann, "High-excitation and high-resolution photoluminescence spectra of bulk AlN", Physical Review B **82**, 075208 (2010).

Bibliography

[11] J. Wu, W. Walukiewicz, K. Yu, J. Ager Iii, E. Haller, H. Lu, W. J. Schaff, Y. Saito, and Y. Nanishi, "Unusual properties of the fundamental band gap of InN", Applied Physics Letters **80**, 3967–3969 (2002).

[12] Y. P. Varshni, "Temperature dependence of the energy gap in semiconductors", Physica **34**, 149–154 (1967).

[13] V. Fiorentini, F. Bernardini, and O. Ambacher, "Evidence for nonlinear macroscopic polarization in III–V nitride alloy heterostructures", Applied Physics Letters **80**, 1204–1206 (2002).

[14] F. Bernardini and V. Fiorentini, "Spontaneous versus piezoelectric polarization in III–V nitrides: conceptual aspects and practical consequences", physica status solidi (b) **216**, 391–398 (1999).

[15] N. Grandjean, B. Damilano, S. Dalmasso, M. Leroux, M. Laügt, and J. Massies, "Built-in electric-field effects in wurtzite AlGaN/GaN quantum wells", Journal of applied physics **86**, 3714–3720 (1999).

[16] G. Rossbach, High-Density Excitonic Effects in GaN : Mott-Transition and Polariton Lasing PAR, PhD thesis, EPF (2014).

[17] C. Weisbuch and B. Vinter, Quantum semiconductor structures: fundamentals and applications, Elsevier (2014).

[18] R. Leavitt and J. Little, "Simple method for calculating exciton binding energies in quantum-confined semiconductor structures", Physical Review B **42**, 11774 (1990).

[19] N. Mott, "The transition to the metallic state", Philosophical Magazine **6**, 287–309 (1961).

[20] A. Kavokin, J. Baumberg, G. Malpuech, and F. Laussy, Microcavities, Oxford University Press (2007).

[21] E. Hanamura and H. Haug, "Condensation effects of excitons", Physics Reports **33**, 209–284 (1977).

[22] N. Mott, "Metal-Insulator Transition", Rev. Mod. Phys. **40**, 677–683 (1968).

[23] D. Guerci, M. Capone, and M. Fabrizio, "Exciton Mott transition revisited", Phys. Rev. Materials **3**, 054605 (2019).

[24] A. Almand-Hunter, H. Li, S. Cundiff, M. Mootz, M. Kira, and S. W. Koch, "Quantum droplets of electrons and holes", Nature **506**, 471 (2014).

[25] X.-F. He, "Excitons in anisotropic solids: The model of fractional-dimensional space", Physical Review B **43**, 2063 (1991).

[26] C. Klingshirn, R. Hauschild, J. Fallert, and H. Kalt, "Room-temperature stimulated emission of ZnO: Alternatives to excitonic lasing", Phys. Rev. B **75**, 115203 (2007).

[27] T. Nagai, A. Yamamoto, and Y. Kanemitsu, "Photoluminescence dynamics of GaN under intense band-to-band and exciton resonant excitation", Phys. Rev. B **71**, 121201 (2005).

[28] Y.-R. Wu, R. Shivaraman, K.-C. Wang, and J. S. Speck, "Analyzing the physical properties of InGaN multiple quantum well light emitting diodes from nano scale structure", Applied Physics Letters **101**, 083505 (2012).

[29] M. Filoche, M. Piccardo, Y.-R. Wu, C.-K. Li, C. Weisbuch, and S. Mayboroda, "Localization landscape theory of disorder in semiconductors. I. Theory and modeling", Physical Review B **95**, 144204 (2017).

[30] C.-K. Li, M. Piccardo, L.-S. Lu, S. Mayboroda, L. Martinelli, J. Peretti, J. S. Speck, C. Weisbuch, M. Filoche, and Y.-R. Wu, "Localization landscape theory of disorder in semiconductors. III. Application to carrier transport and recombination in light emitting diodes", Physical Review B **95**, 144206 (2017).

[31] M. Piccardo, C.-K. Li, Y.-R. Wu, J. S. Speck, B. Bonef, R. M. Farrell, M. Filoche, L. Martinelli, J. Peretti, and C. Weisbuch, "Localization landscape theory of disorder in semiconductors. II. Urbach tails of disordered quantum well layers", Physical Review B **95**, 144205 (2017).

[32] L. Mancini, N. Amirifar, D. Shinde, I. Blum, M. Gilbert, A. Vella, F. Vurpillot, W. Lefebvre, R. Lardé, E. Talbot, *et al.*, "Composition of wide bandgap semiconductor materials and nanostructures measured by atom probe tomography and its dependence on the surface electric field", The Journal of Physical Chemistry C **118**, 24136–24151 (2014).

[33] J. Wu, W. Walukiewicz, W. Shan, K. Yu, J. Ager Iii, S. Li, E. Haller, H. Lu, and W. J. Schaff, "Temperature dependence of the fundamental band gap of InN", Journal of Applied Physics **94**, 4457–4460 (2003).

[34] T. Makimoto, K. Kumarkura, T. Nishida, and N. Kobayashi, "Valence-band discontinuities between InGaN and GaN evaluated by capacitance-voltage characteristics of p-InGaN/n-GaN diodes", Journal of electronic materials **31**, 313–315 (2002).

[35] C. Weisbuch, M. Piccardo, L. Martinelli, J. Iveland, J. Peretti, and J. S. Speck, "The efficiency challenge of nitride light-emitting diodes for lighting", physica status solidi (a) **212**, 899–913 (2015).

[36] P. M. Pattison, M. Hansen, and J. Y. Tsao, "LED lighting efficacy: status and directions", Comptes Rendus Physique **19**, 134–145 (2018).

[37] S. Matthias, "Innovations in LED lighting", DOE SSL Workshop, Nashville (2018).

[38] A. Laubsch, M. Sabathil, W. Bergbauer, M. Strassburg, H. Lugauer, M. Peter, S. Lutgen, N. Linder, K. Streubel, J. Hader, J. V. Moloney, B. Pasenow, and S. W. Koch, "On the origin of IQE-'droop' in InGaN LEDs", physica status solidi c **6**, S913–S916 (2009).

[39] A. David and N. F. Gardner, "Droop in III-nitrides: Comparison of bulk and injection contributions", Applied Physics Letters **97**, 193508 (2010).

[40] C. Sheng Xia, Z. M. Simon Li, and Y. Sheng, "On the importance of AlGaN electron blocking layer design for GaN-based light-emitting diodes", Applied Physics Letters **103**, 233505 (2013).

[41] J. Hader, J. V. Moloney, and S. W. Koch, "Density-activated defect recombination as a possible explanation for the efficiency droop in GaN-based diodes", Applied Physics Letters **96**, 221106 (2010).

[42] J. Cho, E. F. Schubert, and J. K. Kim, "Efficiency droop in light-emitting diodes: Challenges and countermeasures", Laser & Photonics Reviews **7**, 408–421 (2013).

[43] J. Iveland, L. Martinelli, J. Peretti, J. S. Speck, and C. Weisbuch, "Direct measurement of Auger electrons emitted from a semiconductor light-emitting diode under electrical injection: identification of the dominant mechanism for efficiency droop", Physical review letters **110**, 177406 (2013).

[44] E. Kioupakis, D. Steiauf, P. Rinke, K. T. Delaney, and C. G. Van de Walle, "First-principles calculations of indirect Auger recombination in nitride semiconductors", Physical Review B **92**, 035207 (2015).

[45] Q. Y. P.-C. K. Christina M. Jones, Chu-Hsiang Teng and E. Kioupakis, "Impact of carrier localization on recombination in InGaN quantum wells and the efficiency of nitride light-emitting diodes: Insights from theory and numerical simulations", Applied Physics Letters **111**, 113501 (2017).

[46] C.-K. Tan, W. Sun, J. J. Wierer Jr, and N. Tansu, "Effect of interface roughness on Auger recombination in semiconductor quantum wells", AIP Advances **7**, 035212 (2017).

[47] A. David, N. G. Young, C. A. Hurni, and M. D. Craven, "Quantum Efficiency of III-Nitride Emitters: Evidence for Defect-Assisted Nonradiative Recombination and its Effect on the Green Gap", Physical Review Applied **11**, 031001 (2019).

[48] M. Auf der Maur, A. Pecchia, G. Penazzi, W. Rodrigues, and A. Di Carlo, "Efficiency Drop in Green InGaN/GaN Light Emitting Diodes: The Role of Random Alloy Fluctuations", Phys. Rev. Lett. **116**, 027401 (2016).

[49] C. Haller, J.-F. Carlin, G. Jacopin, W. Liu, D. Martin, R. Butté, and N. Grandjean, "GaN surface as the source of non-radiative defects in InGaN/GaN quantum wells", Applied Physics Letters **113**, 111106 (2018).

[50] S. Vilhunen, H. Särkkä, and M. Sillanpää, "Ultraviolet light-emitting diodes in water disinfection", Environmental Science and Pollution Research **16**, 439–442 (2009).

[51] W. L. Morison, Phototherapy and photochemotherapy for skin disease, CRC Press (2005).

[52] H. Hirayama, Recent Progress in AlGaN Deep-UV LEDs, IntechOpen (2018).

[53] T.-Y. Wang, C.-T. Tasi, C.-F. Lin, and D.-S. Wuu, "85% internal quantum efficiency of 280-nm AlGaN multiple quantum wells by defect engineering", Scientific reports **7**, 14422 (2017).

[54] M. Kneissl, T. Kolbe, C. Chua, V. Kueller, N. Lobo, J. Stellmach, A. Knauer, H. Rodriguez, S. Einfeldt, Z. Yang, *et al.*, "Advances in group III-nitride-based deep UV light-emitting diode technology", Semiconductor Science and Technology **26**, 014036 (2010).

[55] F. Römer, M. Deppner, Z. Andreev, C. Kölper, M. Sabathil, M. Strassburg, J. Ledig, S. Li, A. Waag, and B. Witzigmann, "Luminescence and efficiency optimization of InGaN/GaN core-shell nanowire LEDs by numerical modelling", Proceedings of SPIE **8255**, 82550H (2012).

[56] H.-M. Kim, Y.-H. Cho, H. Lee, S. I. Kim, S. R. Ryu, D. Y. Kim, T. W. Kang, and K. S. Chung, "High-brightness light emitting diodes using dislocation-free indium gallium nitride/gallium nitride multiquantum-well nanorod arrays", Nano letters **4**, 1059–1062 (2004).

[57] F. Glas, "Critical dimensions for the plastic relaxation of strained axial heterostructures in free-standing nanowires", Physical Review B **74**, 121302 (2006).

[58] L. F. Zagonel, S. Mazzucco, M. Tencé, K. March, R. Bernard, B. Laslier, G. Jacopin, M. Tchernycheva, L. Rigutti, F. H. Julien, *et al.*, "Nanometer scale spectral imaging of quantum emitters in nanowires and its correlation to their atomically resolved structure", Nano letters **11**, 568–573 (2010).

[59] T. Kuykendall, P. Ulrich, S. Aloni, and P. Yang, "Complete composition tunability of InGaN nanowires using a combinatorial approach", Nature materials **6**, 951 (2007).

[60] F. Olivier, A. Daami, C. Licitra, and F. Templier, "Shockley-Read-Hall and Auger non-radiative recombination in GaN based LEDs: A size effect study", Applied Physics Letters **111**, 022104 (2017).

[61] P. Gilet and I.-C. Robin, "Nanostructures on Silicon to Solve the Active Display Paradigms", in "SID Symposium Digest of Technical Papers", volume 49, pages 684–687, Wiley Online Library (2018).

[62] R. Calarco, M. Marso, T. Richter, A. I. Aykanat, R. Meijers, A. vd Hart, T. Stoica, and H. Lüth, "Size-dependent photoconductivity in MBE-grown GaN- nanowires", Nano letters **5**, 981–984 (2005).

[63] B. Deveaud, F. Clérot, N. Roy, K. Satzke, B. Sermage, and D. Katzer, "Enhanced radiative recombination of free excitons in GaAs quantum wells", Physical review letters **67**, 2355 (1991).

[64] Hamamatsu, Guide to streak cameras User's manual.

[65] S. Ono and K. Kanaya, "The energy dependence of secondary emission based on the range-energy retardation power formula", Journal of Physics D: Applied Physics **12**, 619 (1979).

[66] D. Drouin, A. R. Couture, D. Joly, X. Tastet, V. Aimez, and R. Gauvin, "CASINO V2. 42—a fast and easy-to-use modeling tool for scanning electron microscopy and microanalysis users", Scanning: The Journal of Scanning Microscopies **29**, 92–101 (2007).

[67] Y.-T. Chen, K. F. Karlsson, J. Birch, and P.-O. Holtz, "Determination of critical diameters for intrinsic carrier diffusion-length of GaN nanorods with cryo-scanning near-field optical microscopy", Scientific reports **6**, 21482 (2016).

Bibliography

[68] C. Gutsche, R. Niepelt, M. Gnauck, A. Lysov, W. Prost, C. Ronning, and F.-J. Tegude, "Direct determination of minority carrier diffusion lengths at axial GaAs nanowire p–n junctions", Nano letters **12**, 1453–1458 (2012).

[69] S. Sonderegger, E. Feltin, M. Merano, A. Crottini, J. F. Carlin, R. Sachot, B. Deveaud, N. Grandjean, and J. D. Ganière, "High spatial resolution picosecond cathodoluminescence of InGaN quantum wells", Applied Physics Letters **89**, 232109 (2006).

[70] M. Shahmohammadi, J.-D. Ganière, H. Zhang, R. Ciechonski, G. Vescovi, O. Kryliouk, M. Tchernycheva, and G. Jacopin, "Excitonic Diffusion in InGaN/GaN Core–Shell Nanowires", Nano Letters **16**, 243–249 (2016).

[71] T. Onuma, Y. Kagamitani, K. Hazu, T. Ishiguro, T. Fukuda, and S. F. Chichibu, "Femtosecond-laser-driven photoelectron-gun for time-resolved cathodoluminescence measurement of GaN", Review of Scientific Instruments **83**, 043905 (2012).

[72] A. Steckenborn, H. Münzel, and D. Bimberg, "Cathodoluminescence lifetime pattern of GaAs surfaces around dislocations", Journal of Luminescence **24**, 351–354 (1981).

[73] I. Weppelman, R. Moerland, J. Hoogenboom, and P. Kruit, "Concept and design of a beam blanker with integrated photoconductive switch for ultrafast electron microscopy", Ultramicroscopy **184**, 8–17 (2018).

[74] M. Merano, S. Sonderegger, A. Crottini, S. Collin, P. Renucci, E. Pelucchi, A. Malko, M. H. Baier, E. Kapon, B. Deveaud, and J.-D. Ganière, "Probing carrier dynamics in nanostructures by picosecond cathodoluminescence", Nature **438**, 479–482 (2005).

[75] A. M. Armstrong, B. N. Bryant, M. H. Crawford, D. D. Koleske, S. R. Lee, and J. J. Wierer Jr, "Defect-reduction mechanism for improving radiative efficiency in InGaN/GaN light-emitting diodes using InGaN underlayers", Journal of Applied Physics **117**, 134501 (2015).

[76] T. Akasaka, H. Gotoh, T. Saito, and T. Makimoto, "High luminescent efficiency of InGaN multiple quantum wells grown on InGaN underlying layers", Applied physics letters **85**, 3089–3091 (2004).

[77] C. Haller, J.-F. Carlin, G. Jacopin, D. Martin, R. Butté, and N. Grandjean, "Burying non-radiative defects in InGaN underlayer to increase InGaN/GaN quantum well efficiency", Applied Physics Letters **111**, 262101 (2017).

[78] S. F. Chichibu, A. Uedono, T. Onuma, B. A. Haskell, A. Chakraborty, T. Koyama, P. T. Fini, S. Keller, S. P. DenBaars, J. S. Speck, U. K. Mishra, S. Nakamura, S. Yamaguchi, S. Kamiyama, H. Amano, I. Akasaki, J. Han, and T. Sota, "Origin of defect-insensitive emission probability in In-containing (Al, In, Ga)N alloy semiconductors", Nature Materials **5**, 810–816 (2006).

[79] O. Brandt and K. H. Ploog, "Solid-state lighting: The benefit of disorder", Nature materials **5**, 769 (2006).

[80] . S. Rosner, E. Carr, M. Ludowise, G. Girolami, and H. Erikson, "Correlation of cathodo-luminescence inhomogeneity with microstructural defects in epitaxial GaN grown by metalorganic chemical-vapor deposition", Applied Physics Letters **70**, 420–422 (1997).

[81] S. Nakamura, "The roles of structural imperfections in InGaN-based blue light-emitting diodes and laser diodes", science **281**, 956–961 (1998).

[82] S. Pimputkar, J. S. Speck, S. P. DenBaars, and S. Nakamura, "Prospects for LED lighting", Nature photonics **3**, 180 (2009).

[83] C. A. Hurni, A. David, M. J. Cich, R. I. Aldaz, B. Ellis, K. Huang, A. Tyagi, R. A. DeLille, M. D. Craven, F. M. Steranka, *et al.*, "Bulk GaN flip-chip violet light-emitting diodes with optimized efficiency for high-power operation", Applied Physics Letters **106**, 031101 (2015).

[84] M. Shatalov, W. Sun, A. Lunev, X. Hu, A. Dobrinsky, Y. Bilenko, J. Yang, M. Shur, R. Gaska, C. Moe, *et al.*, "AlGaN deep-ultraviolet light-emitting diodes with external quantum efficiency above 10%", Applied Physics Express **5**, 082101 (2012).

[85] M. Albrecht, L. Lymperakis, and J. Neugebauer, "Origin of the unusually strong lumines-cence of *a*-type screw dislocations in GaN", Phys. Rev. B **90**, 241201(R) (2014).

[86] R. Liu, A. Bell, F. Ponce, C. Chen, J. Yang, and M. A. Khan, "Luminescence from stacking faults in gallium nitride", Applied Physics Letters **86**, 021908 (2005).

[87] G. Pozina, R. Ciechonski, Z. Bi, L. Samuelson, and B. Monemar, "Dislocation related droop in InGaN/GaN light emitting diodes investigated via cathodoluminescence", Applied Physics Letters **107**, 251106 (2015).

[88] X. Wu, C. Elsass, A. Abare, M. Mack, S. Keller, P. Petroff, S. DenBaars, J. Speck, and S. Rosner, "Structural origin of V-defects and correlation with localized excitonic centers in InGaN/GaN multiple quantum wells", Applied Physics Letters **72**, 692–694 (1998).

[89] T. Sugahara, H. Sato, M. Hao, Y. Naoi, S. Kurai, S. Tottori, K. Yamashita, K. Nishino, L. T. Romano, and S. Sakai, "Direct evidence that dislocations are non-radiative recombina-tion centers in GaN", Japanese journal of applied physics **37**, L398 (1998).

[90] D. Gogova, A. Kasic, H. Larsson, B. Pécz, R. Yakimova, B. Magnusson, B. Monemar, F. Tuomisto, K. Saarinen, C. Miskys, M. Stutzmann, C. Bundesmann, and M. Schubert, "Optical and Structural Characteristics of Virtually Unstrained Bulk-Like GaN", Japanese Journal of Applied Physics **43**, 1264–1268 (2004).

[91] H. Lu, X. Cao, S. LeBoeuf, H. Hong, E. Kaminsky, and S. Arthur, "Cathodoluminescence mapping and selective etching of defects in bulk GaN", Journal of Crystal Growth **291**, 82–85 (2006).

[92] V. M. Kaganer, J. Lähnemann, C. Pfüller, K. K. Sabelfeld, A. E. Kireeva, and O. Brandt, "Can we determine the carrier diffusion length in GaN from cathodoluminescence maps around threading dislocations?", arXiv preprint arXiv:1906.05645 (2019).

[93] N. Gmeinwieser, P. Gottfriedsen, U. T. Schwarz, W. Wegscheider, R. Clos, A. Krtschil, A. Krost, A. Weimar, G. Brüderl, A. Lell, and V. Härle, "Local strain and potential distribution induced by single dislocations in GaN", Journal of Applied Physics **98**, 116102 (2005).

[94] N. Gmeinwieser and U. T. Schwarz, "Pattern formation and directional and spatial ordering of edge dislocations in bulk GaN: Microphotoluminescence spectra and continuum elastic calculations", Physical Review B **75** (2007).

[95] W. Harding, I. Blenkinsop, and D. Wight, "Dislocation-limited minority-carrier lifetime in n-type GaP", Electronics Letters **12**, 503 (1976).

[96] G. Jacopin, M. Shahmohammadi, J.-D. Ganière, and B. Deveaud, "Hopping process of bound excitons under an energy gradient", Applied Physics Letters **104**, 042109 (2014).

[97] S. L. Rhode, M. K. Horton, W. Y. Fu, S.-L. Sahonta, M. J. Kappers, T. J. Pennycook, C. J. Humphreys, R. O. Dusane, and M. A. Moram, "Dislocation core structures in Si-doped GaN", Applied Physics Letters **107**, 243104 (2015).

[98] A. Pinos, S. Marcinkevičius, M. Usman, and A. Hallén, "Time-resolved luminescence studies of proton-implanted GaN", Applied Physics Letters **95**, 112108 (2009).

[99] A. Krtschil, A. Dadgar, and A. Krost, "Electrical microcharacterization of dislocation-related charges in GaN-based single layers by scanning probe microscopy techniques", Journal of Crystal Growth **248**, 542–547 (2003).

[100] S. Limpijumnong and C. G. Van de Walle, "Diffusivity of native defects in GaN", Physical Review B **69**, 035207 (2004).

[101] T. Bezyazychnaya, D. Kabanau, V. Kabanov, Y. Lebiadok, A. Ryabtsev, G. Ryabtsev, V. Zelenkovskii, and S. Mehta, "Influence of vacancies on indium atom distribution in InGaAs and InGaN compounds", Lithuanian Journal of Physics **55**, 10 (2015).

[102] A. Uedono, T. Watanabe, S. Kimura, Y. Zhang, M. Lozac'h, L. Sang, S. Ishibashi, N. Oshima, R. Suzuki, and M. Sumiya, "Vacancy-type defects in In x Ga1- x N grown on GaN templates probed using monoenergetic positron beams", Journal of Applied Physics **114**, 184504 (2013).

[103] Y. Kawakami, K. Omae, A. Kaneta, K. Okamoto, T. Izumi, S. Sajou, K. Inoue, Y. Narukawa, T. Mukai, and S. Fujita, "Radiative and Nonradiative Recombination Processes in GaN-Based Semiconductors", physica status solidi (a) **183**, 41–50 (2001).

[104] K. Muraki, S. Fukatsu, Y. Shiraki, and R. Ito, "Surface segregation of In atoms during molecular beam epitaxy and its influence on the energy levels in InGaAs/GaAs quantum wells", Applied Physics Letters **61**, 557–559 (1992).

[105] D. Wickramaratne, J.-X. Shen, C. E. Dreyer, M. Engel, M. Marsman, G. Kresse, S. Marcinkevičius, A. Alkauskas, and C. G. Van de Walle, "Iron as a source of efficient Shockley-Read-Hall recombination in GaN", Applied Physics Letters **109**, 162107 (2016).

[106] T. Uždavinys, S. Marcinkevičius, J. Leach, K. Evans, and D. C. Look, "Photoexcited carrier trapping and recombination at Fe centers in GaN", Journal of Applied Physics **119**, 215706 (2016).

[107] M. A. Reshchikov, D. Demchenko, A. Usikov, H. Helava, and Y. Makarov, "Carbon defects as sources of the green and yellow luminescence bands in undoped GaN", Physical Review B **90**, 235203 (2014).

[108] C. E. Dreyer, A. Alkauskas, J. L. Lyons, J. S. Speck, and C. G. Van de Walle, "Gallium vacancy complexes as a cause of Shockley-Read-Hall recombination in III-nitride light emitters", Applied Physics Letters **108**, 141101 (2016).

[109] R. Pässler, "Temperature dependences of the nonradiative multiphonon carrier capture and ejection properties of deep traps in semiconductors. I. Theoretical results", physica status solidi (b) **85**, 203–215 (1978).

[110] A. Hangleiter, T. Langer, P. Henning, F. A. Ketzer, H. Bremers, and U. Rossow, "Internal quantum efficiency of nitride light emitters: a critical perspective", in "Gallium Nitride Materials and Devices XIII", volume 10532, page 105321P, International Society for Optics and Photonics (2018).

[111] M. Shiojiri, C. Chuo, J. Hsu, J. Yang, and H. Saijo, "Structure and formation mechanism of V defects in multiple In Ga N/ Ga N quantum well layers", Journal of applied physics **99**, 073505 (2006).

[112] S. P. DenBaars, D. Feezell, K. Kelchner, S. Pimputkar, C.-C. Pan, C.-C. Yen, S. Tanaka, Y. Zhao, N. Pfaff, R. Farrell, *et al.*, "Development of gallium-nitride-based light-emitting diodes (LEDs) and laser diodes for energy-efficient lighting and displays", Acta Materialia **61**, 945–951 (2013).

[113] M.-H. Chang, D. Das, P. Varde, and M. Pecht, "Light emitting diodes reliability review", Microelectronics Reliability **52**, 762–782 (2012).

[114] S. Chichibu, A. Abare, M. Mack, M. Minsky, T. Deguchi, D. Cohen, P. Kozodoy, S. Fleischer, S. Keller, J. Speck, *et al.*, "Optical properties of InGaN quantum wells", Materials Science and Engineering: B **59**, 298–306 (1999).

[115] P. Waltereit, O. Brandt, A. Trampert, H. Grahn, J. Menniger, M. Ramsteiner, M. Reiche, and K. Ploog, "Nitride semiconductors free of electrostatic fields for efficient white light-emitting diodes", Nature **406**, 865 (2000).

[116] K.-C. Kim, M. C. Schmidt, H. Sato, F. Wu, N. Fellows, Z. Jia, M. Saito, S. Nakamura, S. P. DenBaars, J. S. Speck, *et al.*, "Study of nonpolar m-plane InGaN/GaN multiquantum well light emitting diodes grown by homoepitaxial metal-organic chemical vapor deposition", Applied Physics Letters **91**, 181120 (2007).

[117] E. Matioli, S. Brinkley, K. M. Kelchner, Y.-L. Hu, S. Nakamura, S. DenBaars, J. Speck, and C. Weisbuch, "High-brightness polarized light-emitting diodes", Light: Science & Applications **1**, e22 (2012).

[118] G. A. Garrett, H. Shen, M. Wraback, A. Tyagi, M. C. Schmidt, J. S. Speck, S. P. DenBaars, and S. Nakamaura, "Comparison of time-resolved photoluminescence from InGaN single quantum wells grown on nonpolar and semipolar bulk GaN substrates", physica status solidi c **6**, S800–S803 (2009).

[119] Y. Huang, K. Sun, A. Fischer, Q. Wei, R. Juday, F. Ponce, R. Kato, and T. Yokogawa, "Effect of misfit dislocations on luminescence in m-plane InGaN quantum wells", Applied Physics Letters **98**, 261914 (2011).

[120] S. Marcinkevičius, K. Kelchner, L. Kuritzky, S. Nakamura, S. DenBaars, and J. Speck, "Photoexcited carrier recombination in wide m-plane InGaN/GaN quantum wells", Applied Physics Letters **103**, 111107 (2013).

[121] S. Marcinkevičius, K. M. Kelchner, S. Nakamura, S. P. DenBaars, and J. S. Speck, "Optical properties and carrier dynamics in m-plane InGaN quantum wells", physica status solidi (c) **11**, 690–693 (2014).

[122] D. Sutherland, T. Zhu, J. T. Griffiths, F. Tang, P. Dawson, D. Kundys, F. Oehler, M. J. Kappers, C. J. Humphreys, and R. A. Oliver, "Optical studies of non-polar m-plane () InGaN/GaN multi-quantum wells grown on freestanding bulk GaN", physica status solidi (b) **252**, 965–970 (2015).

[123] T. Langer, M. Klisch, F. Alexej Ketzer, H. Jönen, H. Bremers, U. Rossow, T. Meisch, F. Scholz, and A. Hangleiter, "Radiative and nonradiative recombination mechanisms in nonpolar and semipolar GaInN/GaN quantum wells", physica status solidi (b) **253**, 133–139 (2016).

[124] P. Dawson, S. Schulz, R. A. Oliver, M. Kappers, and C. J. Humphreys, "The nature of carrier localisation in polar and nonpolar InGaN/GaN quantum wells", Journal of Applied Physics **119**, 181505 (2016).

[125] R. N. Hall, "Electron-hole recombination in germanium", Physical review **87**, 387 (1952).

[126] W. Shockley and W. Read Jr, "Statistics of the recombinations of holes and electrons", Physical review **87**, 835 (1952).

[127] O. Brandt, H. Yang, and K. H. Ploog, "Impact of recombination centers on the spontaneous emission of semiconductors under steady-state and transient conditions", Physical Review B **54**, R5215 (1996).

[128] T. Langer, A. Chernikov, D. Kalincev, M. Gerhard, H. Bremers, U. Rossow, M. Koch, and A. Hangleiter, "Room temperature excitonic recombination in GaInN/GaN quantum wells", Applied Physics Letters **103**, 202106 (2013).

[129] A. David, C. A. Hurni, N. G. Young, and M. D. Craven, "Field-assisted Shockley-Read-Hall recombinations in III-nitride quantum wells", Applied Physics Letters **111**, 233501 (2017).

[130] G. Rossbach, J. Levrat, G. Jacopin, M. Shahmohammadi, J.-F. Carlin, J.-D. Ganière, R. Butté, B. Deveaud, and N. Grandjean, "High-temperature Mott transition in wide-band-gap semiconductor quantum wells", Physical Review B **90**, 201308 (2014).

[131] A. Hangleiter, Z. Jin, M. Gerhard, D. Kalincev, T. Langer, H. Bremers, U. Rossow, M. Koch, M. Bonn, and D. Turchinovich, "Efficient formation of excitons in a dense electron-hole plasma at room temperature", Phys. Rev. B **92**, 241305 (2015).

[132] A. Hangleiter, T. Langer, M. Gerhard, D. Kalincev, A. Kruse, H. Bremers, U. Rossow, and M. Koch, "Efficiency droop in nitride LEDs revisited: impact of excitonic recombination processes", in "Gallium Nitride Materials and Devices X", volume 9363, page 93631R, International Society for Optics and Photonics (2015).

[133] A. David and M. J. Grundmann, "Droop in InGaN light-emitting diodes: A differential carrier lifetime analysis", Applied Physics Letters **96**, 103504 (2010).

[134] S. Khatsevich and D. Rich, "The effects of crystallographic orientation and strain on the properties of excitonic emission from wurtzite InGaN/GaN quantum wells", Journal of Physics: Condensed Matter **20**, 215223 (2008).

[135] E. Kioupakis, D. Steiauf, P. Rinke, K. T. Delaney, and C. G. Van de Walle, "First-principles calculations of indirect Auger recombination in nitride semiconductors", Phys. Rev. B **92**, 035207 (2015).

[136] L. Schade, T. Wernicke, J. Rass, S. Ploch, M. Weyers, M. Kneissl, and U. Schwarz, "On optical polarization and charge carrier statistics of nonpolar InGaN quantum wells", physica status solidi (b) **253**, 145–157 (2016).

[137] R. Huber, F. Tauser, A. Brodschelm, M. Bichler, G. Abstreiter, and A. Leitenstorfer, "How many-particle interactions develop after ultrafast excitation of an electron–hole plasma", Nature **414**, 286 (2001).

[138] P. Corfdir, J. Levrat, G. Rossbach, R. Butté, E. Feltin, J.-F. Carlin, G. Christmann, P. Lefebvre, J.-D. Ganière, N. Grandjean, and B. Deveaud-Plédran, "Impact of biexcitons on the relaxation mechanisms of polaritons in III-nitride based multiple quantum well microcavities", Phys. Rev. B **85**, 245308 (2012).

[139] D. Snoke, "Predicting the ionization threshold for carriers in excited semiconductors", Solid State Communications **146**, 73–77 (2008).

[140] M. Shahmohammadi, G. Jacopin, G. Rossbach, J. Levrat, E. Feltin, J.-F. Carlin, J.-D. Ganiere, R. Butté, N. Grandjean, and B. Deveaud, "Biexcitonic molecules survive excitons at the Mott transition", Nature communications **5**, 5251 (2014).

[141] L.-X. Zhai, Y. Wang, and J.-J. Liu, "Screening effect on the binding energy of the exciton in quantum wires", Journal of Applied Physics **112**, 033709 (2012).

[142] G. Rossbach, J. Levrat, E. Feltin, J.-F. m. c. Carlin, R. Butté, and N. Grandjean, "Impact of saturation on the polariton renormalization in III-nitride based planar microcavities", Phys. Rev. B **88**, 165312 (2013).

[143] M. Funato and Y. Kawakami, "Excitonic properties of polar, semipolar, and nonpolar In Ga N/ Ga N strained quantum wells with potential fluctuations", Journal of Applied Physics **103**, 093501 (2008).

Bibliography

[144] A. E. Siegman, M. Sasnett, and T. Johnston, "Choice of clip levels for beam width measurements using knife-edge techniques", IEEE Journal of Quantum Electronics **27**, 1098–1104 (1991).

[145] H. Amano, N. Watanabe, N. Koide, and I. Akasaki, "Room-temperature low-threshold surface-stimulated emission by optical pumping from Al0. 1Ga0. 9N/GaN double heterostructure", Japanese journal of applied physics **32**, L1000 (1993).

[146] J. Muth, J. Lee, I. Shmagin, R. Kolbas, H. Casey Jr, B. Keller, U. Mishra, and S. DenBaars, "Absorption coefficient, energy gap, exciton binding energy, and recombination lifetime of GaN obtained from transmission measurements", Applied Physics Letters **71**, 2572–2574 (1997).

[147] P. Corfdir, J. Levrat, A. Dussaigne, P. Lefebvre, H. Teisseyre, I. Grzegory, T. Suski, J.-D. Ganière, N. Grandjean, and B. Deveaud-Plédran, "Intrinsic dynamics of weakly and strongly confined excitons in nonpolar nitride-based heterostructures", Phys. Rev. B **83**, 245326 (2011).

[148] A. Alkauskas, C. E. Dreyer, J. L. Lyons, and C. G. Van de Walle, "Role of excited states in Shockley-Read-Hall recombination in wide-band-gap semiconductors", Phys. Rev. B **93**, 201304 (2016).

[149] M. R. Krames, G. Christenson, D. Collins, L. W. Cook, M. G. Craford, A. Edwards, R. M. Fletcher, N. F. Gardner, W. K. Goetz, W. R. Imler, *et al.*, "High-brightness AlGaInN light-emitting diodes", in "Light-Emitting Diodes: Research, Manufacturing, and Applications IV", volume 3938, pages 2–13, International Society for Optics and Photonics (2000).

[150] T. Mukai, M. Yamada, and S. Nakamura, "Characteristics of InGaN-based UV/blue/-green/amber/red light-emitting diodes", Japanese Journal of Applied Physics **38**, 3976 (1999).

[151] M. Binder, A. Nirschl, R. Zeisel, T. Hager, H.-J. Lugauer, M. Sabathil, D. Bougeard, J. Wagner, and B. Galler, "Identification of nnp and npp Auger recombination as significant contributor to the efficiency droop in (GaIn) N quantum wells by visualization of hot carriers in photoluminescence", Applied Physics Letters **103**, 071108 (2013).

[152] E. Kioupakis, P. Rinke, K. T. Delaney, and C. G. Van de Walle, "Indirect Auger recombination as a cause of efficiency droop in nitride light-emitting diodes", Applied Physics Letters **98**, 161107 (2011).

[153] F. Bertazzi, X. Zhou, M. Goano, G. Ghione, and E. Bellotti, "Auger recombination in InGaN/GaN quantum wells: A full-Brillouin-zone study", Applied Physics Letters **103**, 081106 (2013).

[154] J. Piprek, F. Römer, and B. Witzigmann, "On the uncertainty of the Auger recombination coefficient extracted from InGaN/GaN light-emitting diode efficiency droop measurements", Applied Physics Letters **106**, 101101 (2015).

[155] S. F. Chichibu, A. Uedono, T. Onuma, B. A. Haskell, A. Chakraborty, T. Koyama, P. T. Fini, S. Keller, S. P. DenBaars, J. S. Speck, *et al.*, "Origin of defect-insensitive emission

probability in In-containing (Al, In, Ga) N alloy semiconductors", Nature materials **5**, 810 (2006).

[156] M. Leroux, N. Grandjean, M. Laügt, J. Massies, B. Gil, P. Lefebvre, and P. Bigen-wald, "Quantum confined Stark effect due to built-in internal polarization fields in (Al,Ga)N/GaN quantum wells", Phys. Rev. B **58**, R13371–R13374 (1998).

[157] T. Takeuchi, S. Sota, M. Katsuragawa, M. Komori, H. Takeuchi, H. Amano, and I. Akasaki, "Quantum-confined Stark effect due to piezoelectric fields in GaInN strained quantum wells", Japanese Journal of Applied Physics **36**, L382 (1997).

[158] Y.-H. Cho, G. Gainer, A. Fischer, J. Song, S. Keller, U. Mishra, and S. DenBaars, ""S-shaped" temperature-dependent emission shift and carrier dynamics in InGaN/GaN multiple quantum wells", Applied Physics Letters **73**, 1370–1372 (1998).

[159] R. Butté and N. Grandjean, Polarization Effects in Semiconductors, from Ab Initio Theory to Device Applications, Springer US, Boston, MA (2008), edited by C. Wood and D. Jena.

[160] N. Mott, "The mobility edge since 1967", Journal of Physics C: Solid State Physics **20**, 3075–3102 (1987).

[161] L. C. Andreani, F. Tassone, and F. Bassani, "Radiative lifetime of free excitons in quantum wells", Solid State Communications **77**, 641 – 645 (1991).

[162] A. L. Efros, C. Wetzel, and J. M. Worlock, "Effect of a random adiabatic potential on the optical properties of two-dimensional excitons", Phys. Rev. B **52**, 8384–8390 (1995).

[163] K. K. Sabelfeld, O. Brandt, and V. M. Kaganer, "Stochastic model for the fluctuation-limited reaction–diffusion kinetics in inhomogeneous media based on the nonlinear Smoluchowski equations", Journal of Mathematical Chemistry **53**, 651–669 (2015).

[164] K. Kojima, A. A. Yamaguchi, M. Funato, Y. Kawakami, and S. Noda, "Impact of nonpolar AlGaN quantum wells on deep ultraviolet laser diodes", Journal of Applied Physics **110**, 043115 (2011).

[165] B. Deveaud, F. Clérot, N. Roy, K. Satzke, B. Sermage, and D. S. Katzer, "Enhanced radiative recombination of free excitons in GaAs quantum wells", Phys. Rev. Lett. **67**, 2355–2358 (1991).

[166] M. D. C. F. S. V. S. N. F. C. A. M. P. R. G. L. A. C. C. M. A. Q. F. M. A. B. G. Saba Michele, Cadelano Michele, "Correlated electron-hole plasma in organometal perovskites", Nature Communications **5**, 5049 (2014).

[167] R. Vaxenburg, A. Rodina, E. Lifshitz, and A. L. Efros, "The role of polarization fields in Auger-induced efficiency droop in nitride-based light-emitting diodes", Applied Physics Letters **103**, 221111 (2013).

[168] E. Kioupakis, Q. Yan, and C. G. Van de Walle, "Interplay of polarization fields and Auger recombination in the efficiency droop of nitride light-emitting diodes", Applied Physics Letters **101**, 231107 (2012).

Bibliography

[169]   K. Iso, H. Yamada, H. Hirasawa, N. Fellows, M. Saito, K. Fujito, S. P. DenBaars, J. S. Speck, and S. Nakamura, "High Brightness Blue InGaN/GaN Light Emitting Diode on Nonpolarm-plane Bulk GaN Substrate", Japanese Journal of Applied Physics **46**, L960–L962 (2007).

[170]   Y.-D. Lin, A. Chakraborty, S. Brinkley, H. C. Kuo, T. Melo, K. Fujito, J. S. Speck, S. P. DenBaars, and S. Nakamura, "Characterization of blue-green m-plane InGaN light emitting diodes", Applied Physics Letters **94**, 261108 (2009).

[171]   M. J. Davies, P. Dawson, S. Hammersley, T. Zhu, M. J. Kappers, C. J. Humphreys, and R. A. Oliver, "Comparative studies of efficiency droop in polar and non-polar InGaN quantum wells", Applied Physics Letters **108**, 252101 (2016).

[172]   K. Ueda, T. Tayagaki, M. Fukuda, M. Fujii, and Y. Kanemitsu, "Breakdown of the k-conservation rule in quantized Auger recombination in $Si_{1-x}Ge_x$ nanocrystals", Phys. Rev. B **86**, 155316 (2012).

[173]   Y. Kobayashi and N. Tamai, "Size-Dependent Multiexciton Spectroscopy and Moderate Temperature Dependence of Biexciton Auger Recombination in Colloidal CdTe Quantum Dots", The Journal of Physical Chemistry C **114**, 17550–17556 (2010).

[174]   F. Natali, D. Byrne, M. Leroux, B. Damilano, F. Semond, A. Le Louarn, S. Vezian, N. Grandjean, and J. Massies, "Inhomogeneous broadening of $Al_xGa_{1-x}NGaN$ quantum wells", Phys. Rev. B **71**, 075311 (2005).

[175]   M. Yoshikawa, M. Kunzer, J. Wagner, H. Obloh, P. Schlotter, R. Schmidt, N. Herres, and U. Kaufmann, "Band-gap renormalization and band filling in Si-doped GaN films studied by photoluminescence spectroscopy", Journal of Applied Physics **86**, 4400–4402 (1999).

[176]   D. Kleinman and R. Miller, "Band-gap renormalization in semiconductor quantum wells containing carriers", Physical Review B **32**, 2266 (1985).

[177]   D. Robbins and P. Landsberg, "Impact ionisation and Auger recombination involving traps in semiconductors", Journal of Physics C: Solid State Physics **13**, 2425 (1980).

[178]   H. Wang, C. Zhang, and F. Rana, "Ultrafast dynamics of defect-assisted electron–hole recombination in monolayer MoS2", Nano letters **15**, 339–345 (2014).

[179]   S. K. Pang, A. W. Smith, and A. Rohatgi, "Effect of trap location and trap-assisted Auger recombination on silicon solar cell performance", IEEE Transactions on Electron Devices **42**, 662–668 (1995).

[180]   C. Haller, J.-F. Carlin, M. Mosca, M. D. Rossell, R. Erni, and N. Grandjean, "InAlN underlayer for near ultraviolet InGaN based light emitting diodes", Applied Physics Express **12**, 034002 (2019).

[181]   W. Liu, R. Butté, A. Dussaigne, N. Grandjean, B. Deveaud, and G. Jacopin, "Carrier-density-dependent recombination dynamics of excitons and electron-hole plasma in m-plane InGaN/GaN quantum wells", Phys. Rev. B **94**, 195411 (2016).

[182] A. David, C. A. Hurni, N. G. Young, and M. D. Craven, "Electrical properties of III-Nitride LEDs: Recombination-based injection model and theoretical limits to electrical efficiency and electroluminescent cooling", Applied Physics Letters **109**, 083501 (2016).

[183] S. Li and A. Waag, "GaN based nanorods for solid state lighting", Journal of Applied Physics **111**, 5 (2012).

[184] R. Koester, D. Sager, W.-A. Quitsch, O. Pfingsten, A. Poloczek, S. Blumenthal, G. Keller, W. Prost, G. Bacher, and F.-J. Tegude, "High-speed GaN/GaInN nanowire array light-emitting diode on silicon (111)", Nano letters **15**, 2318–2323 (2015).

[185] M. D. Brubaker, P. T. Blanchard, J. B. Schlager, A. W. Sanders, A. Roshko, S. M. Duff, J. M. Gray, V. M. Bright, N. A. Sanford, and K. A. Bertness, "On-chip optical interconnects made with gallium nitride nanowires", Nano letters **13**, 374–377 (2013).

[186] S. Sadaf, S. Zhao, Y. Wu, Y.-H. Ra, X. Liu, S. Vanka, and Z. Mi, "An AlGaN core–shell tunnel junction nanowire light-emitting diode operating in the ultraviolet-C band", Nano letters **17**, 1212–1218 (2017).

[187] N. Guan, X. Dai, A. Messanvi, H. Zhang, J. Yan, E. Gautier, C. Bougerol, F. H. Julien, C. Durand, J. Eymery, *et al.*, "Flexible white light emitting diodes based on nitride nanowires and nanophosphors", ACS photonics **3**, 597–603 (2016).

[188] H. Zhang, X. Dai, N. Guan, A. Messanvi, V. Neplokh, V. Piazza, M. Vallo, C. Bougerol, F. H. Julien, A. Babichev, *et al.*, "Flexible photodiodes based on nitride core/shell p–n junction nanowires", ACS applied materials & interfaces **8**, 26198–26206 (2016).

[189] A. Waag, X. Wang, S. Fündling, J. Ledig, M. Erenburg, R. Neumann, M. Al Suleiman, S. Merzsch, J. Wei, S. Li, *et al.*, "The nanorod approach: GaN NanoLEDs for solid state lighting", physica status solidi c **8**, 2296–2301 (2011).

[190] S. Boubanga-Tombet, J. B. Wright, P. Lu, M. R. Williams, C. Li, G. T. Wang, and R. P. Prasankumar, "Ultrafast carrier capture and auger recombination in single GaN/InGaN multiple quantum well nanowires", ACS Photonics **3**, 2237–2242 (2016).

[191] J. R. Riley, S. Padalkar, Q. Li, P. Lu, D. D. Koleske, J. J. Wierer, G. T. Wang, and L. J. Lauhon, "Three-dimensional mapping of quantum wells in a GaN/InGaN core–shell nanowire light-emitting diode array", Nano letters **13**, 4317–4325 (2013).

[192] M. Tchernycheva, P. Lavenus, H. Zhang, A. V. Babichev, G. Jacopin, M. Shahmohammadi, F. H. Julien, R. Ciechonski, G. Vescovi, and O. Kryliouk, "InGaN/GaN Core–Shell Single Nanowire Light Emitting Diodes with Graphene-Based P-Contact", Nano Letters **14**, 2456–2465 (2014).

[193] M. Mandl, X. Wang, T. Schimpke, C. Kölper, M. Binder, J. Ledig, A. Waag, X. Kong, A. Trampert, F. Bertram, J. Christen, F. Barbagini, E. Calleja, and M. Strassburg, "Group III nitride core–shell nano- and microrods for optoelectronic applications", physica status solidi (RRL) – Rapid Research Letters **7**, 800–814 (2013).

[194] M. S. Mohajerani, S. Khachadorian, T. Schimpke, C. Nenstiel, J. Hartmann, J. Ledig, A. Avramescu, M. Strassburg, A. Hoffmann, and A. Waag, "Evaluation of local free carrier concentrations in individual heavily-doped GaN:Si micro-rods by micro-Raman spectroscopy", Applied Physics Letters **108**, 091112 (2016).

[195] X. Fu, G. Jacopin, M. Shahmohammadi, R. Liu, M. Benameur, J.-D. Ganière, J. Feng, W. Guo, Z.-M. Liao, B. Deveaud, and D. Yu, "Exciton Drift in Semiconductors under Uniform Strain Gradients: Application to Bent ZnO Microwires", ACS Nano **8**, 3412–3420 (2014).

[196] A. M. Armstrong, B. N. Bryant, M. H. Crawford, D. D. Koleske, S. R. Lee, and J. J. Wierer, "Defect-reduction mechanism for improving radiative efficiency in InGaN/GaN light-emitting diodes using InGaN underlayers", Journal of Applied Physics **117**, 134501 (2015).

[197] J. Lähnemann, P. Corfdir, F. Feix, J. Kamimura, T. Flissikowski, H. T. Grahn, L. Geelhaar, and O. Brandt, "Radial Stark Effect in (In,Ga)N Nanowires", Nano Letters **16**, 917–925 (2016).

[198] M. Müller, P. Veit, F. F. Krause, T. Schimpke, S. Metzner, F. Bertram, T. Mehrtens, K. Müller-Caspary, A. Avramescu, M. Strassburg, A. Rosenauer, and J. Christen, "Nanoscopic Insights into InGaN/GaN Core–Shell Nanorods: Structure, Composition, and Luminescence", Nano Letters **16**, 5340–5346 (2016).

[199] C. Mounir, T. Schimpke, G. Rossbach, A. Avramescu, M. Strassburg, and U. T. Schwarz, "Optical properties and internal quantum efficiency of InGaN/GaN core-shell microrods for solid state lighting", Journal of Applied Physics **120**, 155702 (2016).

[200] S. Hafiz, F. Zhang, M. Monavarian, V. Avrutin, H. Morkoç, U. Özgür, S. Metzner, F. Bertram, J. Christen, and B. Gil, "Determination of carrier diffusion length in GaN", Journal of Applied Physics **117**, 013106 (2015).

[201] Y. T. Chen, K. F. Karlsson, J. Birch, and P. O. Holtz, "Determination of critical diameters for intrinsic carrier diffusion-length of GaN nanorods with cryo-scanning near-field optical microscopy", Scientific Reports **6**, 21482 (2016).

[202] N. Ino and N. Yamamoto, "Low temperature diffusion length of excitons in gallium nitride measured by cathodoluminescence technique", Applied Physics Letters **93**, 232103 (2008).

[203] A. Kaneta, M. Funato, and Y. Kawakami, "Nanoscopic recombination processes in InGaN/GaN quantum wells emitting violet, blue, and green spectra", Phys. Rev. B **78**, 125317 (2008).

[204] S. Chichibu, A. Abare, M. Mack, M. Minsky, T. Deguchi, D. Cohen, P. Kozodoy, S. Fleischer, S. Keller, J. Speck, J. Bowers, E. Hu, U. Mishra, L. Coldren, S. DenBaars, K. Wada, T. Sota, and S. Nakamura, "Optical properties of InGaN quantum wells", Materials Science and Engineering: B **59**, 298 – 306 (1999).

[205] M. Tchernycheva, P. Lavenus, H. Zhang, A. Babichev, G. Jacopin, M. Shahmohammadi, F. Julien, R. Ciechonski, G. Vescovi, and O. Kryliouk, "InGaN/GaN core–shell single nanowire light emitting diodes with graphene-based p-contact", Nano Letters **14**, 2456–2465 (2014).

[206] M. Müller, P. Veit, F. F. Krause, T. Schimpke, S. Metzner, F. Bertram, T. Mehrtens, K. Müller-Caspary, A. Avramescu, M. Strassburg, *et al.*, "Nanoscopic Insights into InGaN/GaN Core–Shell Nanorods: Structure, Composition, and Luminescence", Nano letters **16**, 5340–5346 (2016).

[207] C. Jones, C.-H. Teng, Q. Yan, P.-C. Ku, and E. Kioupakis, "Impact of Anderson localization on carrier recombination in InGaN quantum wells and the efficiency of nitride light-emitting diodes", Applied Physics Letters **111**, 113501 (2017).

[208] Y. Hou, J. Bai, R. Smith, and T. Wang, "A single blue nanorod light emitting diode", Nanotechnology **27**, 205205 (2016).

[209] R. Zimmermann, F. Grosse, and E. Runge, "Excitons in semiconductor nanostructures with disorder", Pure and Applied Chemistry **69**, 1179–1186 (1997).

[210] M. Vallone, M. Goano, F. Bertazzi, and G. Ghione, "Carrier capture in InGaN/GaN quantum wells: Role of electron-electron scattering", Journal of Applied Physics **121**, 123107 (2017).

[211] F. Natali, D. Byrne, M. Leroux, B. Damilano, F. Semond, A. Le Louarn, S. Vezian, N. Grand-jean, and J. Massies, "Inhomogeneous broadening of Al x Ga 1-x N/ Ga N quantum wells", Physical Review B **71**, 075311 (2005).

[212] H. Wang, Z. Ji, S. Qu, G. Wang, Y. Jiang, B. Liu, X. Xu, and H. Mino, "Influence of excitation power and temperature on photoluminescence in InGaN/GaN multiple quantum wells", Optics Express **20**, 3932–3940 (2012).

[213] A. McAllister, D. Bayerl, and E. Kioupakis, "Radiative and Auger recombination processes in indium nitride", Applied Physics Letters **112**, 251108 (2018).

[214] E. Kioupakis, Q. Yan, D. Steiauf, and C. G. Van de Walle, "Temperature and carrier-density dependence of Auger and radiative recombination in nitride optoelectronic devices", New Journal of Physics **15**, 125006 (2013).

[215] M. Mohajerani, S. Khachadorian, T. Schimpke, C. Nenstiel, J. Hartmann, J. Ledig, A. Avramescu, M. Strassburg, A. Hoffmann, and A. Waag, "Evaluation of local free carrier concentrations in individual heavily-doped GaN: Si micro-rods by micro-Raman spectroscopy", Applied Physics Letters **108**, 091112 (2016).

List of Acronyms

AFM	atomic force microscopy
AOM	acousto-optic modulator
BGR	band gap renormalization
BBO	beta barium borate
CB	conduction band
CL	cathodoluminescence
CW	continuous-wave
CRI	color rendering index
DOE	Department of Energy
E-k	energy-momentum
e-h	electron-hole
EQE	external quantum efficiency
EL	electroluminescence
ECV	electrochemical capacitance-voltage
EDX	dispersive x-ray
FEG	field-emission gun
FWHM	full width at half maximum
GTI	Gires-Tournois interferometer
hh	heavy-hole
IQE	internal quantum efficiency
lh	light-hole
LL	localization landscape
LBO	lithium triborate
LED	light-emitting diodes
MQW	multi-quantum well
MT	Mott-transition
MCP	micro-channel plate
MOCVD	metal-organic chemical vapor deposition
MLs	monolayers
MRs	microrods
MC	color-mixed
NRCs	non-radiative recombination centers
NUV	near ultraviolet
1-3 D	one-three dimensional
PL	photoluminescence
PLE	photoluminescence excitation
PC	phosphor-conversion
QWs	quantum wells
QCSE	quantum-confined Stark effect
RF	radio frequency
so	split-off
SQW	single quantum well
SRH	Shockley–Read–Hall

SEM	scanning electron microscope	**TR-PL**	time-resolved photoluminescence
SE	secondary electron	**TEM**	transmission electron microscopy
STEM	scanning transmission electron microscopy	**TDD**	threading dislocation density
		UL	underlayer
SHG	second harmonic generation	**VBs**	valence bands
SL	superlattice	**UV**	ultra-violet
SDs	surface defects	**WPE**	wall plug efficiency
TR-CL	time-resolved cathodoluminescence		

Acknowledgements

Acknowledgements

Rousseau, Joachim Ciers, who bring diverse knowledge and cheerful atmosphere for the last four years. I would like to thank secretary Nadja Dekumbis for her great support in the daily work. I would like to thank LOEQ members, Merhan Shahmohammadi, Mahmoud Hezam, Hadis Abbaspour, Albert Adiyatullin, Morteza Navadeh, Claudéric Ouellet-Plamondon, Grégory Sallen, Mitchell Anderson, Daniel Oberli, Marcia Portella, François Morier-Genoud, who share knowledge of fascinating quantum optics and joyful office time. I would like to thank secretary Claire-Lyse Rouiller for her kind support for my relocation in Lausanne and the daily work.

In the end, I would like to thank my father Liangyou Liu and mother Tianxiu Liu, for giving their son life, faith, and education. I would like to thank my wife Dr. Jingjing Liu for being my destiny. I cherish every moment since we met. I would like to thank my friends for their company with unforgettable happiness in the Alps and the lakes in Switzerland.

Lausanne, 27. Sept. 2019   Wei Liu

CV

Name: **Wei Liu**
Nationality: Chinese
Email: we.liu@epfl.ch
Address: CH A3 425, LASPE, Institute of Physics, EPFL, Lausanne CH-1015, Switzerland

Education background

- *03. 2015-08. 2019* PhD student, institute of physics, EPFL, Switzerland.
  Supervisors: Prof. Nicolas Grandjean, Dr. Gwénolé Jacopin, Prof. Benoît Deveaud
  PhD topic: ultrafast carrier dynamics in III-nitride nanostructures and LED quantum efficiency.
- *09. 2010-06. 2013* master of microelectronics, Xiamen univ., China, GPA 88/100.
  Supervisor: Prof. Baolin Liu,
  Master thesis: modulation of polarization field in the active layer of GaN-based LEDs.
- *06. 2011-12. 2012* exchange student, Taiwan synchrotron radiation research center.
  Advisor: Prof. Zhechuan Feng
  Project: near edge X-ray absorption fine structure in III-nitride semiconductors.
- *09. 2006-06. 2010* bachelor of physics, Xiamen univ., China, GPA 80/100.

Employment history

- *01. 2014-01. 2015* research assistant, solid-state lighting laboratory, Xiamen Univ., China.
- *08. 2013-12. 2013* engineer of microelectronics, TP-LINK technologies Co., Ltd., China.

Expertise

- Experiments: ultrafast electron microscope and cathodoluminescence, time-resolved micro-photoluminescence, pulse laser mode-locking, frequency doubling and tripling, streak camera, laser pulse picking, ultrahigh vacuum and cryogenic temperature techniques, two-color pump-probe Raman spectroscopy, AFM, cleanroom skills.
- Programming: Matlab, Python, LabVIEW, COMSOL, Zemax.
- Theoretical framework: semiconductor physics, nonlinear optics, quantum optics.
- Language: English (advanced), French (A1), Chinese (native).

Fellowships

- *11. 2019* early postdoc. mobility at UCLA, Swiss National Science Foundation.
- *02. 2015* achievement award scholarship for new engineering graduate students, department of material science and engineering, Univ. of Florida.
- *09. 2012* the first prize scholarship for graduate students, department of physics, Xiamen Univ.

Supervision and teaching activities

- Training new PhD students about ultrafast spectroscopy experiments.
- 3 years teaching in the course of laboratoire de physique II, including supervising experiments and correcting reports of Michelson interferometry, optical grating spectroscopy, projection microscope and telescope.

Scientific reviewing

- As of *02. 2019*, reviewing 7 manuscripts for scientific journals: Applied Physics Letters, Journal of Applied Physics, Superlattices and Microstructures.

Publications in peer-reviewed scientific journals

- **W. Liu**, G. Rossbach, T. Schimpke, A. Avramescu, H.-J. Lugauer, M. Strassburg, C. Mounir,U. Schwarz, B. Deveaud, and G. Jacopin, *Impact of alloy disorder on Auger recombination in single InGaN/GaN core-shell microrods*, (under review in Physical Review B, 2019).

- **W. Liu**, C. Mounir, G. Rossbach, T. Schimpke, A. Avramescu, H.-J. Lugauer, M. Strassburg, U. Schwarz, B. Deveaud, and G. Jacopin, *Spatially dependent carrier dynamics in single InGaN/GaN core-shell microrod by time-resolved cathodoluminescence*, Applied Physics Letters 112, 052106, 2018.
- C. Haller, J.-F. Carlin, G. Jacopin, **W. Liu**, D. Martin, R. Butté, and N. Grandjean, *GaN surface as the source of non-radiative defects in InGaN/GaN quantum wells*, Applied Physics Letters 113, 111106, 2018.
- M. Shahmohammadi, **W. Liu**, G. Rossbach, L. Lahourcade, A. Dussaigne, C. Bougerol, R. Butté, N. Grandjean, B. Deveaud, and G. Jacopin, *Enhancement of Auger recombination induced by carrier localization in InGaN/GaN quantum wells*, Physical Review B 95, 125314, 2017.
- **W. Liu**, R. Butté, A. Dussaigne, N. Grandjean, B. Deveaud, and G. Jacopin, *Carrier-density-dependent recombination dynamics of excitons and electron-hole plasma in m-plane InGaN/GaN quantum wells*, Physical Review B 94, 195411, 2016.
- **W. Liu**, J.-F. Carlin, N. Grandjean, B. Deveaud, and G. Jacopin, *Exciton dynamics at a single dislocation in GaN probed by picosecond time-resolved cathodoluminescence*, Applied Physics Letters 109, 042101, 2016.

Oral presentations in international conferences

- **W. Liu**, C. Haller, G. Callsen, T. Weatherley, J.-F. Carlin, R. Butté, G. Jacopin and N. Grandjean, *Impact of point defects on Auger recombination in InGaN/GaN quantum well in the droop regime,* the 13th international conference on nitride semiconductors, U. S. , 2019.
- **W. Liu**, C. Haller, J.-F. Carlin, R. Butté, B. Deveaud, G. Jacopin and N. Grandjean, *Nanoscopic insight on decoration of non-radiative defects along step-edge in InGaN/GaN quantum well,* the 10th international workshop on nitride semiconductors, Japan, 2018.
- **W. Liu**, J.-F. Carlin, N. Grandjean, G. Jacopin and B. Deveaud, *Time-resolved cathodoluminescence for nanostructures in III-nitride semiconductors,* Paul-Drude-Institute workshop on cathodoluminescence of semiconductor nanostructures, Germany, 2018 (invited).
- **W. Liu,** C. Mounir, G. Rossbach, T. Schimpke, A. Avramescu, H.-J. Lugauer, M. Strassburg, U. Schwarz, B. Deveaud, and G. Jacopin, *Time-resolved cathodoluminescence of InGaN/GaN core-shell microwires,* the 12th international conference on nitride semiconductors, Germany, 2017.
- **W. Liu,** J.-F. Carlin, N. Grandjean, B. Deveaud, and G. Jacopin, *Exciton dynamics on a Single dislocation in GaN probed by picosecond cathodoluminescence*, the 18th international conference on extended defects in semiconductors, France, 2016.
- **W. Liu,** J.-F. Carlin, N. Grandjean, B. Deveaud, and G. Jacopin**, *Exciton dynamics on a single dislocation in GaN Probed by picosecond cathodoluminescence*, the 13th international conference on beam injection assessment in semiconductors, France, 2016.